УДК 517

Публікуються результати експериментальних та теоретичних досліджень у галузях фізичної електроніки, фізики плазми, фізики поверхні твердого тіла, емісійної електроніки, кріогенної та мікроелектроніки, нанофізики та наноелектроніки, високотемпературної надпровідності, квантової радіофізики, функціональної електроніки, твердотільної електроніки, мобільного зв'язку, медичної радіофізики, методів отримання діагностичної інформації та її комп'ютерної обробки.

Для науковців, викладачів вищої школи, студентів.

Experimental and theoretical contributions are published in the following fields: physical electronics, plasma physics, solid-state surface physics, emission electronics, cryogenic electronics, microelectronics, nanophysics and nanoelectronics, high-temperature supercondactive electronics, solid-state electronics, functional electronics, microwave electronics, quantum electronics, mobile communication, medical radiophysics, methods of receipt and computer processing of diagnosis information

Designed for researches, university teachers, students.

ЗМІСТ

СОДЕРЖАНИЕ

CONTENTS

ВИПУСК 2(20)

O. Bediukh , Ph.D., M. Drobkov, stud.
Department Quantum Radiophysics, Faculty of Radiophysics,
Taras Shevchenko National University of Kyiv

RADIO ABSORBING PROPERTIES OF THIN GOLD FILMS IN 8÷11,6 GHZ BAND

The results of measurements of absorbing properties of gold films of 8–20nm thickness deposited on a polymer substrate in the frequency band 8÷11.6 GHz electromagnetic radiation are presented.
Keywords: electromagnetic radiation, radar absorbing materials, nanoscale gold films, VSWR, 3-cm wavelength range.

Introduction. Reducing the impact of electromagnetic radiation (EMR) on technical devices and biological objects, especially due to the sharp increase in the number of sources of electromagnetic radiation (communication, consumer electronics, information systems, etc.), is an important task in a wide frequency band.

The development of new, improved radar absorbing materials (RAM) is one of the main components of the task of protection from EMR (along with screening, the use of design elements, etc.).

There are resonant absorbers, which are one type of RAM [4]. They use semitransparent metal films. If such film is situated at a distance of $\lambda/4$ (λ – wavelength of electromagnetic radiation) before conductive surface which has to be protected, it is provided the conditions for optimal matching at this wavelength. When several films use, with help of modern computational methods, it is possible to optimize not only the absorption band, but and number of layers, the total thickness and weight of the RAM.

Additional studies are conducted and for studying of the absorbing properties of metal films [1–2]. These works are carried out on the assumption that the film thickness is much smaller than the thickness of the skin layer in the selected band of wavelengths. At a film thickness of 10÷100 nm, this assumption holds for the microwave range.

The results of measurement of reflection and absorption of electromagnetic waves of the gold films in the frequency band 25÷37 GHz are presented in [3]. The objective of this study was to conduct similar studies in the band of 8÷12 GHz, which significantly extends the frequency range of the use of such films.

Experimental technique. For research it is used a gold film of 8÷20 nm thickness, obtained by thermal vacuum deposition on a dielectric polymer substrate of 0.1 mm thickness. Control the thickness of the film is implemented by known method of quartz oscillator.

The samples were cut with size slightly smaller than the cross section of the waveguide so that they are easily placed in him. The sample was placed between the layers of foam as shown in Figure 1. The gold film had no galvanic contact with the walls of the waveguide.
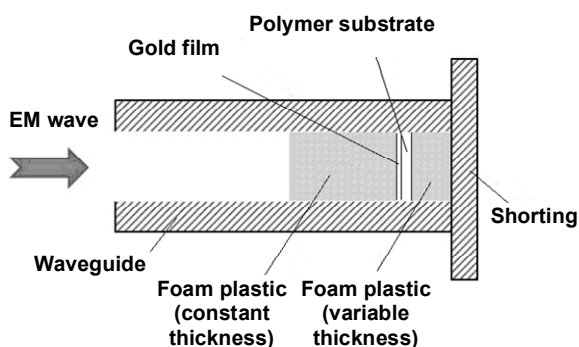
Measurements were carried out in the frequency band 8÷11.6 GHz (3 cm wavelength range) on panoramic VSWR meter P2-65 in the section of rectangular waveguide with a cross section of 28 x 12 mm for two cases: the segment of the waveguide was joined to the shorting in the form of metal plate or to the matched load.

The 8 samples with different thickness of the gold layer on the surface were used for measurements. The samples were selected in pairs with the same thickness of gold: 8 nm, 10 nm, 15 nm, 20 nm. Measurements were performed for each sample in the pairs and compared with each other.

This technique has allowed to verify the correctness of the data by collecting and comparing statistical information and to establish the correctness of the gold film deposition (i.e. its uniformity and accuracy of thickness determination).

We used a set of foam plates with thickness of 0.25 mm, 0.5 mm, 0.85 mm, 1 mm, 1.3 mm, 1.5 mm for change of the distance between the sample and the shorting

The waveguide segment with a sample, the matched load and the shorting were joined to the measuring waveguide line at four points so as to avoid any cracks, gaps and distortions in the joints. The sample was placed between the foam plates so that it remained in horizontal position.

Experimental results. Measurements were carried out for each values of the four thickness of gold film separately. The VSWR were measured at the distances changing from the film to the shorting.

For a visual representation of the data, they were grouped by the values of the gold film thickness and the distances between the sample and the shorting in the case of measurements with the shorting and by the values of the gold film thickness in the case of measurements with matched load.

The results of VSWR measurement for the sample with the gold film thickness of 8 nm in depending on the frequency are shown in Figure 2, where show the different cases according to the distance between the sample and the shorting.

Fig. 1. The placement of the samples in a segment of the waveguide line connected to a shorting
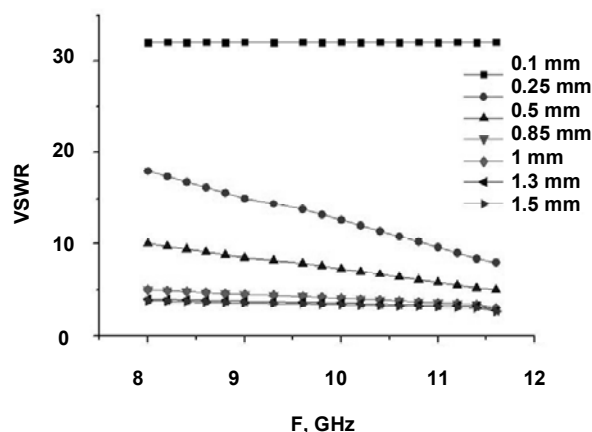
Fig. 2. The values of VSWR measurement as a function of frequency for the sample with a gold film thickness of 8 nm and the different distances between the sample and the shorting

The figure shows that the VSWR value depends on the distance between the sample and the shorting. Sharp drop of VSWR values to about 4–4.5 VSWR is noticeable with increasing distance between the shorting and the gold film.

The results of VSWR measurement for the sample with the gold film thickness of 10 nm in depending on the frequency and in the cases of the different distance between the gold film and the shorting are shown in Figure 3.
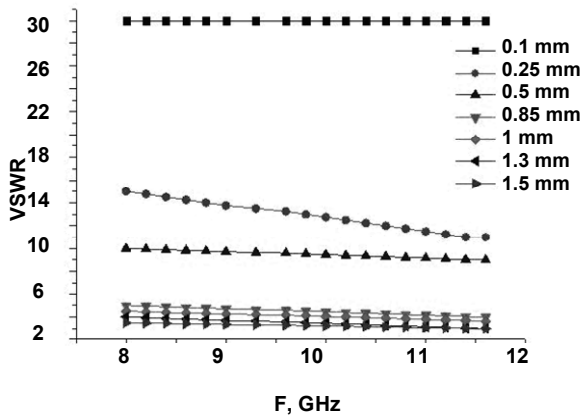
Fig. 3. The values of VSWR measurement as a function of frequency for the sample with a gold film thickness of 10 nm and the different distances between the sample and the shorting

As in the case of the 8 nm gold film we see qualitatively similar dependence of VSWR from the distance between the sample and the absorbing. It should be noted that increasing the thickness of the gold film on 2 nanometers has led to a greater drop in the value of VSWR with increasing the distance to the shorting to the level 2.5–3 that correspond of more than of 80% level of energy absorption.

The results of VSWR measurement for the sample with the gold film thickness of 15 nm in depending on the frequency and in the cases of the different distance between the gold film and the shorting are shown in Figure 4.
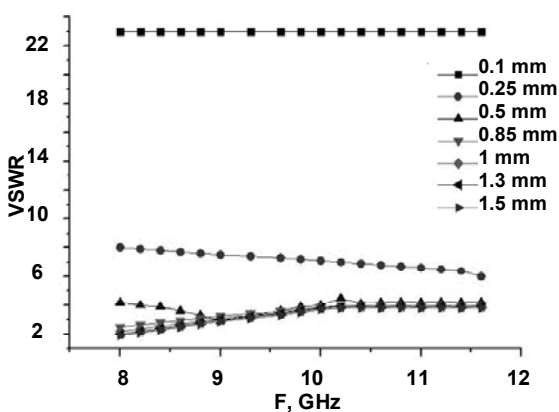
Fig. 4. The values of VSWR measurement as a function of frequency for the sample with a gold film thickness of 15 nm and the different distances between the sample and the shorting

We see that increasing the film thickness of 15 nm leads already to a gradual increase in the values of VSWR compared to the film thickness of 10 nm.

The results of VSWR measurement for the sample with the gold film thickness of 20 nm in depending on the frequency and in the cases of the different distance between the gold film and the shorting are shown in Figure 5.
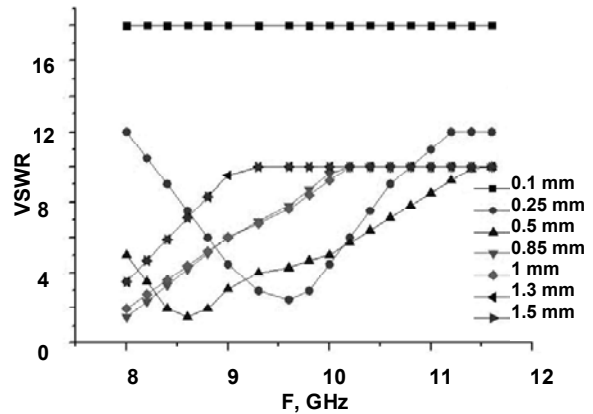
Fig. 5. The values of VSWR measurement as a function of frequency for the sample with a gold film thickness of 20 nm and the different distances between the sample and the shorting

We see that if the thickness of the gold film 20 nm value of VSWR already has significant frequency dependence. The value of VSWR is significantly higher than in cases of thickness 10÷15 nm. A similar trend was observed for measurements on duplicate sample.

The results of VSWR measurement depending on the frequency in case of connecting to the matched load for samples with different thickness of the gold film are shown in Figure 6.
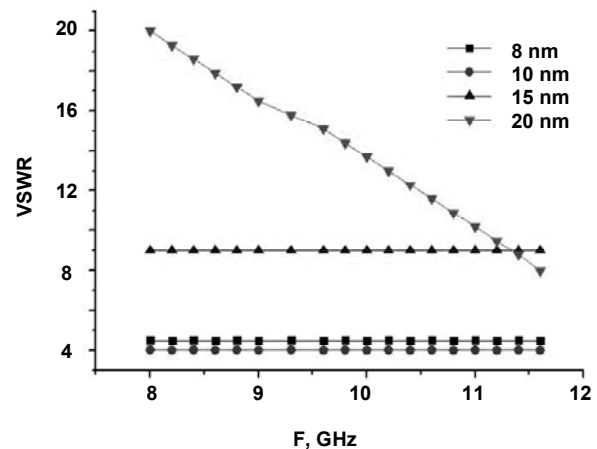
Fig. 6. The frequency dependence of VSWR for the samples with different thickness of gold film in case of connecting to the matched load

The obtained results allow clear that the optimal thickness of the gold film, for EMR absorption in 3-sm wavelength range is in the range of 8 to 15 nm.

Conclusions. The value of VSWR depends on the film thickness. The higher film thickness, the greater the reflection coefficient in the case of matched load (see Figure 6).

At a certain film thickness and the distance to a shorting the reflection is lower than in the case of a matched load. This suggests that there is an antiphase compensation reflected and incident waves, which is not resonant in nature and occurs throughout the all frequency range of measurement.

When the film thickness was 10 nm and the distance from a shorting was equal to 1.5 mm, VSWR across the all 3-cm measurement range was less than 3, which corresponds to more than 80% absorption of the incident electromagnetic radiation.

The obtained results showed high levels of absorption of electromagnetic energy by structures based on nanoscale gold films in a 3-cm wavelengths and prospects of using these structures in the design of real RAM.

The article is written on the results of the applied state budget research work № 12БП052-01

Reference

1. Andreev V.G., Vdovin V.A. and Voronov P.S. An experimental study of millimeter wave absorption in thin metal films. / Technical physics letters, Vol. 29, November 11 (2003), 953–955 2.. Antonets I.V., Kotov L.N., Nekipelov S.V. and Karpushov. E.N. Conductive and reflective properties of thin metal films. / Technical physics, Vol. 49, November 11 (2004), 1496–1500. 3. Bediukh O.R., Tepliy O Investigation of radio absorbing properties of thin metal films in the microwave range"; ICAP 2012, XII International young scientists' conference on applied physics, May 23–25, Kyiv, Ukraine, 2012. 4. Paul Saville. Review of Radar Absorbing Materials. Tehnical Memorandum, DRDC Atlantic, TM 2005–003, January 2005.

О. Бедюх, канд. фіз.-мат. наук, М. Дробков, студ.
кафедра квантової радіофізики, радіофізичний факультет
Київський національний університет імені Тараса Шевченка

РАДІОПОГЛИНАЮЧІ ВЛАСТИВОСТІ ТОНКИХ ПЛІВОК ЗОЛОТА В ДІАПАЗОНІ ЧАСТОТ 8÷11,6 ГГЦ

Наведені результати вимірювання поглинаючих властивостей плівок золота товщиною 8–20 нм, що нанесені полімерну підкладку в смузі частот 8 ÷ 11,6 ГГц електромагнітного випромінювання.

Ключові слова: електромагнітне випромінювання, радіопоглинаючих матеріалів нанорозмірних плівок золота, КСХН, 3 сантиметровий діапазон довжин хвиль.

О. Бедюх, канд. физ.-мат. наук, М. Дробков, студ.
кафедра квантовой радиофизики, радиофизический факультет
Киевский национальный университет имени Тараса Шевченко

РАДИОПОГЛОЩАЮЩИЕ СВОЙСТВА ТОНКИХ ПЛЕНОК ЗОЛОТА В ДИАПАЗОНЕ ЧАСТОТ 8÷11,6 ГГЦ

Приведены результаты измерения поглощающих свойств пленок золота толщиной 8–20 нм, нанесены полимерную подложку в полосе частот 8 ÷ 11,6 ГГц электромагнитного излучения.

Ключевые слова: электромагнитное излучение, радиопоглощающие материалы наноразмерных пленок золота, КСВН, 3 сантиметровый диапазон длин волн.

R. Bogdanov, eng. Department of Radio engineering and Radio-electronic Systems,
O. Kostiukevych, eng. Department Physical Electronics,
Faculty of Radiophysics, Taras Shevchenko National University of Kyiv

ZONED TARGET IN THE EXPERIMENTAL INVESTIGATION OF THE MAGNETRON SPUTTERING DEVICE WITH TWO EROSION ZONES

The Monte Carlo computer simulation program of the magnetron sputtering device with two erosion zones was build, in which the searching algorithm of the self-consistent starting positions of the secondary electrons on cathode was introduced. For the verification of the simulation results the zoned test target for the magnetron sputtering device was designed, which provides the measurements of the discharge current distributions along it surface. The comparison of the experimental results to the simulation demonstrates their compliance in the identical conditions.

Key words: zoned target, magnetron sputtering device, cathode sheath, computer simulation, Monte Carlo method

Introduction. Magnetron sputtering devices on direct current (hereafter – MSD) had found a wide application in the technology of coating of the conductive materials and their composites [12, 16, 17, 10]. Some of the latest investigations have shown the possibilities of carbon nanotubes synthesis by the magnetron sputter deposition method for wide sphere of technical applications [1–4].

The magnetic and electric fields in MSD are rather complicated, and this makes impossible an analytical description of the particles motion in them. The computer simulations of MSD based on the integration of particle motion equations and Monte Carlo collisions description are widely used now to predict the shape of erosion zone of the cathode-target [13, 14]. In the work [15] the Monte Carlo method was used to find the starting positions of secondary electrons at the cathode, which correspond to the steady state discharge operation mode and for indirect prediction of current-voltage characteristics of the discharge. The simple methods [13–15] were used for low working pressure (< 10 Pa) and they neglect the electric field changes in the cathode sheath, which provided by any variation of heavy particles (ions) density. This circumstance is eliminated in "particle-in-cell and Monte Carlo collision" method (PIC/MCC), in which every plasma species are presented as a limited ensemble of super-particles, and the Poisson equation is used to calculate the fully self-consistent electrical potential [8, 9]. This method requires more computer resources, but provides the most comprehensive description of the physical processes in MSD.

In the works [8, 9, 13–15] the MSD with single erosion zone of cathode-target ("race track") were investigated. The numerical model of the MSD with two erosion zones of the cathode-target (hereafter – CT), based on the Monte Carlo method, was built previously in the works [5, 6, 7] by authors. In the article [7] the searching algorithm of the self-consistent starting positions of the secondary electrons on the CT and the estimation of the cathode sheath thickness, based on the Child-Langmuir law, were presented. Modeling results in [6, 7] were compared with experimental data of sputtering of the multilayer target from the non-magnetic materials. There were obtained the dimensions of the internal and external CT erosion zones in the two characteristic opposite cases. There are the case of "low" discharge currents (≤ 15 mA), in which only the external discharge zone was able to ignite, and the case of the "high" currents (≥ 40 mA), when both discharge zones were ignited. Unfortunately, it was impossible to obtain from these measurements the absolute values of discharge current in the corresponding zone, which is important for checking the results of computer simulation.

The MSD with two erosion zones [11] is the module of the industrial vacuum system VUP-5 and has the area of the cathode unit about $4,5 \cdot 10^3 \, \text{mm}^2$, on which the disk-

shaped target with same size is mounted. The target area, which is efficiently used in $1,9..2,0 \cdot 10^3 \text{mm}^2$ [6, 7]. On the surface of the cathode the magnetic induction could reach up to $B_t = 0,084\,\text{T}$ and decreases on the up distance h according to the $\sim \exp(-h/L)$ law, in which L is characteristic length (in the internal discharge zone it is $L_1 = 3,2\,\text{mm}$, in the external – $L_2 = 6,4\,\text{mm}$). This feature of magnetic field makes impossible ignition of the internal zone of discharge at current $\leq 15\,\text{mA}$, when the cathode sheath d_E is much bigger than L_1 [5].

In order to estimate abilities of this MSD for carbon nanotubes synthesis, like in [1–4], in this article the approach of definition of ion current distribution on the CT surface has been proposed. Also the cathode sheath thickness along the CT radius has been estimated. It was made both in experimental and the computer simulation ways.

Modeling and experiment. Both at the experiment and in the computer model the reference point of cylindrical coordinate system was chosen in the centre of CT surface. If at the beginning of calculation the secondary electrons are randomly placed on the CT surface, according to the magnetic confinement there are two discharge zones be able to appear [5]. Then for the acceleration of computer calculation, the electrons were started on the CT areas, where the discharge is maintained the most effectively (on the radius r : in internal zone – $5..10\,\text{mm}$, in external – $21..26\,\text{mm}$). The discharge voltage U_d and work gas pressure p must be defined from the experiment. Hereafter is accepted that U_d predominantly applied on the discharge cathode sheath.

The cathode sheath thickness also needs the definition. In order to improve the computer simulation at the small thickness of the cathode sheath d_E ($d_E \leq 3,2\,\text{mm}$) it was perfected the shape of model cathode sheath (in compare with [5-7]). In the articles [5-7] the d_E was steady on the whole CT surface (as in [14, 15]) and was chosen in maxima of magnetic field induction. Now this value is marked as $d_{E\,Min}$. Now, the d_E depends on the magnetic induction value, which is parallel to the CT surface along radius r (Fig. 1).

The algorithm of self-consistency of the secondary electrons starting positions is the distinguishing feature of this computer model. The several tracing cycles of secondary electrons from the surface of CT are performed. If at first cycle the electron's positions on the CT are random, but then they are defined by ionization acts positions. The secondary electrons quantity is estimated by secondary ion-electron emission ratio $\gamma < 0,1$ [12, 15]. In comparison with the previous work [7], it is a new criterion of evaluation of steady state of the discharge. It is based on the comparison of the average quantity of ionization acts per one secondary electron – n_i, created on this cycle to the previous. If difference is less than $5\,\%$, the steady state mode of the discharge is reached (like in [15]). After that we can to calculate the ion motion, the radial distribution of the ions relative number and energy, like in [5].

Distribution of the discharge current could be associated to the ion distribution at CT surface, because only there ions define the discharge current. If the discharge current I_d is known experimentally in this discharge operation mode, the distribution of the discharge current could be estimated in easy way.
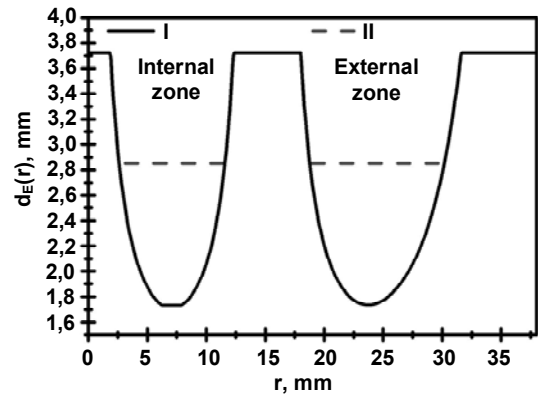
Fig. 1. The cathode sheath thickness at the computer modeling. (The curves I – at $d_{E\,Min} = 1,737\,\text{mm}$, and II – at $d_{E\,Min} = 2,834\,\text{mm}$)

The zoned test target was made in order to check the results of simulation (Fig. 2). It consists of eight flat rings from non-magnetic steel (its thickness is of $1\,\text{mm}$) and central platform. There are placed on the isolating mica substrate with a thickness of $0,1\,\text{mm}$. Every zone-ring is connected individually to the common power source, and can be commutated for the immediate current measurement on itself. Radial position of the ring's middle r_i was determined by this formula, in which central zone was taken in account as the ring (the dimension units – mm):

$$r_i = (4i - 2,5), \qquad (1)$$

where i – the ring number from 1 to 9.

According to the previous radius formula (1) the ring's area is (the dimension units – mm^2):

$$S_i(r_i) = 2\pi \cdot a \cdot r_i, \qquad 2)$$

where r_i – the radial position (1); a – the thickness of zoned target ring, which equals $a = 3\,\text{mm}$ (and the distance between rings equals $1\,\text{mm}$ (Fig.2)). The similar method of the cathode-target division was used in computer modeling, but the distance between rings was 0, and rings thickness was $1\,\text{mm}$.
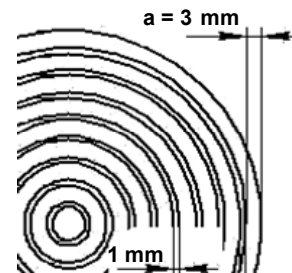
Fig. 2. Zoned target layout

If ion current on the ring i is I_i, according to the (2) the current density $j_i(r_i)$ could be determined as:

$$j_i(r_i) = I_i / S_i(r_i). \qquad (3)$$

In our article j_i will have the dimension mA/cm^2. The ion current density is less than discharge current density in $(1 + \gamma)$ times, where γ – is the coefficient of the secondary ion-electron emission ($\gamma < 0,1$).

The Child-Langmuir law could be used to estimate the cathode sheath thickness d_E under the condition of low

pressure and big mean free path of ions [12 p.98]. The following formula is being used for determination of d_E (dimension of d_E is mm):

$$d_E(r) = 2,43 \cdot 10^{-3} \cdot \left(V_d^{0,75} \Big/ \left(M_i^{0,25} \cdot \left(j_i(r) \right)^{0,5} \right) \right), \qquad (4)$$

where V_d – is the voltage fall on the cathode sheath similar to the interelectrode space of flat gas-filled diode, and as mentioned before $V_d \approx U_d$; M_i – is ion mass of working gas Ar in atomic mass units ($M_i = 40$); $j_i(r_i)$ – is density of ion current on the cathode surface from (3), but in this case in A/cm^2 like in [7, 12].

In this article the value $d_E(r)$ from (4) is called as "effective thickness" of the cathode sheath.

The experimental results obtained on the zoned target. Measuring of the radial distribution of discharge current was made at three pressures of working gas Ar : $p_1 = 0,67\,Pa$, $p_2 = 1,33\,Pa$, $p_3 = 6,65\,Pa$, and also at four discharge currents I_d , of 15 mA , 45 mA , 90 mA , 150 mA . In such conditions the discharge voltage U_d was changed in the range from 240 V to 480 V . There are presented the data by two typical currents. In the case of the discharge current $I_d = 15\,mA$ only the external discharge zone is ignited as in [5]. If the current is $I_d = 90\,mA$ both zones are ignited.

For the cases $I_d = 15\,mA$ and $I_d = 90\,mA$ there are presented the radial distributions of the ion current density on the cathode target given according to (1)-(3) (Fig. 3, 5). Efficient thickness of cathode sheath $d_E(r)$ is presented on the Fig. 4 and Fig. 6. There are taken in account the ratio of the secondary ion-electron emission $\gamma = 0,1$.

The discharge mode at $I_d = 15\,mA$ shows the existence of intensive external discharge zone, in which ion current density is much bigger then in internal zone (Fig. 3).
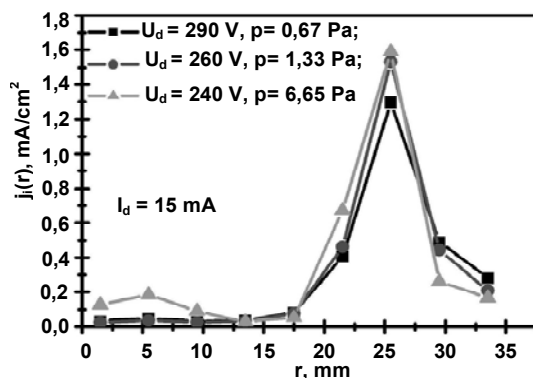
Fig. 3. The ion current density radial distribution on zoned target at $I_d = 15\,mA$

In such conditions in external zone effective cathode sheath thickness (4) goes down to $d_E = 2\,mm$ for every pressure. This value is lesser than mentioned before value $L_2 = 6,4\,mm$ for the magnetic field (*Fig. 4*). In the internal zone the cathode sheath does not have big differences at pressures $p_1 = 0,67\,Pa$ and $p_2 = 1,33\,Pa$. The characteristic length $L_1 = 3,2\,mm$ is strongly exceeded. Vice versa, if the pressure of working gas argon amount to $p_3 = 6,65\,Pa$, the cathode sheath in the internal zone is

close to L_1 (Fig. 4). It provides better conditions for effective magnetic confinement of electrons in the zone of acceleration on the electric potential, which suitable for discharge ignition in this zone.
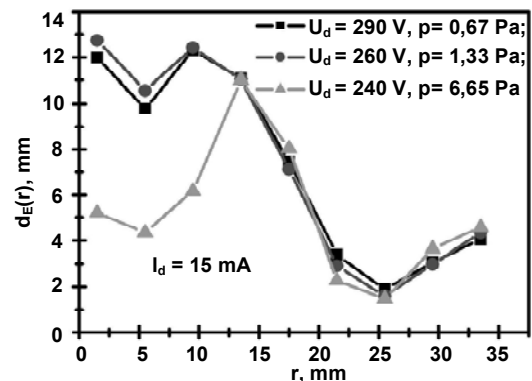
Fig. 4. The radial distribution of effective thickness of the cathode sheath on zoned target at $I_d = 15\,mA$

If the discharge current is $I_d \geq 45\,mA$, the simultaneously increasing of ion current density corresponded to noticeable decreasing of the cathode sheath thickness in both zones. If current is $I_d = 90\,mA$ (Fig. 5), the value of $d_E(r)$ in the internal zone are lesser than L_1 (Fig. 6). It automatically provides acceptable conditions for discharge in this zone. At the pressure $p_3 = 6,65\,Pa$ the current density in internal zone begins to exceed the ones in external zone (Fig. 6).
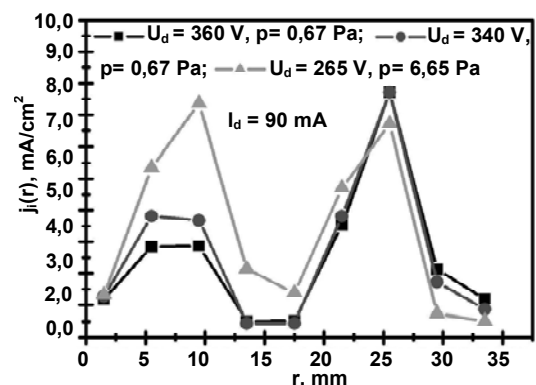
Fig. 5. The ion current density radial distribution on zoned target at $I_d = 90\,mA$
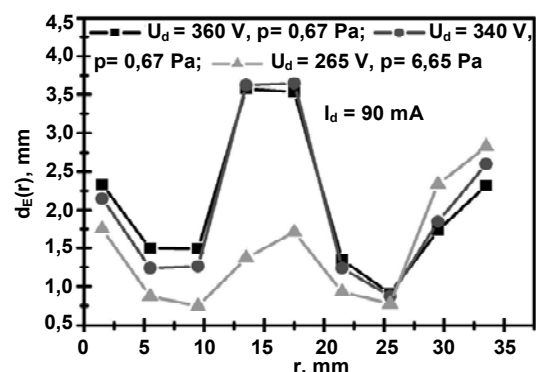
Fig. 6. The radial distribution of effective thickness of the cathode sheath on zoned target at $I_d = 90\,mA$

For the CT area, limited by radius $r = 38\,\text{mm}$, the average cathode sheath thickness d_E could be equals from $1,2\,\text{mm}$ to $3,9\,\text{mm}$ under the conditions of every experimental voltage U_d and appropriate currents I_d (from (4)). For the current $I_d = 90\,\text{mA}$ and more the cathode layer in both discharge zones (with area $2,0\cdot10^3\,\text{mm}^2$ [7]) should be approach to $1,0..1,5\,\text{mm}$ at every pressures, which close to results of the work [8] for such magnetic field.

Comparison of the computer simulation results with zoned target data. In the computer simulation at the conditions of discharge current $I_d = 90\,\text{mA}$, Ar pressure $6,65\,\text{Pa}$ and cathode sheath voltage $V_d = 265\,\text{V}$, the minimal starting cathode sheath thickness was chosen as $d_{E\,Min} = 1,737\,\text{mm}$ (Fig. 1). At the pressures $1,33\,\text{Pa}$ and $0,67\,\text{Pa}$ ($V_d = 340\,\text{V}$ and $V_d = 350\,\text{V}$) it was chosen $d_{E\,Min} = 2,834\,\text{mm}$ (Fig. 1). Only at these values of $d_{E\,Min}$ the conditions of the steady state of the discharge were reached.

The cathode sheath potential $-V_d$, gives to the secondary electron the energy eV_d, where $-e$ is the electron charge. Dividing the eV_d on the average quantity of ionization acts on the one secondary electron n_i we could to obtain the energetic ionization cost. In the computer simulation results for the pressures $0,67\,\text{Pa}$ and $1,33\,\text{Pa}$, this value is close to $31\,\text{eV}$, which corresponds to the well-known experimental facts for Ar [10, 15].

The Fig. 7–9 presents the simulation results of effective cathode sheath thickness $d_E(r)$ at the current $I_d = 90\,\text{mA}$ and the results by zoned target at appropriate pressures and voltages for the comparison. (In this figures and simulation $\gamma = 0,073$, which looks more realistic).

Obviously, that the simulation results make possible to predict the distribution of discharge current density on radius more accurate than measurement on the zoned target. As we can see from Fig. 7-9, the suppositions, which were made for the form of the cathode sheath (Fig. 1), could be automatically improve in process of finding of self-consistent starting positions of secondary electrons on the CT. Obtained plots demonstrate good coincidence with experimental results at pressures $0,67\,\text{Pa}$ and $1,33\,\text{Pa}$ (Fig. 7. and Fig. 8.). For the pressure $0,67\,\text{Pa}$ it was chosen $V_d = 350\,\text{V}$ because of the best coincidence with experimental results (Fig 7).
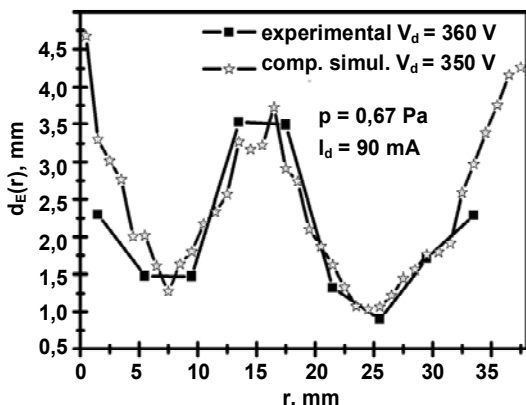
Fig. 7. The comparison of computer simulation results with results on the zoned target at $I_d = 90\,\text{mA}$, $p = 0,67\,\text{Pa}$
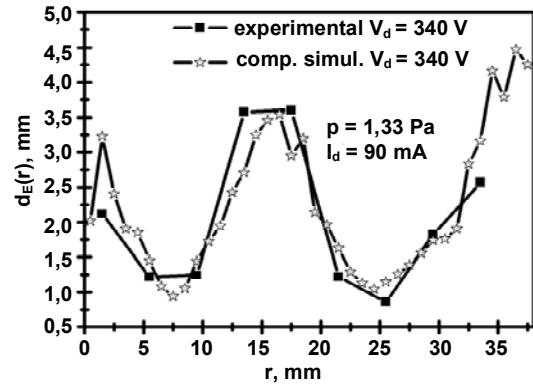
Fig. 8. The comparison of computer simulation results with results on the zoned target at $I_d = 90\,\text{mA}$, $p = 1,33\,\text{Pa}$
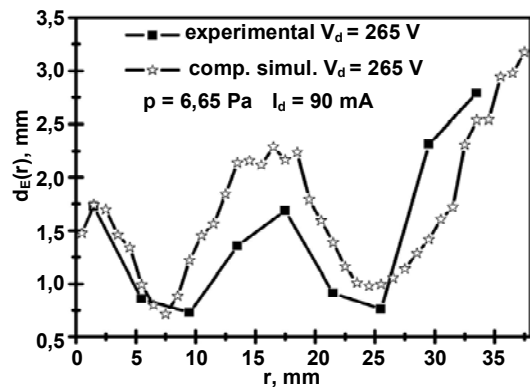
Fig. 9. The comparison of computer simulation results with results on the zoned target at $I_d = 90\,\text{mA}$, $p = 6,65\,\text{Pa}$

Noticeable differences are taken place at pressure $6,65\,\text{Pa}$ (Fig. 9). It could be related with overstated initial value of the cathode sheath thickness between zones at such conditions (Fig. 1). But difference of distribution for the internal zone versus the external one is even stronger.

Conclusions. For the investigation of the distribution of discharge current on the cathode-target of MSD with two erosion zones the zoned target was used. The measurements (at the three pressures of working gas Ar – $0,67\,\text{Pa}$, $1,33\,\text{Pa}$, $6,65\,\text{Pa}$) of the distribution of the discharge current in MSD along cathode-target radius converted to the cathode sheath with using of the Child-Langmuir law [12, 7] were held. This results have confirmed the assumption about influence of the confinement magnetic field variation in the MSD along the vertical distance from the cathode on the discharge current distribution on the cathode at the "low" ($15\,\text{mA}$) and "high" ($90\,\text{mA}$) discharge currents. At discharge current $90\,mA$ the comparison of experimental dependencies with values from the computer simulation has been made.

The discharge simulation program based on the Monte Carlo method [5–7] has been improved with taking into account the non-homogeneity of the cathode sheath, which depends on the magnetic field induction along the cathode radius. Algorithm of self-consistency of starting positions of secondary electrons also was improved.

The results of computer simulation at $90\,\text{mA}$ are demonstrated coincidence to the data received by experiments on the zoned target. In experiment as well as in simulation results were demonstrated the locating of the maximal current density in the internal zone of discharge at $90\,\text{mA}$ and working pressure $6,65\,\text{Pa}$ were demonstrated.

Thus, the Monte Carlo numerical model of MSD with two erosion zones which was designed in previous articles [5–7] and has been improved in present work, clearly describes the discharge behavior in practically useful cases. It could be used for foreseeing the target sputtering efficiency on this magnetron sputtering device, which is important at thin film production.

References

1. Antonenko S.V. Issledovanie uglerodnyh nanostruktur, poluchennyh metodom raspylenija na postojannom toke / S.V. Antonenko, S.N. Mal'cev, A.A. Timofeev // Inzhenernaja fizika. – 2002, – №1. – P. 38–40. (in Russian). 2. Magnetronnaja tehnologija sozdanija grafitovyh pokrytij, nanotrubok, i nanostruktur na ih osnove, / S.V. Antonenko // Funkcional'nye materialy i vysokochistye veshhestva. – M.: 2007. – Rezhim dostupu: http://www.edu-cons.net/atlas_last/doc/444/Antonenko_rus.pdf. – Nazva z ekranu. (in Rus.). 3. Novye uglerodnye nanosistemy na osnove nanotrubok, fullerenov i ih proizvodnyh / Antonenko S.V., Malinovskaja O.S. // Funkcional'nye materialy i vysokochistye veshhestva, – M.: 2007. – Rezhim dostupu: http://www.edu-cons.net/atlas_last/doc/443/Antonenko_Mal_rus.pdf. – Nazva z ekranu. (in Russian). 4. Antonenko S.V. Mal'cev S.N. Poluchenie uglerodnyh nanotrubok metodom magnetronnogo raspylenija na postojannom toke / S.V. Antonenko, S.N. Mal'cev // Pribory i tekhnika eksperimenta. – 2005. – №3. – P.150–152. (in Russian). 5. Bogdanov R.V. Komp'yuterne modelyuvannya mahnetronnoho rozpylyuvanoho pristroyu z dvoma zonamy eriziyi / R.V. Bogdanov, O.M. Kostiukevych. // Visnik Kyyivskoho nacionalnoho universitetu imeni Tarasa Shevchenka. Seriya "Ffizyko-matematichni nauky", – 2012, – №1, – P. 249–260. (in Ukrainian). 6. The computer simulation of the sputtering magnetron device with two erosion zones and it comparison to experimental results / R.V. Bogdanov, O.M. Kostiukevych. // thesis of "XIIth International Young Scientists' Conference on Applied Physics", May, 23–26, 2012; – Kyiv, Ukraine, Taras Shevchenko Nat. Univ. Rad.-Phys. Faculty, – P.182-183. 7. Bogdanov R.V., Kostiukevych O.M.. Experimental investigation and computer simulation of the magnetron sputtering device with two erosion zones / R.V. Bogdanov, O.M. Kostiukevych // "Problems of Atomic Science and Technology" Series: Plasma Physics (19), – 2013. – No.1. – P.189–191. 8. Bultinck E. The effect of the magnetic field strength on the sheath region of a dc magnetron discharge / E. Bultinck, A. Bogaerts // J. Phys. D: Appl. Phys – 2008. – No.41, 20 2007, – P.1–5. 9. Bultinck E., Particle-in-cell/Monte Carlo collisions treatment of an Ar/O2 magnetron discharge used for the reactive sputter deposition of TiOx films / Bultinck, A. Bogaerts // New J. Phys., – 2009, – No.11, 103010, – P.1–25. 10. Kashtanov P.V. Magnetronnaja plasma i nanotehnologia / P.V. Kashtanov, B.M. Smirnov, R. Hippler // Uspekhi Fizicheskikh Nauk, – 2007, – №5, – T.177, – №5, – P.473–510. (in Russian). 11. Kucherenko E.T. Magnetronnoe raspylitelnoe ustroystvo s dvumua zonams eriziyi / E.T. Kucherenko // Plasmotehnologia-97: Sb. nauch. trudov.; Zaporozhye: RIP "Vidavets", 1997, – P.121–124. (in Russian). 12. Kuzmichev A.I. Magnetronnyie raspilitenye systemy. Kniga 1. Vvedenie v fiziku i tehniku magnetronnogo raspilenija. / A.I. Kuzmichev // Kiev: "Avers", 2008. – 244 p. – ISBN 966-8934-07-5. (in Russian). 13. Magnetic field improvement in end region of rectangular planar DC magnetron based on particle Simulation, / [Qiu Qingquan, Li Qingfu, Su Jingjing, Jiao Yu, Jim Finley] // Plasma Science and Technology, – 2008, – Vol.10, No.6, – P. 694–700. 14. Musschoot J. Influence of the geometrical configuration on the plasma ionization distribution and erosion profile of a rotation cylindrical magnetron: a Monte Carlo simulation / J. Musschoot, D. Depla, J. Haemers, R. De Gryse // Plasma Sources Sci. Technol., – 2006, – No.39, 015209, – P. 3989–3993. 15. Musschoot J. Investigation of the sustaining mechanisms of dc magnetron discharges and consequences for I-V characteristics / J. Musschoot, D. Depla, J. Haemers, R. De Gryse. // Plasma Sources Sci. Technol., 2008, – No.41, 015209, – P.1–5. 16. Soloviev A. A. Harakteristiki plazmy nesbalansirovannoj magnetronnoj raspylitel'noj sistemy i ih vlijanie na parametry pokrytij ZnO:Ga / Soloviev A.A., Zaharov A.N., Rabotkin S.V., Oskomov K.V., Sochugov N.S. // Fizika i khimija obrabotki materialov, – 2009, – №2, – P.58–65. (in Russian). 17. Shirajev S.A. Poluchenie i svojstva kompozicionnyh pokrytij na osnove metall-uglerod s nanokristallicheskoj strukturoj / Shirjaev S.A., Atamanov M.V., Guseva M.I., Martynenko Ju.V., Mitin A.V., Mitin V.S., Moskovkin P.G. // Zhurnal tekhnicheskoj fiziki, – 2002, – T.72, – Vyp. 2, – P. 99–104. (in Russian).

Р. Богданов, інж., кафедра радіотехніки та радіоелектронних систем,
О. Костюкевич, інж., кафедра фізичної електроніки
радіофізичний факультет, Київський національний університет імені Тараса Шевченка

ЗОНОВАНА МІШЕНЬ В ЕКСПЕРИМЕНТАЛЬНОМУ ДОСЛІДЖЕННІ МАГНЕТРОННОГО РОЗПИЛЮВАЛЬНОГО ПРИСТРОЮ З ДВОМА ЗОНАМИ ЕРОЗІЇ

Побудовано комп'ютерну модель магнетронного розпилювального пристрою з двома зонами ерозії, засновану на методі Монте-Карло, де введено алгоритм пошуку самоузгоджених стартових позицій вторинних електронів на катоді. Для перевірки результатів комп'ютерного моделювання було виготовлено зоновану тестову мішень для даного магнетронного розпилювального пристрою, яка забезпечила вимірювання розподілів розрядного струму по своїй поверхні. Порівняння результатів експерименту та моделювання продемонстрували їх відповідність за однакових умов.

Ключові слова: зонована мішень, магнетронний розпилювальний пристрій, катодний шар, комп'ютерне моделювання, метод Монте-Карло.

Р. Богданов, инж., кафедра радиотехники и радиоэлектронных систем,
О. Костюкевич, инж., кафедра физической электроники
радиофизический факультет, Киевский национальный университет имени Тараса Шевченка

ЗОНИРОВАННАЯ МИШЕНЬ В ЭКСПЕРИМЕНТАЛЬНОМ ИССЛЕДОВАНИИ МАГНЕТРОННОГО РАСПЫЛИТЕЛЬНОГО УСТРОЙСТВА С ДВУМЯ ЗОНАМИ ЭРОЗИИ

Построена компьютерная модель магнетронного распылительного устройства с двумя зонами эрозии, основанная на методе Монте-Карло, в которой введен алгоритм поиска самосогласованных стартовых позиций вторичных электронов на катоде. Для проверки результатов компьютерного моделирования была изготовлена зонированная тестовая мишень для данного магнетронного распылительного устройства, которая обеспечила измерения распределений разрядного тока по своей поверхности. Сравнение результатов эксперимента и моделирования продемонстрировало их соответствие при одинаковых условиях.

Ключевые слова: зонированная мишень, магнетронный распылительное устройство, катодный слой, компьютерное моделирование, метод Монте-Карло.

A. Ivanisik, Ph.D., P. Korotkov, D.Sci., Taras Shevchenko national university of Kyiv,
Faculty of Radiophysics, Department of Medical Radiophysics
G. Ponezha, Ph.D., National academy of statistics, accounting and auditing,
Faculty of Economy and Statistics

SUBNANOSECOND STIMULATED RAMAN SCATTERING PULSES OF Q-SWITCHED LASER AT SELF-FOCUSING

The results of experimental study confirm the availability of using self-focusing media for creation of highly efficient transformers of laser radiation based on stimulated Raman scattering. It has been shown that due to the self-focusing dynamics, such transformers can change frequency and compress giant pulses of multimode lasers more than in ten times, utilizing a simple scheme. The proposed and implemented scheme is suitable for generation of initiating subnanosecond Stokes pulses, which further can be used for compression of giant laser pulses with a corresponding increasing of power.

Keywords: laser, self-focusing, stimulated Raman scattering.

Introduction. It is known that SRS (stimulated Raman scattering) is successfully used in transformers of laser radiation for frequency tuning, pulse compression and improving of optical beam quality [6, 1]. However, SRS-

active media, which have practical use, are limited to hydrogen and methane (at pressure of tens of atm) or certain crystals. Such available, optically stable and easy to use media as self-focusing liquids (benzene, toluene, etc.), there historically first SRS was observed [9], were neglected because of unsuccessful attempts to create the highly efficient quantum electronics devices. This narrows the range of radiation frequencies that can be obtained from a laser, and thus reduces the value of SRS as a method of frequency tuning.

In self-focusing liquids, experimental threshold of SRS is defined by critical power of self-focusing [2] and achieved very easily. However, there are significant complications to achieve the high energy conversion efficiency of laser radiation. Mostly, in self-focusing liquids conversion efficiency in the first Stokes SRS component does not exceed ~20% under the excitation by a giant pulse of a multimode laser and in all Stokes components it is ~ 30%. This situation was classified as an effect of "absolute saturation of stimulated scattering" [7] the nature of which remains until now unclear. Nevertheless, the main problem is effect of small-scale self-focusing.

In our opinion, SRS-based transformers with high conversion efficiency still can be created in self-focusing liquids, but in two stages - in a two-cell scheme. Namely, a seed pulse is generated under forward or backward SRS in a cell where the threshold of self-focusing is exceeded, and then is enhanced below threshold of self-focusing in the second cell. It is important that, besides of achievement of the high overall conversion efficiency in the two-cell scheme, in the first cell it can possible to reduce simultaneously a pulse duration (and hence, as a result, to compress the pulse) using dynamic of self-focusing process.

In addition, it should be noted that the most important practical results of solving the problem of increasing the SRS effectiveness in self-focusing liquids is closely linked to the availability of the exciting laser. Therefore, it is particularly important to solve a complex problem: the efficient conversion of the available multimode laser radiation and at the same time improving the optical quality of the radiation. The above circumstances stimulated experimental research described in this work.

Thus, the work is aimed to obtain Stokes subnanosecond pulses in self-focusing SRS-active liquids under the excitation by multimode Q-switched laser. These pulses can be used as initiators in the gain stage and can define the temporal-spatial characteristics of the converted laser radiation.

Results of experimental studies. The multimode ruby laser with the linear resonator of 35 cm-length and with passive switching of resonator quality was used. The laser radiated light pulses at a wavelength 0.6943 μm with the energy 0.6 J. Duration of pulses was τ_L =30 ns at half level of intensity. The root mean square of the pulse energy variation was 5%. An envelope of the laser pulse (recorded by C7-10B oscillograph) was smooth. The hath-width of the pulse spectrum (measured using a Fabry–Pérot interferometer with a ring thickness 30 mm and sharpness $F^* \approx 20$) was 0.01 cm^{-1}, which is less than the spectral distance between two longitudinal modes of the empty laser cavity (0.014 cm^{-1}). The laser beam at an intersection (with the diameter of about 1 cm) was heterogeneous with a large number (10^2) maxima and minima of intensity.

For this laser, the threshold of SRS was exceeded in 3.5 times without addition focusing in the cell of 25cm-length with toluene (C_6H_5-CH_3). The conversion efficiency into all Stokes components, propagating in the direction of the excitation beam, was approximately 20% of the laser pulse energy. Forward SRS-pulse duration ranged from 15 ns to 25 ns, that is not less than half the duration of the laser pulse.

For obtaining and registration of short pulses of Stokes SRS, the optical scheme shown in Fig. 1 was used.
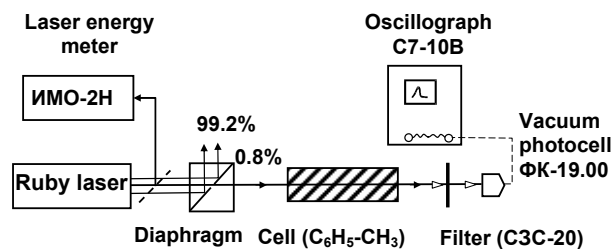
Fig. 1. Optical scheme

Laser radiation partially (0.8%) passes through the diaphragm and reaches the 25 cm-cell with toluene. Optical filter C3C-20 after the cell absorbs laser radiation. Scattered light (mostly first Stokes SRS) after passing through the filter enters the registration scheme. The registration scheme consists of a photovoltaic vacuum cell ФК-19.000 (rise time from 0.1 to 0.9 of maximum value of the current pulse less than 0.7 ns) and the oscillograph C7-10B with a signal delay line (a bandwidth of the delay line is at least 650 MHz with the recession 3dB).

The diaphragm (Fig.1) is formed by two 90^0-prisms, which hypotenuse surfaces have an optical contact of limited area with glycerin. The surface of the optical contact in the form of a disk has a diameter $D \approx 0.4$ mm. Compared to a conventional diaphragm, such diaphragm has an advantage. Namely, at powerful light pulse (~20MW at used laser), optical breakdown is prevented on its boundary. In addition, the laser radiation, which does not pass the diaphragm (99.2%), can be used in the gain channel.

The diameter D=0.4 mm of the diaphragm aperture was chosen based on the fact that in toluene the laser beam fragments into individual parts which self-focus independently. Applying the registration scheme for obtaining the spatial-angular spectra and the calculation procedure described in works [3, 4], it was determined that at the cell entrance, the average diameter of these fragments of the laser beam was $d \approx 0.23$ mm. In the cell with toluene at the diameter ratio $D/d<2$, with high probability not more than one self-focusing focal point is formed simultaneously and, thus, formation of many independent sources of SRS with different phase, spatially localized within focal area, is prevented.

The distance 5 cm between the diaphragm and the cell was selected experimentally to make sure that the SRS threshold is exceeded for each laser pulse, under the given instability of spatial and temporal characteristics the used multimode laser.

In the case of increasing distance between the diaphragm and the cell to 10cm, the threshold of SRS was not achieved. It is consequence of the beam diffraction at the distance between the diaphragm and the cell. As a result of the diffraction an area of self-focusing was not formed.

Radiation energy passed through the diaphragm was approximately 4mJ. It is only 0.8% of the total energy of the laser pulse. Under these conditions, the average pulse energy of SRS was 0.15 mJ, which corresponded to the energy conversion efficiency of laser radiation 4%, significantly less than the conversion efficiency in the absence of the diaphragm.

Fig. 2 shows oscillograms of the laser (a) and SRS (b) pulses without the diaphragm and of the laser (c) and SRS (d) pulses after the diaphragm. For emphasize the differences in the shape and duration, all pulses in Fig. 2 were normalized so that their amplitudes were the same.
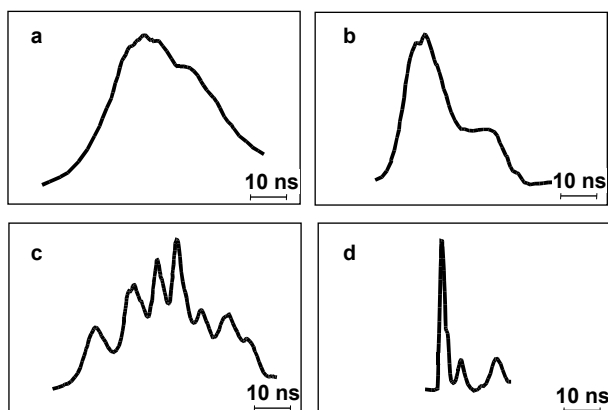
Fig. 2 Oscillograms of pulses:
laser (a) and SRS (b) pulses without the diaphragm; laser (c)
and SRS (d) pulses after the diaphragm

The oscillograms of laser pulses after the diaphragm (Fig. 2, c) have almost 50% modulation with period of about 7 ns. Note, for the laser resonator length 35cm, longitudinal modes beating would lead to a modulation with a period of 2.3 ns. So, the modulation should be attributed to the beating of transverse modes or deformation of mode structure of the beam in the process of generation.

The oscillogram of SRS pulse (Fig. 2, d) shows that in the proposed scheme, under using the diaphragm, subnanosecond pulse duration of SRS can be obtained. The duration of SRS pulses at half the level of intensity was less than 1 ns.

Quite often, even with constant experimental conditions, after the first pulse of SRS, one or two pulses were observed additionally. They were usually longer and have a lower amplitude. Period of these pulses closely correlates with the period of oscillation of intensity laser radiation after the diaphragm (Fig. 2, c).

Analysis and conclusion. The experimental data allow us to evaluate the effectiveness of SRS in a separate focal area. Assuming that the laser pulse has duration τ_L =30 ns at the half level of intensity and energy E_L =4 mJ after the diaphragm, we obtain the value of the laser power $P_L = E_L / \tau_L$ =133 kW. The critical power for self-focusing in toluene is P_{CR} =25 kW [4]. As the SRS-threshold and, hence, the threshold of self-focusing in the absent of the diaphragm was overcame in μ =3.5 times, we can evaluate the power of the laser radiation which self-focusing in separate focal area after entering the diaphragm: $P_L^* = k\mu P_{CR}$ =80 kW, where k =0.92 is a loss factor due to the light reflection at the outer sides of the diaphragm. Thus, in the focal region it was 60% of the radiation passed the diaphragm. The other part of the radiation (40%) was not involved in the generation of SRS-pulse.

If in the focal region the full depletion of the laser pulse at SRS takes place, then the amplitude of SRS pulse in the

oscillograms must be also 60% of the laser pulse amplitude. In the experiment, the amplitude ratio of SRS/laser pulses (after taking into account the filter transmission and the spectral sensitivity of the photocell) reached 0.5. It can be concluded that the energy conversion efficiency of laser radiation in the focal region reached in the experiment the value of about $0.5/0.6 \approx 0.8$ (80 %), and quantum efficiency was 86 %.

Hence, achieving the high conversion efficiency of the laser radiation in SRS-active self-focusing fluids in principle is possible. The effect of "absolute saturation of stimulated scattering" [7] has not fundamental nature.

The obtained value for the conversion efficiency indicates that the use of approximations of a given excitation field and the field of first Stokes SRS [5] or a given excitation field and the exponential growth of the first Stokes component [8] to describe the SRS at self-focusing is incorrect. At the same time, the model of deep depletion of exciting radiation in the self-focusing focal areas [4] gets the further experimental confirmation in the present work.

A flat decline of Stokes pulse compared with its front, in our opinion, is partially due to uncontrolled parasitic feedback, which leads to the subthreshold generation of SRS. The repeated pulses of low amplitude and longer duration (Fig. 2, d) are reinforced echo the main pulse.

Such complications can be avoided by using two-component cell. In the first long part of the cell will be self-focusing liquid with a different Raman frequency, and in the second short part – basic liquid, as in the gain stage. The two-component cell may have other advantages, because it makes better use of self-focusing dynamics [3].

The proposed and implemented simple scheme is suitable for generation of initiating subnanosecond Stokes pulses, which further can be used for more then 20 times compression of giant laser pulses with a corresponding increase in power.

Reference
1. Boyd R.W., Lukishova S.G., Shen Y.-R. Self-focusing: past and present. Fundamentals and prospects.– New York, 2009. 2. Ivanisik A. I., Malyi V. I., Ponezha G. V. Spatial-angular structure of anti-Stokes radiation formed by stimulated Raman scattering in a Kerr liquid // Optics and Spectroscopy.– 1996. – Vol. 80, No. 2. – P. 185–189. 3. Ivanisik A. I., Malyi V. I., Ponezha G. V. Stimulated Raman scattering in self-focusing environments: new methods for experimental studies // Bulletin of Taras Shevchenko national university of Kyiv. Series: Physics & Mathematics. – 1997. – No. 4. – P. 239–248. 4. Ivanisik A. I., Malyi V. I., Ponezha G. V. Effect of Self-Focusing on the Angular Spectra of Stimulated Raman Scattering // Optics and Spectroscopy.– 1998. – Vol. 85, No. 1. – P. 78–84. 5. Lugovoi V. N., Prokhorov A. M. Contribution to the theory of stimulated Raman scattering in focused light beams // JETP.– 1975. – Vol. 42, No. 1. – P. 42–46. 6. Smirnov V. G. Unconventional principles for designing high-power lasers with nonlinear frequency converters // Quantum electronics. – 1993.– Vol. 23, No. 5. – P. 361–379. 7. Sokolovskaya A. I., Kudryavtseva A.. D, Brekhovskih G. L. New optical phenomena at Raman light scattering in condensed matter // FIAN proceedings. – 1991. – Vol. 212. – P. 16–37. 8. Venkin G. V., Klyshko D. N., Kulyuk L. L. Angular structure of higher components of stimulated Raman scattering of light // Quantum electronics. – 1977.– Vol. 7, No. 5.– P. 550–553. 9. Woodbury E. J., Ng W. K. Ruby laser operation near IR // Proc. IRE.– 1962. – Vol. 50. – P 2367–2369.

А. Іванісік , канд. фіз.-мат. наук, П. Коротков, д-р фіз.-мат. наук,
Київський національний університет імені Тараса Шевченка, радіофізичний факультет, кафедра медичної радіофізики
Г. Понежа, канд. фіз. мат. наук, Національна академія статистики, обліку та аудиту, економіко-статистичний факультет

СУБНАНОСЕКУНДНІ ІМПУЛЬСИ ВИМУШЕНОГО КОМБІНАЦІЙНОГО РОЗСІЮВАННЯ ЛАЗЕРА
З МОДУЛЯЦІЄЮ ДОБРОТНОСТІ РЕЗОНАТОРА ЗА САМОФОКУСУВАННЯ

Результати експериментальних досліджень підтверджують перспективність використання самофокусуючих середовищ для створення високо ефективних перетворювачів лазерного випромінювання на основі вимушеного комбінаційного розсіювання. Показано, що завдяки динаміці самофокусування, в таких перетворювачах можна змінити частоту та за простою схемою більше, ніж у десять разів, компресувати гігантські імпульси багатомодових лазерів. Запропонована та використана схема придатна для генерації ініціюючих субнаносекундних стоксових імпульсів, які далі можуть використовуватися для компресії гігантських лазерних імпульсів з відповідним зростанням потужності.
Ключові слова: лазер, самофокусування, вимушене комбінаційне розсіювання.

А. Иванисик, канд. физ.-мат. наук, П. Коротков, д-р физ.-мат. наук,
Киевский национальный университет имени Тараса Шевченко, радиофизический факультет, кафедра медицинской радиофизики
Г. Понежа, канд. физ.-мат. наук, Национальная академия статистики, учета и аудита, Экономико-статистический факультет

СУБНАНОСЕКУНДНЫЕ ИМПУЛЬСЫ ВЫНУЖДЕННОГО КОМБИНАЦИОННОГО РАССЕИВАНИЯ ЛАЗЕРА С МОДУЛЯЦИЕЙ ДОБРОТНОСТИ РЕЗОНАТОРА ПРИ САМОФОКУСИРОВАНИИ

Результаты экспериментальных исследований подтверждают перспективность использования самофокусующих сред для создания высоко эффективных преобразователей лазерного излучения на основе вынужденного комбинационного рассеивания. Показано, что благодаря динамике самофокусирования, в таких преобразователях можно изменить частоту и с использованием простой схемы компрессировать, более чем в десять раз, гигантские импульсы многомодовых лазеров. Предложенная и использованная схема применима для генерации инициирующих субнаносекундных стоксовых импульсов, которые далее могут использоваться для компрессии гигантских лазерных импульсов с соответствующим возрастанием мощности.
Ключевые слова: лазер, самофокусировка, вынужденное комбинационное рассеивание.

O. Ivanyuta, Ph.D.
Department Electrophysics, Faculty of Radiophysics,
Taras Shevchenko National University of Kyiv

CHARACTERIZATION OF FULLERITY DERIVATIVES FOR ORGANIC PHOTOVOLTAICS

The fullerity C_{mn} derivatives were prepared by light illumination and ozonolysis of C_{60} gel solution. Experimental investigation was carried by UV-vis, IR, Raman spectroscopy, XPS and AFM. The structure of C_{mn} derivatives in gel solution (aggregates with hydrated shell) was studied. I present results from initial screening of the candidates based on informatics quantitative structure – property relationships, their comparison with results from density functional theory calculations about the effect of donor-acceptor architectures on the efficiency of the photovoltaic device.The comparison of spectral features for C_{mn} derivatives with the data for the adsorbed layers allowed to detect a series of C_{mn} hydroxyl group of derivatives.
Keywords: fullerity fullerol, hydroxyl-, epoxy-, keto- derivatives, electronic structure, surface-enhanced infrared absorption.

Introduction. Organic photovoltaic devices appear considerably cheaper and simpler in application, than traditional elements. Distribution of this technology is restrained by two important factors: not high (less than 9 %) efficiency of transformation and small works. It is considered that their commercial prospects depend on that, whether they will manage to attain ten percent efficiency at the simultaneous increase of calculation resource to ten thousand clock. These devices have recently reached 15 % efficiency and lifetimes close to 20 years; the search for the best (co)monomers for donor polymers being based on exacting experimental synthesis (Fig. 1).
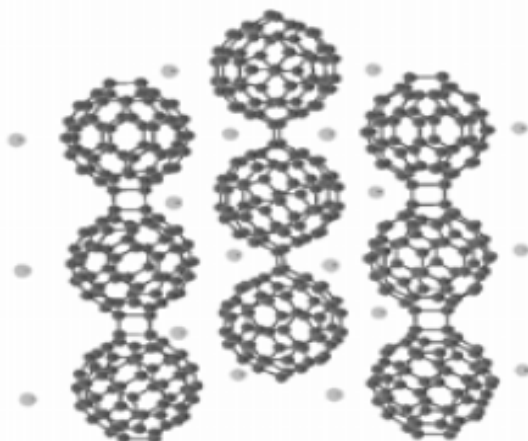
Fig. 1. Fullerity C_{m60} in polymer chains [1]

The design, automation and calculation of million organic molecules allow the screening of the best candidates for further study. Current applications of biosolutions with fullerity C_{m60} and they derivatives in molecular electronics are based on their behavior as active photosensitizer [1÷5]. These features originate from known energy levels diagram (Fig. 2) of the photosensitized generation of singlet and triplet. Fullerity C_{m60} and its derivatives can be photosensitizer due to a strong absorption of light throughout the UV and visible regions and the low energy

gap between the excited singlet and triplet states ($5,8 \cdot \text{kcal/mol}$) facilitating efficient intersystem crossing. High yield of the triplet state, > 95%, provides an efficient generation of singlet excite. Also, C_{60} is a acceptor of photoelectrons with the ability to accommodate up to several electrons reversibly [1, 6].
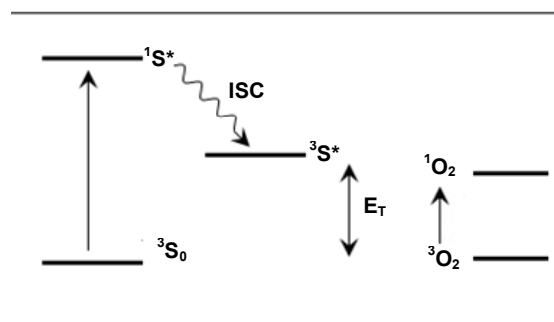
Fig. 2. Diagram of the energy levels in the photosensitized generation of singlet ($^1O_2$). ^1S, $^1S^*$, $^3S^*$ are the singlet ground state, the singlet excited state, and the triplet excited state, respectively, of the sensitizer S (C_{60}). $^3O_2$ and $^1O_2$ are the triplet ground and singlet state, respectively, of oxygen. Next transitions correspond: $^1S \to {}^1S^*$ absorption; $^1S^* \to {}^3S^*$ intersystem crossing (ISC); $^3S^* + {}^3O_2 \to {}^3S + {}^1O_2$ energy transfer. The energy transfer is possible if $\Delta E_T > 100 \, \text{kJ/mol}$ [1]

Physical and chemical properties of fullerity C_{m60} and they derivatives in gel solutions such as their structure (aggregates with hydrated shell), chemical and electronic structure were studied recently in respect to the photoinduced change transfer [1÷5]. However, experimental investigation of the behavior of fullerity C_{m60} showed that it can be easily modification over light and very short time of charge transfer from donor to acceptor occurs [5, 8]. Also, the singlet excited exits very short time and these systems do not have applications in molecular electronic. Polymeric derivatives of fullerites in solutions

also are of importance as photosensitizers, however their use in dissolutions needs special confirmations [3, 11].

In this work, synthesized gel soluble with fullerity C_{m60} derivatives by UV light illumination and ozonolysis of fullerene C_{60} gel solution. I consider also novel experimental data verifying hypothesis about possibility to prepare stable fullerity C_{m60} derivatives in gel solutions on C_{60} colloids. The comparison with the results of recent publication on fullerity C_{m60} [8÷12] was carried out. I present spectroscopic evidence of formation hydroxyl-, epoxy- and keto- derivatives and discuss variation of electronic structure of C_{m60} molecule associated with additions of the -O and -HO containing functional groups.

Experimental. I will show how the modification the electronic properties of the transparent electrode can be used to change the geometry of organic photovoltaic devices and build solar cells that do not require the use of low-work function electrodes. At the receipt of organic films the method Lengmyur - Blodzhett (a method allows to put in order and orient molecules in monolayer by the set appearance) arises up problem of their thermal instability and distributions, appearing at the transfer of tape on samples [13, 21]. In addition, thickness of such tapes and, consequently, the stake of eaten up light is small. It does difficult the receipt of functional photo-electric devices on such organic tapes. Organic elements with more high efficiency of transformation (to 11 %) it is possible to get using the method of self organizations molecules, but from complication of this method the industrial production these devices is eliminated [19]. In order to study formation of gel solutions with C_{m60} hydroxyl-, epoxy- and keto-derivatives I prepared two types of C_{m60} gel solutions which from toluene C_{m60} solution followed by evaporation of the toluene overlayer spread on the strong and polymer surface [13, 15]: this C_{m60} gel solution was illuminated by UV light from a standard bacterium dead lamp in air, $T = 300\,K, 1\,h$. The tin layer gel solution was ozonolysis during 30 min, the toluene layer was evaporated on the strong and polymer surface, assisting the transfer of C_{m60} derivatives from toluene solution [3, 14]. Also, I studied C_{m60} derivatives in two toluene solutions: (1) products formed after ozonolysis C_{60} toluene solution were repetition dissolved in toluene (a saturated solution was produced); (2) the toluene solution (1) was illuminated by UV light in air by eximer laser $280\,nm$, $T = 300\,K, 1\,h$.

Absorption spectra of these products in gel and toluene solutions were recorded with double beam spectrometers Jasco V-570 or UV-2401PC in quartz cavettos with the range $190 \div 2500\,nm$ at $T = 300\,K$. Raman spectra of these products in toluene solutions in quartz glass cavettos were recorded by double monochromator DFS-24 or CT-25C with $514,5\,nm$ excitation light of an Ar laser in range of the wave numbers $11200 \div 1500\,cm^{-1}$ at $T = 300\,K$.

Two types of C_{m60} derivatives in gel solutions were used for the fabrication of adsorbed layers on fianit and Al_2O_3 (100) substrates. Typically, $0,2 \cdot ml$ a solutions was dropped on a cleaned surface of TlBr (36 %)-TlJ (64 %) monocrystals and a specially treated surface Al_2O_3 (100) wafers (procedure used in [13]), and samples were dried in air at $T = 300\,K$ in dark. The samples with adsorbed layers were studied with IR spectroscopy (fianit substrate) and XPS (Al_2O_3 (100) substrate). The SPECORD 75 IR Zeiss spectrometer for transmission spectra measurements in the range wave numbers $250 \div 4000\,cm^{-1}$ and the combined spectrometer including XPS equipment with UV radiation ($h_\upsilon = 1355 \cdot eV$) were used. Morphology of the adsorbed layers was studied with atomic force microscopy (AFM) at ambient conditions in the tapping mode [7, 10].

Results and discussion. Fullerity does not differ in high chemical activity [9]. To the moment of beginning studies in the world were not undertaken a systematic works on research of possibility forming fullerity C_{m60} the uncovalently constrained complexes, their physical properties were not studied. A few works were sanctified to the study of cooperation molecules in solutions [16, 18]. Fullerity possess photoconductivity in a spectral range optimal for creation of solar elements.

Basic efforts were concentrated on the study of the covalently-constrained systems of artificial photosynthesis. There were not works on the receipt of such structures in a thin film variant. An organic semiconductor donor-acceptor complex C_{m60} is perspective material for the receipt of molecular by volume heterostructures, thin films heterotransitions and creation of photovoltaic devices. In such solar cells both electrodes are comprised of conducting polymers that are modified to become either hole or electron collecting electrodes. Quantum-chemical calculations showed that complex C_{m60} formed the uncovalently constrained molecular complex, energy of connection that grows and equilibrium distance diminishes among Mg, Zn. The complete charge components complexes is expected. In particular, the realization of surface-enhanced infrared absorption (SEIRA) permitted one to speak of a unified field of surface-enhanced vibrational spectroscopy (SEVS), supported by the enhanced Raman and infrared techniques. Enhancement by SEIRA depends on the size, shape, and particle density of the selected metal island films. In the most widely used Al_2O_3 (100) configuration, film morphology is influenced by surface structure of the supporting substrate, as well as by the experimental conditions used during the film fabrication. An exact count gives the value of transfer charge of C_{m60} - TPP 0,002 elementary charge, in the complexes of C_{m60} - MgTPP and C_{m60} - ZnTPP – 0,2 and 0,4 elementary charge, accordingly. The materials of the first group allow for transmission and/or reflection spectra, while the others are only adequate for external reflection measurements. Notably, low reflective materials could be optically favorable due to a reduced distortion of the band shape in the corresponding SEIRA spectrum. The spectrum photoabsorption C_{m60} lies in the length range waves $280 \div 680\,nm$ and a quantum exit, being probability formation of electron - ionic pair at absorption one photon, 0,9 makes (Fig. 3). The absorption bands with maxima at 527, 573, 1088, 1183, 1220 and $1425\,cm^{-1}$ were revealed in IR spectra of the C_{m60} derivatives layer formed by UV light illumination in air (Fig. 3, b). The maxima at 527, 573, 1183 and $1425\,cm^{-1}$ correspond to the vibration modes of C_{m60} molecules [4, 16]. The bands are broad testifying that some derivatives can appear in water solution as the result of photooxidation [9], e.g. of $C_{60}O$ (epoxide) and $C_{60}(-OH)_k$ (fullerol).
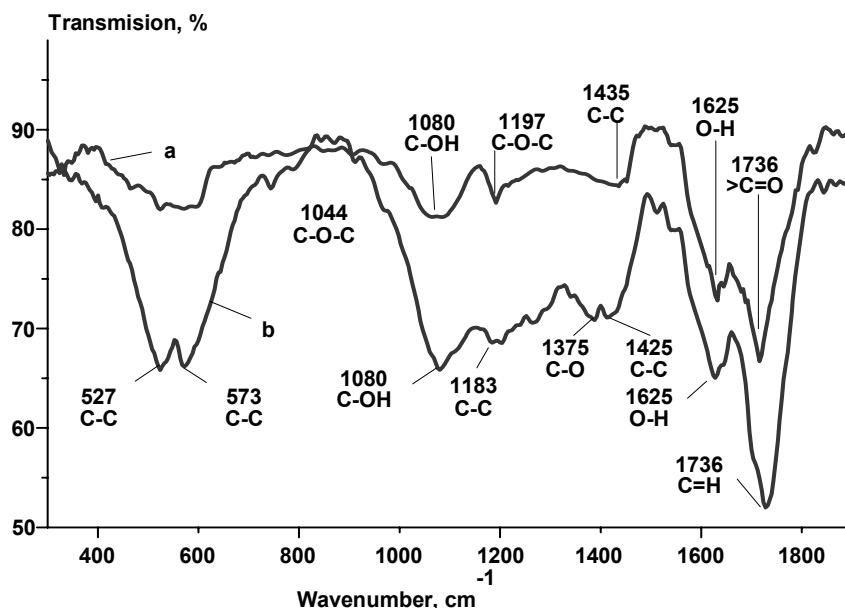
Fig. 3. SEIRA transmittance spectra of C_{m60} derivatives in adsorbed layers on Al_2O_3 (100) substrate from fullerene C_{60} derivatives formed by the different methods: a – ozonolysis; b – UV light illumination in air. The positions of the absorption bands for vibrational modes corresponded to $> C\text{-}O$, $> C = O$, C-O-C, C-OH, -OH groups [3, 17] and to vibrational modes of C_{60} molecules in gel solution [22] are marked. The insert is the spectrum (a) in the range $300 \div 1900$ cm^{-1}

Polymerization fullerene C_{60} under the action of light radiation and formation insoluble in organic solvents tape allow using fullerene as new material for photo resistance cells. The band at 1080 cm^{-1} may be attributed to vibrations of C-OH bonds. The vibration mode of C-O bonds in epoxides appearing at 1374 cm^{-1} was revealed also. The vibration mode at 1376 cm^{-1} is attributed to vibrations of $> C\text{-}O$ bonds in epoxides, at 1197 cm^{-1} does vibrations of C-O-C ester groups, and the intensive band at 1736 cm^{-1} looks as contribution due to ketone group $> C\text{-}O$ [7, 18]. A prolonged illumination of this layer during 4 h at air (relative humidity 70 %) caused destruction of the part of C-OH bonds in $C_{60}(-OH)_k$ since in the IR spectrum the intensity of 1380 cm^{-1} vibration mode strongly decreased. This result confirms that part of $C_{60}(-OH)_k$ bounds can be destroyed. In IR spectra of the layer produced by ozonolysis absorption bands with maxima at 1197, 1375, 1646, 1736, 3226 and 3421 cm^{-1} occurred (Fig. 4). The bands at 1620 and 3306 cm^{-1} can be attributed to deformation and stretching vibrations of adsorbed -OH groups, correspondingly. The other vibration mode of C-OH also makes the contribution in range $3290 \div 3300$ cm^{-1}.

This was confirmed also by comparison of the Raman spectrum C_{m60} derivatives formed by ozonolysis and redissolved and formed in gel by UV light illumination in air at $T = 300$ K. I revealed that in the first spectrum the peak at 1437 cm^{-1} and in the second spectrum the peaks at 1443 and 1461 cm^{-1} appear. Assuming that the peak at 1437 cm^{-1} corresponds to the peak at 1443 cm^{-1} in the second spectrum, the position of the peaks in the first and the second spectrums can be due to ketone and epoxides groups, respectively. This assumption based on the

comparison of the positions of the peak at 1461 and 1469 cm^{-1} which is known for solid C_{m60} and C_{60} molecule [4, 16]. The position of these peaks (at 1443 and 1461 cm^{-1}) can inform on different degree C_{60} oxidation in these two solutions. The next evidence of possible formation of C_{m60} derivatives tailed by $> C\text{-}OH$ and $> C = O$, C-O-OH, C-O-C groups in the adsorbed layers was obtained from the data of XPS experiment for C1s photoemission line (Fig. 5). The spectrum was deconvoluted through the least-squares procedure fitting raw spectra to Gaussians. For C_{m60} derivatives formed by ozonolysis the positions of Gaussian maxima are $h_b = 285,2 \cdot eV$, 285,6, and $h_b = 285,8 \cdot eV$. The reference binding energy of C-C bonds in C_{60} is $285,2 \cdot eV$ [10, 19], and for C-OH bonds the values $h_b = 286,5 \cdot eV$ and $h_b = 285,6 \cdot eV$ can be assigned to C-O or C = O, respectively [11].

For the sample produced by UV light illumination in air the energy positions of Gaussians for the C1s line are 285,2, 285,4, 286,8, 287,7 $\cdot eV$ (Fig. 6). These maxima were assigned to C-C bonds in C_{m60} ($h_b = 285,2 \cdot eV$), C-OH bonds ($h_b = 285,4 \cdot eV$), in C = O or O-C-O bonds ($h_b = 285,6 \cdot eV$) and in C-O-OH bonds ($h_b = 287,7 \cdot eV$) [10, 12]. The energy position Gaussian maximum at $h_b = 287,7 \cdot eV$ can correspond to the mono-oxygenated carbon in fullerol [12, 18]. These conclusions mainly confirmed by data for O1s photoemission line those will be publish elsewhere. Thus, these results indicate on formation of $> C\text{-}OH$, $> C = OH$, C-O-OH, $> C = O$, C-O-C bonds for fullerene C_{60} oxygen derivatives, and the skeleton of C_{m60} molecule, probably, is not broken.
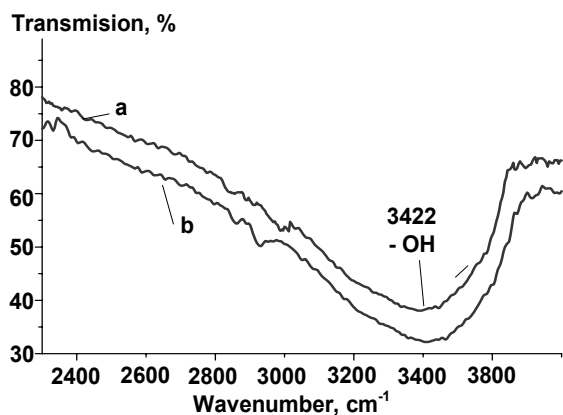
Fig. 4. SEIRA transmittance spectra of C_{m60} **derivatives**

in adsorbed layers on Al_2O_3 **(100) substrate from** C_{60}
derivatives formed by the different methods: a – ozonolysis;
b – UV light illumination in air.

The insert is the spectrum in range $2300 \div 3900$ cm^{-1}.

The vibration mode at 3422 cm^{-1} **was attributed to stretching**
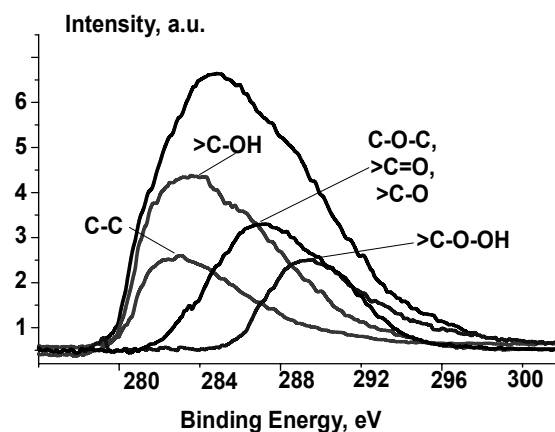**vibrational mode of adsorbed** -OH **groups**

Fig. 5. C1s XPS spectra C_{m60} **derivatives**

in adsorbed layers on Al_2O_3 **(100) formed by the different**
methods ozonolysis in air. The positions of the peaks are
centered at binding energy corresponded to $>C\text{-}OH$, C-C,
C-O-C, $>C=O$, $>C-O$, C-O-OH **bonds**
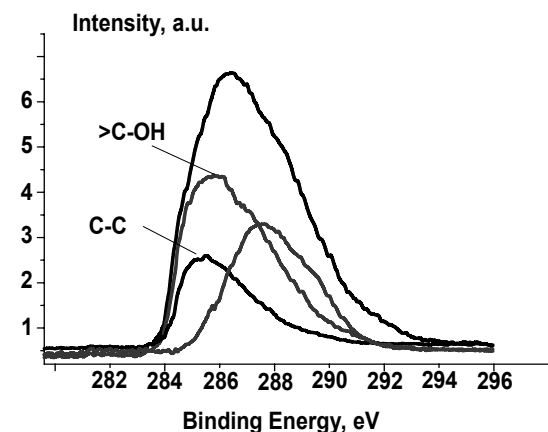
Fig. 6. C1s XPS spectra of C_{m60} **derivatives in adsorbed**

layers on Al_2O_3 **(100) formed by the different methods UV**
light illumination in air. The positions of the peaks are centered
at binding energy corresponded to $>C\text{-}OH$, C-C **bonds**

Because, the value of binding energy for C-C bond ($h_b = 285, 2 \cdot eV$) are near to the value respective the bonds on the skeleton C_{m60}. Using the above analysis of absorption bands in IR and XPS data for C_{m60} derivatives prepared by ozonolysis (Fig. 3, 4 and Fig. 6) corresponding to C_{m60} molecule tailed by ketones ($>C=O$), esters groups (C-O-C), and hydroxyl ($>C\text{-}OH$) the percent ratio of these component was evaluated: $>C=O$ – 34%, $>C\text{-}OH$ – 22 % and C-O-C – 19,5 %. These C_{m60} tailed molecules shown in Fig. 6.

The aggregates of C_{m60} derivatives on substrates From our earlier AFM studies [3, 15] for C_{m60} oxygen and hydroxyl group derivatives in adsorbed layer on dielectric substrates formed over UV light illumination in air established that this layer contains planar orientation aggregates with length up 135 Å including the two C_{m60} molecular clusters. Every cluster with 11 molecules of C_{m60} (28 Å) has the diameter up 72 Å. Between these aggregates small aggregates appear with length up 50 Å from two $(C_{60})_{11}$ molecular clusters with the diameter 25 Å and/or crystallites C_{m60} with linear size up 28,6 Å. These cluster systems form one-dimensional chains due to self-organization over UV light illumination.

Several interesting nanoarrays C_{m60} were also found in UHV environment. Hydrogen bond based network structures provide a potential pathway to the design of host-guest interfaces, because the cavity size can be controlled through careful selection of the component molecules. The formation of a self-assembled bimolecular network C_{m60} through hydrogen bonds by co-adsorption of perylene tetra-carboxylic di-imide (PTCDI) and 1, 3, 5 –triazine – 2, 4, 6 triamine (melamine) was reported [11, 20]. AFM images obtained by within the framework of this work for adsorbed layer from C_{m60} derivatives formed by ozonolysis show, in contrast to described morphology of the adsorbed layer with C_{m60} derivatives formed over UV light illumination in air, disordered spherical particles with diameter $80 \div 120$ nm which can be evaluated as the clusters of C_{m60} derivatives comprising $114 \div 171$ molecules C_{m60} (7 Å).

Electronic spectra of C_{m60} derivatives to show in Fig. 7. On the basis of these result I propose the energy diagrams and electronic transitions in C_{m60} [3, 14]. and their correlation with possible electronic structure of C_{m60} molecules tailed by -O and -OH group. Three and two intense broad absorption bands with maxima at 220, 265, 345 nm and with minimum at 241, 284, 336 nm (Fig. 7, **a**) dominate in the range $190 \div 410$ nm for the spectra in gel and toluene solutions. The energy positions of these maxima correspond to allowed electron transitions $h_g, g_g \rightarrow t_{2u}$ (218 nm), $h_u \rightarrow h_{2g}$ (264, 284 nm) and $h_g, g_g \rightarrow t_{1u}$ (340, 336 nm) (Fig. 7). The shifts between the maxima in gel and toluene solutions are 20 and 40 nm. They can be associated with the hydration of C_{m60} in gel solution influencing an occupation of lowest state conductive band, which created by molecular states t_{1u}. It is important also for electron transitions $h_g, g_g \rightarrow t_{1u}$ and / or their hydrated aggregates self-formation [4, 5]. The

revealed morphology of adsorbed layer from this solution on substrate confirms it. The lowest allowed electron transition $h_u \rightarrow t_{1g}$ to excited state T_{1u} at 408 nm is revealed only in spectra of the C_{m60} derivatives in toluene formed by ozonolysis. This electron transition is allowed only for solid C_{m60} (Fig. 8) [4, 21].
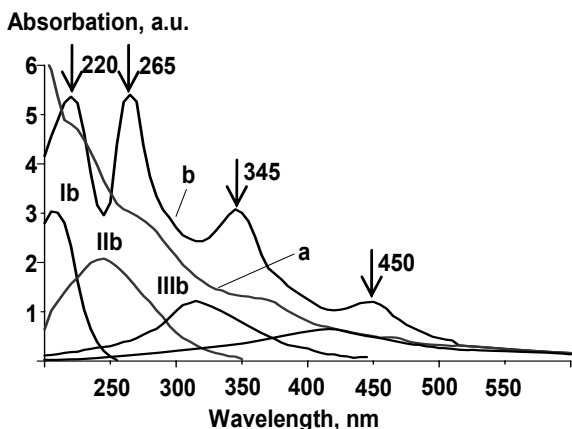
Fig. 7. The absorption spectra of solutions produced by the following procedures: a – UV light illumination of C_{m60} gel solution in air; b –ozonolysis of C_{m60} in toluene solution. Deconvolution of the spectrum (b) shows positions of four bands, residuals are scarcely evident. The positions of Ib, IIb, IIIb bands are at 203, 242, 312, 421 nm, respectively. The insert is these absorption spectra in the energy scale ($1,5 \div 2,5 \cdot eV$)
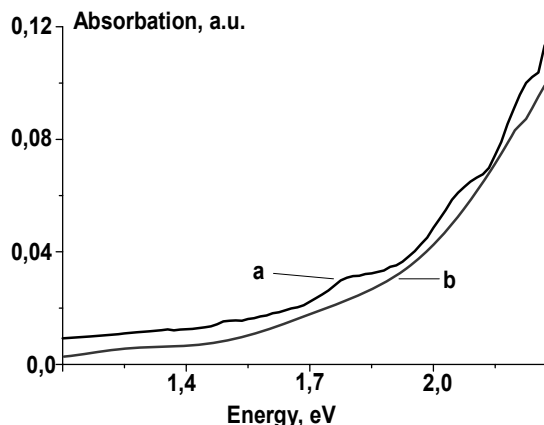
Fig. 8. The positions of the absorption edges in spectra (a) and (b) of C_{m60} derivatives in gel can be revealed at 1.7, $1.8 \cdot eV$, respectively

In the range $420 \div 640$ nm the bands can be associated with electronic transitions to the excited states. The spectra of C_{m60} derivatives in gel and in toluene show the weak bands near 450, 621 nm (Fig. 9, d) and 536, 598, 624 nm (Fig. 10, a), respectively. The weak band at 450 nm in spectrum in gel corresponds to minimum absorption near 440 nm in spectrum in toluene (curves d and a, respectively), and the known electronic transition $2,75 \cdot eV$ (450 nm) can be identified as $h_u \rightarrow t_{1g}$ transitions in solid C_{m60} for these maxima [5, 14]. Also, the weak bands near 620 nm (621 and 624 nm) occur in both spectra. It is known that in the range

$490 \div 640$ nm ($1,9 \div 2,5$ eV) the weak absorption takes place associated with electric dipole-forbidden transitions between the one-electron HOMO level with h_u symmetry and one-electron t_{1u} LUMO level. Only for the solution of C_{m60} derivatives in toluene the weak absorption at 536 and 598 nm are (Fig. 9, a) [3, 19]. I suppose that the spectrum in Fig. 6 can characterize the solid C_{m60} rather than free C_{m60} molecules. These absorption maxima are shifted (up to 10 nm) in comparison with known positions of the solid C_{m60} (460 and 625 nm , respectively).
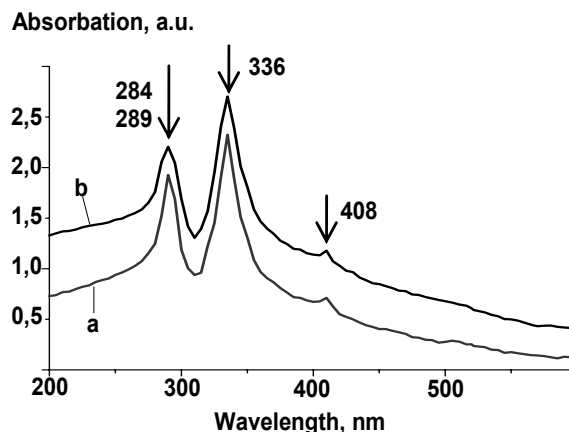
Fig. 9. Absorption spectra of C_{m60} (a) and C_{60} oxygen derivatives (b) in gel solution
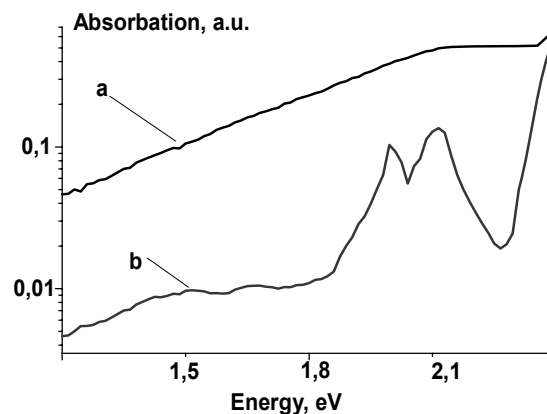
Fig. 10. The positions of the absorption edges for the spectra (a) and (b) can be evaluated at 1.95 and $2,11 \cdot eV$, respectively. The insert is these absorption spectra in the energy scale ($1 \div 3 \cdot eV$)

The difference between shapes of absorption spectra in the range $410 \div 550$ nm for C_{m60} derivatives in gel and toluene can be interpreted assuming that $C_{m60}O_n$ absents in toluene, the minimum at 440 nm occurs (Fig. 11, a). Hence, the higher absorption in this range for spectra prepared without (Fig. 11, d) and with ozonolysis of initial solution of C_{m60} derivatives in toluene (Fig. 11, c) confirm that $C_{m60}O_n$ can be in both solutions. In gel solution of C_{m60} derivatives prepared without ozonolysis of initial solution of C_{m60} in toluene the features due to $C_{m60}O_n$ are observed (that was showed in analysis of IR spectra in Fig. 3, **a**) [4, 12].
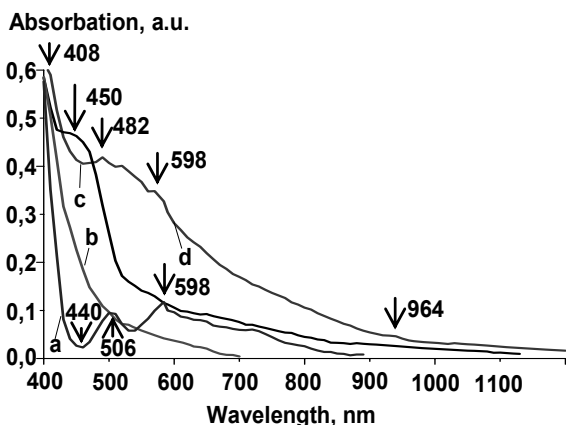
Fig. 11. The absorption spectra of C_{m60} **in toluene solution (a) and** C_{m60} **derivatives in gel solutions prepared by UV light illumination of gel solution in air (d) and toluene solution (c), (b) corresponds to gel solution prepared from ozonolysed** C_{m60} **toluene solution**

In order to built energy diagram (Fig. 12) of the electronic transitions corresponding to the above experimental data we take the known calculated value for the HOMO–LUMO gap in C_{m60} single molecule equal to ~1.5 eV [14, 22] and assume that the HOMO – LUMO electronic transition in hydrated C_{m60} and $C_{60}O$ molecules and aggregates with ordered structure in water is $1{,}7 \cdot eV$ (insert in Fig. 8, **a**) and similar electron transitions in C_{m60} molecules in toluene is at $1{,}8 \cdot eV$ (insert in Fig. 9, **a**). The comparison between electronic spectra of C_{m60} derivatives in gel solution formed by ozonolysis (Fig. 7, **b**) and C_{60} oxygen derivatives in gel solution formed over UV light illumination

in air (Fig. 7 **a**) indicates the clear difference of the first with appearance of absorption bands I**b**, II**b**, III**b**. Positions of band centers 220, 265, 345 nm are shifted to lower wavelengths as compared with those corresponding to electric dipole-allowed electron transitions between HOMO and LUMO in C_{m60} molecule (and also in their analogs in solid C_{m60}).
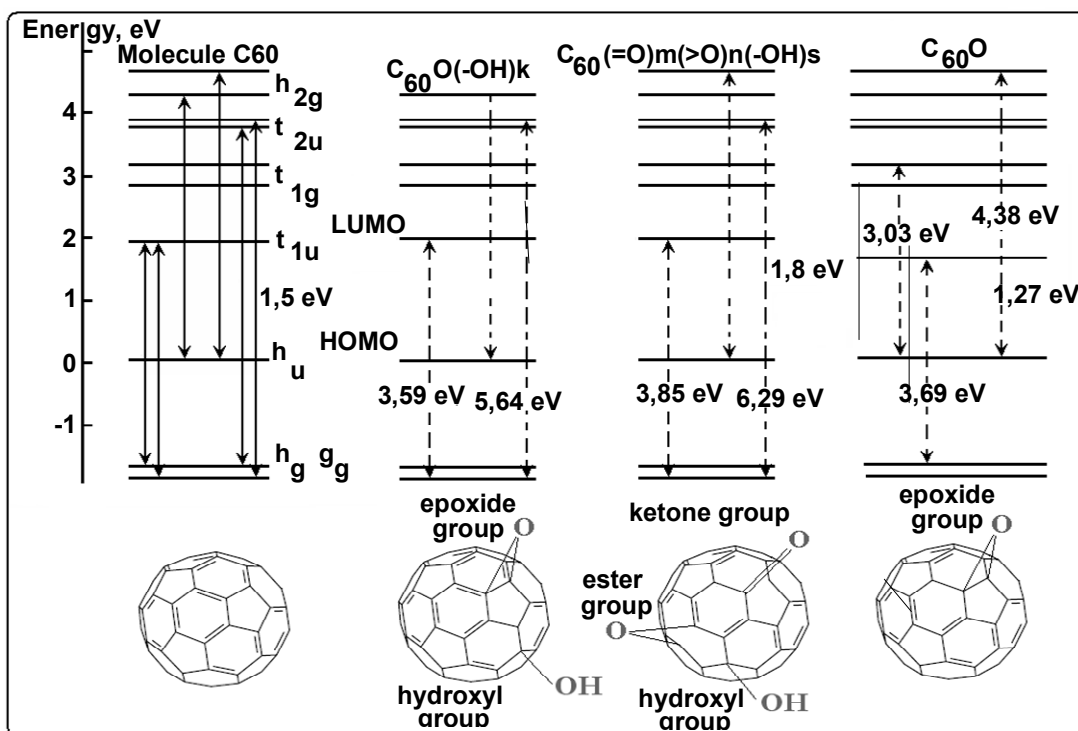
Fig. 12. IR transmittance spectra of C_{m60} **derivatives in adsorbed layers on** Al_2O_3 **(100) substrate from** C_{m60} **derivatives formed by the different methods: a – ozonolysis; b – UV light illumination in air. The positions of the absorption bands for vibrational modes corresponded to** $>C\text{-}OH$, $>C=OH$, $C\text{-}O\text{-}OH$, $>C=O$, $C\text{-}O\text{-}C$, $C\text{-}OH$, $-OH$ **groups [7, 12] and to vibrational modes of** C_{m60} **molecules are marked [3, 8]. The insert is the spectrum (a) in the range** $2500 \div 4000 \cdot cm^{-1}$. **The vibration mode at** $3306 \cdot cm^{-1}$ **was attributed to stretching vibrational mode of adsorbed** $-OH$ **groups**

The photo – reactive monolayer was formed by the adsorbate molecule bearing a ketone group and a benzophenone moiety on an Au-deposited Al_2O_3 (100) substrate. UV exposure caused the benzo phenone moiety to induce the photochemical graft reaction with a thermoplastic hydrocarbon polymer. The photo-induced graft reaction suppressed the dewetting of a polymer thin film with a C_{m60} on the Al_2O_3 (100) substrate. The dewetting suppression was achieved at an exposure dose of $5 J cm^{-2}$ at the irradiation wavelength of $254 nm$. The dewetting

suppression enabled us to fabricate reliable fine patterns of the polymer film by thermal nanoimprint lithography and the Au film by subsequent wet etching. The positions of band I**b**, II**b** and III**b** are 197, 249 and 322 nm (6.29, 4.97 and $3{,}22 \cdot eV$). These results are confirmed for the spectra of the diluted solution in gel: it leads to decrease of the absorption throughout the whole range. The observed shifts of I**b**, II**b**, III**b** bands positions were interpreted as the formation of $C_{m60}(=O_m)(>O)_n(-OH)_s$ taking into account the IR spectra in presented Fig. 3, **a,** and analysis of the

spectra of C_{m60} derivatives in gel solution, toluene (Fig. 5, 6, **a**). They are consistent also with variations of absorption features of C_{m60} molecule in after light irradiation and photolysis [11]. In Fig. 7 the electronic transitions with energy corresponding to the maxima I**b**, II**b**, III**b** for $C_{m60}(=O_m)(>O)_n(-OH)_s$ are presented. Self-assembled 2D structures of C_{m60} derivatives have been a prime target for observations by atomic force microscopy (AFM). Iobserved that molecules of C_{m60} form a 2D network on Al_2O_3 (100)substrate, driven by attractive intermolecular interactions [5, 17], while the surface migration barriers are comparatively small and charge transfer to the adsorbed molecules is minimal. On the contrary, a significant charge transfer is observed in repulsive forces between the molecules that prevent the formation of a molecular add layer network (see Fig.13). It was shown that the limiting factor in the formation of self-assembled networks C_{m60} is the nature of frontier orbital overlap and absorption interface electron transfer. Various patterns determined by the intricate interplay between directional hydrogen bonding interactions and packing forces, including chain molecule–molecule and C_{m60} substrate interactions, - demonstrated the possibility of programmed surface patterning using C_{m60} incorporating directional intermolecular interaction sites. I developed an effective and facile method for self-assembling C_{m60} molecules into hollow hexagonal nanoprisms with uniform size and shape and controllable aspect ratio [14, 16].

30 nm – line concave patterns of a polymer thin film

100 nm
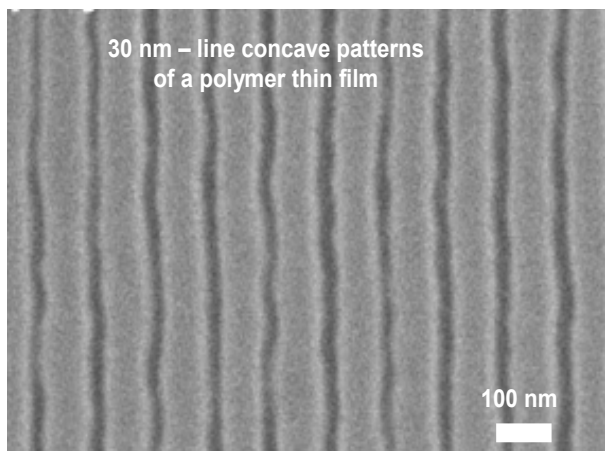
Fig. 13. The photo-induced graft reaction suppressed the dewetting C_{m60} of a polymer thin film

on the Al_2O_3 (100) substrate. UV exposure caused the benzophenone moiety to induce the photochemical graft reaction with a thermoplastic C_{m60} polymer

The following features associated with $C_{m60}(=O_m)(>O)_n(-OH)_s$ compounds presence can be pointed out in the range $400 \div 1000$ nm the spectra of C_{m60} derivatives in gel solution formed by ozonolysis in toluene and the spectra of C_{m60} derivatives in gel solution formed over UV light illumination in air (Fig. 11, **a-d**): the weak band at 408 nm corresponding to solid C_{m60} exists only in the absorption spectra of C_{m60} derivatives in toluene before and after ozonolysis (Fig. 11,**a**, **c**); the band near 450 nm with higher absorptio n as compared with curve **a** in the spectrum of C_{m60} derivatives in toluene after ozonolysis (Fig. 11, **c**);

the broad band at 482 nm in spectra of C_{m60} derivatives in toluene after ozonolysis (Fig. 11, **c**) which is remarkably shifted to shorter wavelengths compared to the band of C_{m60} derivatives in toluene after illumination (536 nm). These features of the oxidized and photolysed C_{m60} in solution were associated with $C_{m60}O$ formation [11, 15]. I can assume that HOMO-LUMO electronic transition with energies 1,9 and $1,27 \cdot eV$ (from insert in Fig. 10) can be due to C_{m60} molecular aggregates and $C_{m60}O$ in toluene, respectively. These electronic transitions for $C_{m60}O$ are are presented in Fig. 12. In the spectral range $925 \div 1000 \cdot$ nm (Fig. 11) the weak feature can be assigned if to consider $C_{m60}O^{\cdot}$ caption as a constituent of the excited $C_{m60}O$ compound, and analyze the vibration mode at $964 \cdot$ nm ($1,34 \cdot eV$). In the near – IR spectra this mode presents as the result of the electrochemical oxidation C_{m60} applying a potential sufficiently negative to cause the reduction of resulted in the regeneration of C_{m60} [6, 11].

I tested the functionality of the thermoplastic C_{m60} polymer and performed temperature - dependent conductivity measurements on the bulk powder materials.

It was the room temperature value for C_{m60} fell below the experimental limit. Therefore, no temperature dependence could be measured (Fig. 14). However, the modifying C_{m60} powder drastically increased by at least nine orders of magnitude compared to chains. Its temperature dependence resembled that of the C_{m60}, indicating that conduction occurred through a percolated three-dimensional network of C_{m60}. However, the room temperature value of the modifying C_{m60} composite did not reach the value of a C_{m60} network, which is expected to be one or two orders higher in magnitude. This indicates the existence of additional tunnelling barriers between the C_{m60}, formed by the coating around C_{m60}. As a further indication of functionality enhanced thermal stability of the composite, which decomposes in air higher. It investigated the photophysical properties of the composite and measured it's photoluminescent behavior ($\lambda_{ext} = 330 \cdot$ nm). Shows, that's a broad emission maximum modifying C_{m60} at about $410 \cdot$ nm caused by reduced groups.

Fig. 14. I-*V* characteristics of inverted C_{m60} bulk-heterojunction solar cells with and without light modification

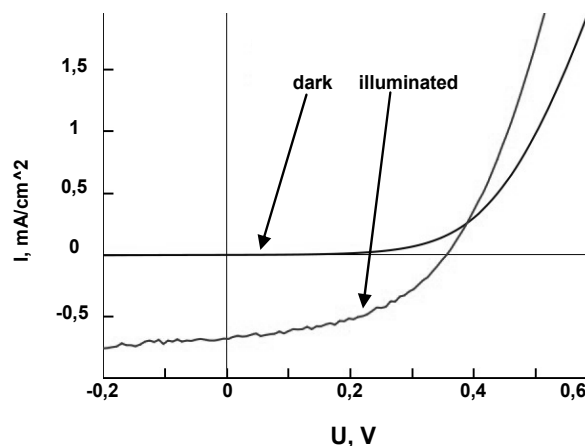Another new concept for a solid-state cell consists of a polymer organic semiconductor that combines the functions of light-absorption and charge transport in C_{m60} material. Therefore, it's able to replace both the transporting excitation. The photoinduced charge separation at the interface of an organic semiconductor has been studied in relation to photovoltaic devices. For an efficient charge generation, it is important that the charge-separated state is the thermodynamically and kinetically most pathway after photoexcitation. Therefore, it's important that the energy of the absorbed photon is used for generation of the chargeseparated state and is not lost via competitive processes like fluorescence $410 \cdot nm$. In addition, it is of importance that the charge – separated state is stabilized, so that the photogenerated charges can migrate to two of the electrodes. Therefore, the back electron transfer should be slowed down as much as possible. When an polymeric semiconductor is excited across the optical band gap C_{m60}. The excitation energies and valence band was offsets of C_{m60} this molecular semiconductor may allow electron transfer to the conduction band of an inorganic semiconductor. It's excitation energies C_{m60} are no longer created at the interface only, but throughout the whole organic material for electronic devices.

Soluble modifying C_{m60} composite has enhanced conductivity and improved thermal stability. It's also luminescent, optically active and can be processed from solutions into films, coatings and fibres. Depending on the synthesis conditions, the bithiazole based polymers exhibited optical band gaps range $1,77 \div 2,62 \cdot eV$ and the sopolymers displayed chromism within a wide span of the visible spectrum. These observations are consistent with the polymer adopting conformation. The circular dichromatic spectrum for modifying C_{m60} showed that the polymerization of aniline in the presence of C_{m60} and doping did not inhibit the polymer's ability to become optically active.

Conclusions. Finally, I will describe examples of organic solar cell architectures in which all layers are comprised of polymers that can be processed from solution. I believe that these strategies pave the way to very low-cost photovoltaic technologies with light-weight and flexible form factors. I present the spectroscopic study evidencing formation of hydroxyl-, epoxy- and keto-derivatives of C_{m60} and analyze changes in the electronic structure of C_{m60} molecule associated with additions of these functional groups. The skeleton of C_{m60} molecule is assumed not broken on the basis of IR, Raman, UV-Vis, XPS spectra of the C_{m60} derivatives. The electronic

transitions in the spectra of identified $C_{m60}O$, $C_{m60}O(-OH)_k$ and $C_{m60}(=O_m)(>O)_n(-OH)_s$ are presented (see Fig. 12). These transitions can play a role in process of new photosensitizers. The copolymers revealed short switching times and useful optical contrast respectively. These devices exhibited low switching voltages and switching times with reasonable stability under atmospheric conditions. I believe that these findings provide the basis for novel smart organic materials of great use in smart optoelectronic applications and devices.

Reference
1. Cancer and aging as consequences of un-repaired DNA damage. In: New Research on DNA Damage / Ed. by Honoka Kimura, Aoi Suzuki. – NewYork., 2008. 2. Gorchinskyi, A.; Bukalo, V.; Scharff, P. et al. Self-Formation of Nanostructures from Hydrated Aggregates and Nanocrystals of (C60)n Molecules on the Liquid Crystal Layer. // In Book: Electronic properties of novel materials – science and technology of molecular nanostructures, New York. – 1999. 3. Frontiers of nano-optoelectronic systems / Ed. by L. Pavesi, E. Busaneva. – Dordrecht., 2000. 4. Future Trends in Microelectronics. Up the Nano Creek / Ed. by S. Luryi,, Xu J., A. Zaslavsky. – NewYork., 2007. 5. Nano and Molecular electronics: handbook / Ed. by S.E. Lyshevski. - Boca Raton, 2007. 6. Nanotechnology: an Introduction to Nanostructuring Techniques / Ed. by M. Kohler, W. Fritzsche. – NewYork., 2007. 7. Surface Modification and Mechanical Properties of Bulk Silicon. Tribolgy Issues and Opportunities in MEMS. / Ed. by Scherge, M.; Schaefer, J. – Kluwer Academic Publishers 1998. 8. Burrell, A.K. Synthetic routes to multiporphyrin. // Chem. Rev. – 2001. – Vol. 101. – P. 2751–2796. 9. Heymann, D.; Bachilo, S.; Weisman, B.; Cataldo, F. at. al. C60O3 Fullerene Ozonide: Synthesis and Dissociation to C60O and O2. // J.Am.Chem.Soc. – 2000. – Vol. 122. – P. 11473–11479. 10. Heymann, D., Bachilo, S., Weisman, R., Ozonides, Epoxides, and Oxidoannulenes of C70. // J. Am. Chem. Soc. – 2002. – Vol. 124. – P.6317–6323. 11. Da Ros, T., Spallutto, G., Prato, M. Biological Applications of Fullerene Derivatives: A Brief Overview. Croatica Chemica Acta. – 2001. – Vol. 74(4). – P. 743–755. 12. Kodymová, J., Müllerová, A., Krása, J. at. al. The Role of the Oxygen Molecule in the Photolysis of Fullerenes, Fullerene Sciences and Technology. – 2000. – Vol.8. – P. 289–318. 13. Mchedlov-Petrossyan, N., Klochov, V., Andrievsky, G. Colloidal dispersions of fullerene C60 in water: some properties and regularities of coagulation by electrolytes. // J.Chem.Soc., Faraday Trans. – 1997. – Vol. 93(24). – P.4343–4346. 14. Kaesarmann, F., Kempf, Ch. Buckminsterfullerene and Photodynamic Inactivation of Viruses. // Reviews in Medical Virology. – 1998. – Vol. 8. – P. 143–151. 15. Tagmatarchis. N. Carbon-based materials: From fullerene nanostractures tofunctionalized carbon nanotubes. // Pure Appl. Chem.- 2005. – Vol. 77. – P.675–1684. 16. Scharff, P.; Risch, K.; Carta-Abelmann at. al Structure of C60 fullerene in water: spectroscopic data. // Carbon. – 2004. – Vol. 42(5-6). – P. 1203–1206. 17. Song T., Dai S.; Tam K. Aggregation behavior of two-arm fullerene-containing poly (ethylene oxide). // Polymer. – 2003. – Vol. 44. – P.2529–2539. 18. Vileno B., Sienkiewicz A., Lekka S. at. al. In vitro assay of singlet oxygen generation in the presence of water-soluble derivatives of C60. // Carbon. – 2004. – Vol. 42(5–6). – P. 1195–1198. 19. Webster R.D., Heath G.A., Voltammetric, EPR and UV-VIS-NIR spectroscopic studies associated with the one-electron oxidation of and in C60 C70 1, 1', 2, 2'-tetrachloroethane containing tri-uoromethanesulfonic acid. // Phys. Chem. Chem. Phys. – 2001. – Vol. 3. – P. 2588–2594. 20. William B. D. Dependence of electron transfer dynamics in wire-like bridgemolecules on donor-bridge energetics and electronic interactions. // Chemical Physics. – 2002. – Vol. 281. – P. 333–346. 21. William B.D., Dependence of electron transfer dynamics in wire-like bridge molecules on donor-bridge energetics and electronic interactions. // Chemical Physics.- 2002. – Vol. 281. – P. 333–346. 22. Yoshida Y. Reactivity of C60C16 and C60Brn (n = 6, 8) in Solution in the Absenceand in the Presence of Electron Donor Molecules. // J. Am. Chem. Soc. – 2000. – Vol. 122. – P. 7244–7251.

О. Іванюта, канд. фіз.-мат. наук,
кафедра електрофізики, радіофізичний факультет
Київський національний університет імені Тараса Шевченка

**ВЛАСТИВОСТІ ЗМІНЕНИХ ФУЛЕРИТІВ
ДЛЯ ОРГАНІЧНИХ ФОТО ЧУТЛИВИХ ПРИСТРОЇВ**

Змінені фулерити C_{mn} були виготовлені шляхом нерадіаційного опромінення і озонування C_{60} в гелієвому розчині. Експериментальні дослідження були проведені в ультрафіолетовому, видимому, інфрачервоному діапазону спектрів раманівською спектроскопією, XPS і АСМ. Структури змінених C_{mn} в гелієвому розчині (агрегати з гідратованими зв'язками) вивчалися. Я представляю результати від початкового вибору зразків, що ґрунтується на інформації квантової структури і супутніх властивостей, їх порівняння з результатами від обчислення щільності функціонала теорії для ефективності фотоелектричного пристрою на ефекті акцепторно – донорної архітектури. Порівняння спектральних особливостей змінених C_{mn} з даними для адсорбованих шарів дозволило виявити серії гідроксильних груп в змінених C_{mn}.

Ключові слова: фулерити C_{mn}, фулерол, гідроксіл-, епоксіл-, кето-зміни, електрона структура, збільшене поверхневе інфрачервоне поглинання.

А. Иванюта , канд. физ.-мат. наук,
кафедра электрофизики, радиофизический факультет
Киевский национальный университет имени Тараса Шевченко

СВОЙСТВА ИЗМЕНЕННЫХ ФУЛЛЕРИТА
ДЛЯ ОРГАНИЧЕСКИХ ФОТО ЧУВСТВИТЕЛЬНЫХ УСТРОЙСТВ

Измененные фуллерита C_{mn} были изготовлены путем нерадиационного облучения и озонирования C_{60} в гелевом растворе. Экспериментальные исследования были проведены в ультрафиолетовом, видимом, инфракрасном диапазонах спектров рамановской спектроскопии, XPS и АСМ. Структуры измененных C_{mn} в гелевом растворе (агрегаты с гидратированными связями) изучались. Я представляю результаты от первоначального выбора образцов, основываясь на информации о ихквантовой структуре и сопутствующих свойствах, их сравнение с результатами вычисления плотности функционала в теории для эффективности фотоэлектрического устройства на эффекте акцепторных – донорной архитектуры. Сравнение спектральных особенностей измененных C_{mn} данным для адсорбированных слоев позволило выявить серии гидроксильных групп в измененных C_{mn}.

Ключевые слова: фуллериты C_{mn}, фулерол, гидроксилы-, епоксил-, кето-изменения, электронная структура, увеличеное поверхностное инфракрасное поглощение.

A. Kotenko, post., D. Gryaznov, assist., Yu. Boyko, Ph.D.
Faculty of Radiophysics, Taras Shevchenko National University of Kyiv

OPTIMIZIATION WEB-APPLICATIONS WITHOUT USERS GENERATED CONTENT
FOR RELIABILITY AND PERFORMANCE USING NGINX TECHNOLOGY

The paper is considered to approach to develop reliable and productive web-application. Contradiction between performance, achieved by building system from different, dedicated to one task, nodes, and reliability is analyzed. Proposed technical solution based on nginx that eliminates the contradiction.

Keywords: web-applications, reliability, performance, nginx.

Introduction. Recently there has been continued growth in both the number of online users and Web applications (sites, services, social networks) [1] The growing number of users requires a web application a significant increase in performance due to the fact that the process visits to web resources has a random nature with significant fluctuations. And customer service even visiting peaks should occur at the time of the order of 1–2 seconds [7]. At the same time the web application requires reliability, so even 15 minutes disability sites lead to a significant reduction of its position in Google SERP [6].

So actual is the problem of building Web applications that have improved reliability and performance simultaneously. But these IT requirements are often those that contradict each other. This contradiction occurs because that productivity is generally associated with parallel operation. This parallel operation requires some parts of specialization that prevents duplication of their work to ensure reliability.

Implementation. In this paper we propose a technical solution that is optimal in terms of reliability and performance. As the criteria of reliability, we used a disability, as well as performance criteria – the number of components that can perform the work at once.

To construct the solution we used technology nginx [4]. Nginx is a free, open-source, high-performance HTTP server and reverse proxy. Nginx was started in 2002, with the first public release in 2004. Nginx now hosts nearly 12.18% (22.2M) of active sites across all domains. Nginx is known for its high performance, stability, rich feature set, simple configuration, and low resource consumption. [5] Scheme of the standard Nginx configuration shown in Fig.1.

As can be seen from the scheme in the standard technology Nginx configuration ensures reliable operation in the case of a single server. However, any server can fail for a number of reasons such as hardware or software failure, network failure, or even problems with the electricity in the data center.

As can be seen from the scheme in the standard technology Nginx configuration ensures reliable operation in the case of a single server. However, any server can fail for a number of reasons such as hardware or software failure, network failure, or even problems with the electricity in the data center.
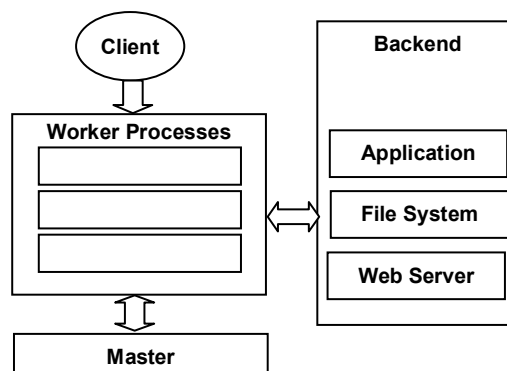
Fig. 1. Scheme of Nginx

The standard way to improve the reliability of system works is mirroring servers, and the reserve server can be located even in a different data center. In case of failure of one server it is possible to switch to another. However, the use of reserve systems can not improve the performance of the system as a whole, as the work performed by one anyway. To improve performance main and reserve servers have to serve clients simultaneously. It is clear, that in the case where users generate the content this architecture become complex because it requires synchronization of content between servers when the user change it. But there are a number of services, such as [3], where it is not necessary to modify the stored content in response to the user actions. The proposed solution is designed for these systems. The main idea of solution is to create mirrored copies of the service, access to which is performed under round robin, implemented by domain name system service [2]. Scheme of the round robin is shown in Fig. 2.

The main problem of this solution is that it requires storing complete copy of the data on all used servers and therefore takes up more memory than the parallel operation of specialized copies. As the solution of this problem it is proposed to use natural feature of database cache – keeping in memory the data that are used more commonly. But in order to work, data used to serve client's request has to hit the cache in the server. So, on every server users requests have to be limited to some subset, of
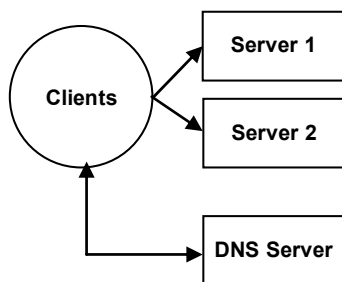
Fig. 2. Scheme of the round robin

all requests, and every server handles it's own part. To implement this mechanism it is proposed to use Nginx server. It is flexible enough to define by configuration how to distribute requests to servers to make cache effective. Also in case of failure of one of them, requests are handled by working servers. This detection efficiency of the server is done automatically by analyzing the responses. The general scheme of the proposed solution is shown in Fig. 3. Example of Nginx configuration is shown below.

```
upstream application_application {
        server 127.0.0.1:8090;}
upstream local_application {
        #prefer local application over remote
        server 127.0.0.1:81;
        server server_2:81 backup;}
upstream remote_application {
        #prefer remote application over local
        server server_2:81;
        server 127.0.0.1:81 backup;}
server {
        listen 81;
        location / {
        proxy_set_header Host $host;
        proxy_pass http://application_upstream;}
}
server {
        #handle client's requests
        listen 80;
        server_name server_1;
        location / {
        #query classification.
        if ($arg_query !~* "^[0-9a-n]") {
                proxy_pass http://remote_application
                break;}
        if ($arg_query ~* "^[0-9a-n]") {
                proxy_pass http://local_application;
                break;}}}
```


Fig. 3. The proposed solution in general

Conclusions. The proposed solution can improve overall system performance by parallelizing work on several servers and effectively using resources of all processors and of total memory of all servers. Also it increases reliability of all system. On failure of a server response time increases, but overall the service keeps running smoothly.

Reference
1. Barney W. Origins, Growth, and Geographies of the Global Internet / Barney W. // SpringerBriefs in Geography. – 2013. – № 1. – P. 9–44. 2. Brisco T. DNS Support for Load Balancing [Electronic resource] / Brisco T. – Mode of access: http://tools.ietf.org/html/rfc1794. 3. Maps locale search [Electronic resource]. – Mode of access: http://maplos.com/. 4. Nginx official page [Electronic resource]. – Mode of access: http://nginx.org/. 5. Nginx official wiki [Electronic resource]. – Mode of access: http://wiki.nginx.org/Main/. 6. Official Google help [Electronic resource]. – Mode of access: http://www.youtube.com/watch?v=qXrwyTGOf1E/. 7. Waiting times in quality of experience for web based services / [Egger S., Hossfeld T., Schatz R., Fiedler M.] // Institute of Electrical and Electronics Engineers – 2012.

А. Котенко, асп., Д. Грязнов, асист., Ю. Бойко. канд. фіз.-мат. наук, доц.,
Київський національний університет імені Тараса Шевченка

ОПТИМІЗАЦІЯ ВЕБ-ДОДАТКИ ЗА НАДІЙНІСТЮ ТА ПРОДУКТИВНІСТЮ З ВИКОРИСТАННЯМ NGINX ТЕХНОЛОГІЇ У ВИПАДКУ ВІДСУТСТВІЯ КОНТЕНТУ, ЩО ГЕНЕРУЄТЬСЯ КОРИСТУВАЧАМИ

У статті розглянуто підхід до побудови відмовостійкого та продуктивного веб-застосунку. Розглянуто протиріччя між продуктивністю, яка досягається за рахунок спеціалізації вузлів системи, та надійністю системи. Запропоновано технічне рішення на основі nginx, яке знімає це протиріччя.
Ключові слова: веб-застосунки, надійність, продуктивність, nginx.

Котенко А.С., асп., Грязнов Д.Б., ассист., Бойко Ю. В., канд. физ-мат. наук.,
Киевский национальный университет имени Тараса Шевченко

ОПТИМИЗАЦИЯ ВЕБ-ПРИЛОЖЕНИЙ ПО НАДЁЖНОСТИ И БЫСТРОДЕСТВИЮ С ИСПОЛЬЗОВАНИЕМ ТЕХНОЛОГИИ NGINX В СЛУЧАЕ ОТСУТСТВИЯ ГЕНЕРИРУЕМОГО ПОЛЬЗОВАТЕЛЯМИ КОНТЕНТА

В статье рассмотрен подход к построению отказоустойчивых и производительных веб-приложений. Рассмотрено противоречие между производительностью, достигнутую за счет специализации узлов и надёжностью системы. Предложено техническое решение на основе nginx, которое снимает противоречие.
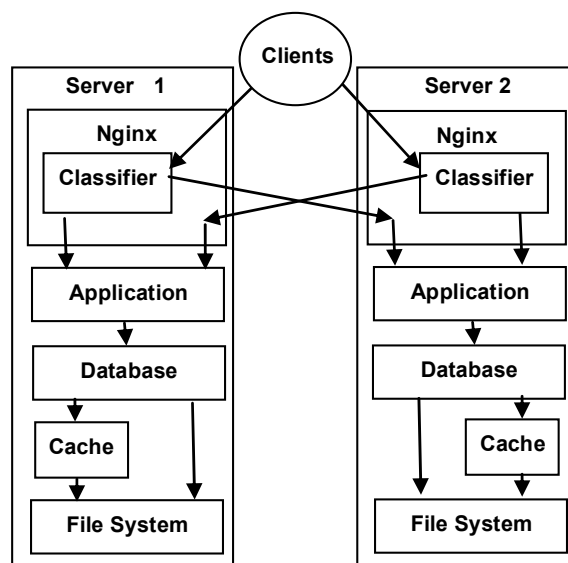*Ключевые слова: веб-приложения, надёжность, производительность, nginx*

UDC 537.635;537.611.44

O. Laguta, stud., Yu. Kobljanskyj, Ph.D.,
Taras Shevchenko National University of Kyiv

SURFACE MODES IN THIN FILMS OF PERMALLOY (NiFe)

Surface modes in spin wave resonance in as prepared thin films of $Ni_{80}Fe_{20}$ were studied. From 4 samples with 25, 50 75 and 100 nm of thickness only two (50 and 75 nm) have one surface mode. Using the surface inhomogeneity (SI) model with antisymmetric boundary conditions, the surface anisotropy constant K_s and variation of magnetization near the surface on the film $\partial_n M_s$ were determined. Also the critical angles θ_H^{cr} between the external magnetic field and the normal to the film's surface were defined. At this critical angle the surface mode coincide with the mode of uniform precession.

Key words: spin-wave resonance, Permalloy, thin film, surface mode, surface anisotropy

Introduction. Improving the technology of thin magnetic films allows their use in spintronic devices and microwave technology. Therefore there is an interest in their studies. As a powerful technique, the low energy excitations of spin waves and ferromagnetic resonance (FMR) play an important role in the study of thin films. Microwave technique can be used to investigate magnetic anisotropy, interlayer coupling, magnetic relaxation, film quality, and so on [3]. The spin wave resonance technique is the only way to study the surface modes. This sort of excitation is due to the surface anisotropy energy being different from the bulk value. The contribution of the surface energy is significant in thin films. Possibility of surface mode excitations are controlled by the state of the surface and close-to-surface inhomogeneities of the magnetization. Therefore the information about magnetic properties of the surface is available from the spin wave resonance experiment.

Experimental results and discussion. The samples were prepared by Electron Beam Evaporation (EBE) and have 75 and 50 nm of thickness. Measurements were carried out at room temperature using a Bruker E580 EPR spectrometer, with a fixed microwave frequency of 9.45 GHz. The goniometer was used to vary the angle. Samples were placed into the cylindrical mode resonator.

Figure 1 shows the sample oriented relative to some right-handed *X-Y-Z* frame such that the sample normal is parallel to the *Z* axis. External magnetic field H_{ext} and magnetization M lies in ZY plane. θ_H is the angle between H_{ext} and the sample normal Z, θ is an angle between M and Z.
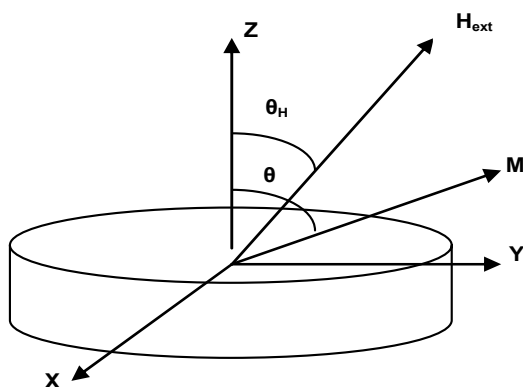
Fig. 1. Disk, field, and static magnetization geometry for the static equilibrium and FMR analysis

The spectra obtained for different angles θ_H presented in Fig. 2 and Fig. 3.

At the critical angle all modes except one vanish. We observe it as a transition of the surface mode into an uniform mode at the $\theta_H = \theta_H^{cr}$. At $\theta_H = 0°$ the distance between the surface mode H_s and the uniform one H_u is maximum and with increasing of θ_H this distance decreases (Fig. 4). As we can see, H_s decreases faster than H_u.
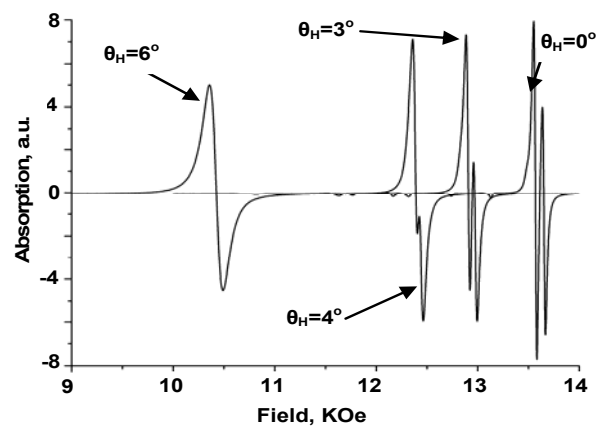
Fig. 2. Spin wave resonance spectra for different orientations of the applied magnetic field for 75 nm film
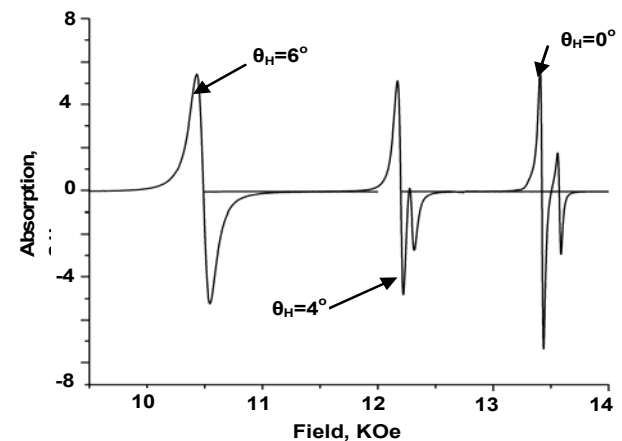
Fig. 3. Spin wave resonance spectra for different orientations of the applied magnetic field for 50 nm film

To use the SI model, we should decide which boundary conditions must be used first. This information could be extracted from perpendicular ($\theta_H = 0°$) magnetization data. The surface mode exists in two cases [1,8]: symmetric (if anisotropy is easy-plane, $K_s < 0$) and anti-symmetric boundary conditions. For symmetric boundary conditions the spin pinning parameter is the same at each film's surface ($\xi_1 = \xi_2 < 0$). For the case $\xi_1 = -\xi_2$, one surface has easy axis anisotropy, and the second one – easy-plane.
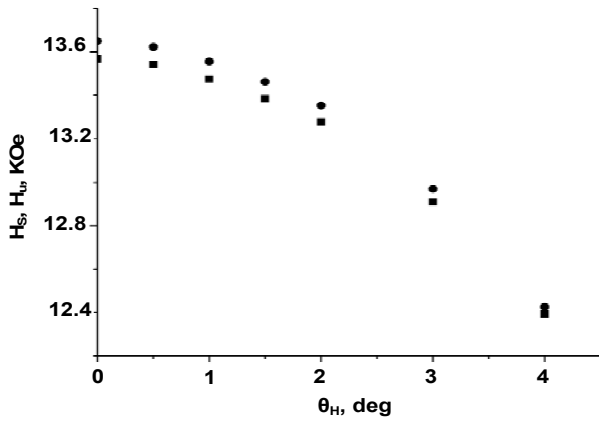
Fig. 4. Angular dependence of resonances fields H_S and H_u for 75 nm film. H_u are circles and H_S – squares

The resonance condition for normal magnetization is given by [1]:

$$H = \frac{\omega}{\gamma} + 4\pi M_S - \frac{2A}{M_S} k_z^2 \qquad (1)$$

$$ctg k_z d = \frac{k_z^2 - \xi_1 \xi_2}{k_z(\xi_1 + \xi_2)} \qquad (2)$$

1. $\xi_1 = \xi_2 < 0$. Solving numerical the equation (2) we can get $k_n = \frac{\pi n}{L}$, L - the film's thickness and $k = ik_s$. Real wave number give ordinary standing volume spin waves, and imaginary k – surface mode. From experimental data of surface mode's position H_s and Eq. (1) we can calculate k_s, using (2) – spin pinning parameter ξ and then the position of the next resonance line H_U. For the 75 nm film we get $k_s \approx 2.3 \times 10^5 \text{cm}^{-1}$, $|\xi| \approx 2.9 \times 10^5 \text{cm}^{-1}$, $H_U = 12,7$ KOe.

2. $\xi_1 = -\xi_2$. There are also real $k_n = \frac{\pi n}{L}$ and imaginary $k = i\xi$. Similarly we get $k = |\xi| \approx 2.3 \times 10^5 \text{cm}^{-1}$ and $H_U = 13.5$ KOe.

Fig. 5 represents the comparison of calculated H_U with experiment for 75 nm film. Namely, for anti-symmetric conditions calculated value of H_U agrees well with the experiment, while for symmetric conditions this value is less on 500 Oe. The same procedure was applied to 50 nm film and similar results were obtained. Now it's clear that both samples have anti-symmetric boundary conditions.
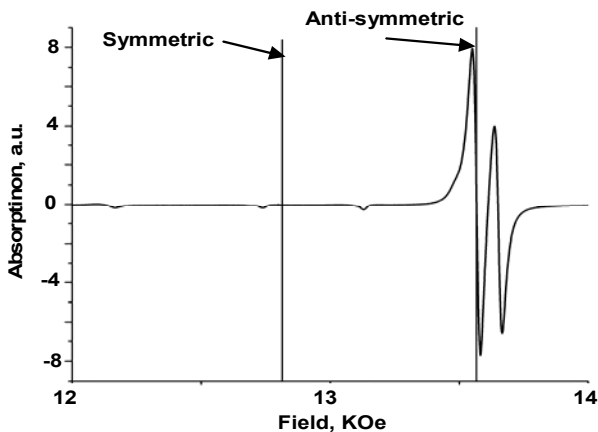
Fig. 5. Comparison of calculated H_u with experiment for 75 nm film

The SI model [4] was used to fit the experimental data. In this model boundary conditions include surface anisotropy energy and magnetization inhomogeneities close to the surface [7]. A simple form of the surface anisotropy $E_S \approx -K_S \cos^2(\theta)$ is taken, where K_S is the surface anisotropy constant. Using the equation of motion of magnetization the dispersion relation is written follow [5]:

$$\left(\frac{\omega}{\gamma}\right)^2 = \left[H\cos(\theta - \theta_H) + 4\pi M_{eff}\cos(2\theta) + \frac{2A}{M_S}k^2 \right] \times$$
$$\times \left[H\cos(\theta - \theta_H) + 4\pi M_{eff}\cos^2(\theta) + \frac{2A}{M_S}k^2 \right] \qquad (3)$$

$4\pi M_{eff} = 4\pi M_S - \frac{2K}{M_S}$. And the equilibrium condition is

$$2H_{res}\sin(\theta - \theta_H) = 4\pi M_S \sin(2\theta) \qquad (4)$$

The case $k^2 < 0$ provides purely imaginary $k = ik_s$, which describes damping of the microwave component of **M** with decreasing distance from the surface, so this case corresponds to the surface modes. The resonance field H_S for the surface mode is larger than field H_u for an uniform. Since the shift $H_S - H_U$ is small, we can get from (3) in the first approximation [2]:

$$H_S = H_U + \frac{2A}{M_S}\frac{k_s^2}{\cos(\theta - \theta_H)} \qquad (5)$$

According to [6, 7] the boundary conditions lead to the equation for the allowed wave vectors k_s:

$$\tanh(k_s L) = \frac{(p_1 + p_2)k_s}{k_s^2 + p_1 p_2} \qquad (6)$$

$$p = -(K_S/A)\cos(2\theta) + (\partial_n M_S)/M_S \qquad (7)$$

where p_1 and p_2 are values of p at the two surfaces of a film. As we already discussed our samples have anti-symmetric pinning parameters, $p_1 = -p_2$. ∂_n denotes the directional derivative along normal to the surface, so the term $(\partial_n M_S)/M_S$ accounts for possible variation of the magnetization close to the surface.

Equation (6) for allowed wave numbers is to be solved numerically. However, for typical parameters one can evaluate that $k_s L \gg 1$ unless we are very close to the critical angle and two approximate solutions are:

$$k_1 = p_1, k_2 = p_2. \qquad (8)$$

Therefore we expect two surface modes if $|p_1| \neq |p_2|$. For anti-symmetric boundary conditions $p_1 = -p_2$ only one surface mode is seen.

With the approximate solution (8) we can rewrite (5) in the form:

$$\sqrt{(H_s - H_u)\cos(\theta - \theta_H)} = \left(\frac{2}{AM_S}\right)^{1/2} |K_S| \times$$
$$\times \left[\cos 2\theta - \frac{A}{K_S}\frac{\partial_n M_S}{M_S} \right] \qquad (9)$$

where the exchange constant $A = 10^{-6} \text{erg/cm}$.

Table **1**

Summary information

L, nm	θ_H^{cr} SI model	θ_H^{cr} experiment	K_S, erg/cm² SI model	K_S, erg/cm² SI model	$\partial_n M_S$ Oe/nm
75	6°	5°	0,18	0,32	15
50	6,7°	5°	0,19	0,31	10

Now we can plot the left hand side of equation (9) (defined as X) against $\cos(2\theta)$. If model is correct we expect a straight line, with deviations perhaps in the very vicinity of the critical angle. We can get the surface anisotropy $|K_s|$ from the slope of this line and the interception with the x-axis gives the magnetization variation $(\partial_n M_s)/M_s$.

Fig. 6 represents the comparison of the SI model with experimental data. It is seen that we have straight line within the experimental error which confirms the proposed model. The fitted values of surface anisotropy constant K_s are reasonable, and are collected in Table 1. We want to mention that the critical angles determined from the extrapolation of the straight lines agree well with the same angles observed directly in the experiment.
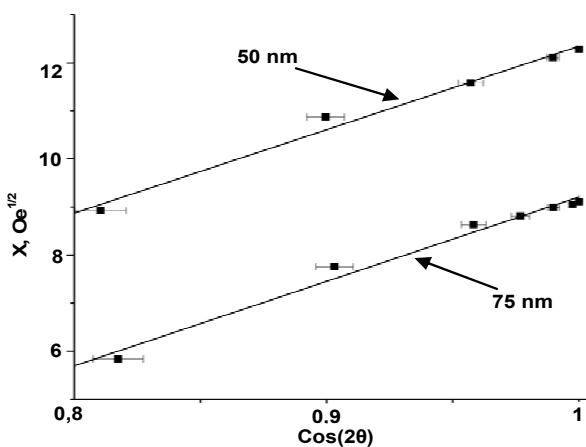

Fig. 6. Dependence of X against cos (2θ)

Conclusions. Angular dependence of surface modes in Permalloy thin films was studied. The surface anisotropy constant K_s and magnetization variation $(\partial_n M_s)/M_s$ were determined using the SI model. The values of K_s are in a good agreement with ones from the standing spin wave resonance experiments. Also this model provides the information about critical angles of surface modes' existence, which are in the agreement with experimental results. The SI model works well unless we are very close to the critical angle. So, the difference between fitted and experimental θ_H^{cr} may be caused by limitations of the surface inhomogeneities model.

Reference
1. Gurevich, A.G. Magnetization Oscillations and Waves / A.G.Gurevich, G.A.Melkov. – CRC Press, N.Y., 1996. – 445 p. – ISBN 0849394600. 2. Maksymowicz, L. J. Surface modes in magnetic thin amorphous films of GdCoMo alloys / L.J. Maksymowicz, D. Sendorek // JMMM. – 1983. – Vol. 37, Issue 2. – P. 177–188. – ISSN: 0304–8853. 3. McMichael, R.D. Ferromagnetic resonance studies of NiO-coupled thin films of Ni80Fe20 / R.D. McMichael, M.D. Stiles, P.J. Chen, W.F. Egelhoff, Jr. // Phys. Rev. B. – 1998. – Vol. 58. – P.8605. – ISSN 1098–0121. 4. Puszkarski H. Theory of surface states in spin wave resonance / H. Puszkarski // Progr. Surf. Scien. – 1979. – Vol. 9. – P. 191. – ISSN 0079–6816. 5. Puszkarski, H. On the interpretation of the angular dependence of the main FMR/SWR line in ferromagnetic thin films / H. Puszkarski, M. Kasperski // Acta Phys. Pol. A. – 2012. – Vol. 121. – P. 1165. – ISSN 1898–794X. 6. Spalek, J. Surface boundary conditions and angular dependence of the spin-wave resonance spectra / J. Spalek, A.Z. Maksymowicz // Solid State Commun. – 1974. – Vol. 15. – P. 559. – ISSN 0038–1098. 7. Sparks M. Ferromagnetic resonance in thin films. III. Theory of mode intensities / M. Sparks // Phys. Rev. B. – 1970. – Vol. 1. – P. 869. – ISSN 1098–0121. 8. Саланский Н. М., Єрухимов М. Ш. Физические свойства и применение магнитных пленок. // Новосибирск: Наука, 1975.– 224 с.

Лагута О., студ., Коблянський Ю., канд. фіз.-мат. наук,
Київський національний університет імені Тараса Шевченка

ПОВЕРХНЕВІ МОДИ В ТОНКИХ ПЛІВКАХ ПЕРМАЛОЮ (NiFe)

Досліджено поверхневі моди в тонких плівках Ni₈₀Fe₂₀ методом спін-хвильового резонансу. Із 4 зразків товщиною 25, 50, 75 та 100 нм лише два (50 та 75 нм) мають по одній поверхневій моді. Використовуючи модель неоднорідності поверхні з антисиметричними граничними умовами, було визначено константу поверхневої анізотропії K_s і варіацію намагніченності $\partial_n M_s$ поблизу поверхні плівки. Також були визначені критичні кути θ_H^{cr} між зовнішнім магнітним полем та нормаллю до поверхні плівки. При досягнені критичного кута поверхнева мода зливається із модою однорідної прецесії.
Ключові слова: спін-хвильовий резонанс, пермалой, тонкі плівки, поверхнева мода, поверхнева анізотропія

Лагута О., студ., Коблянский Ю., канд. физ.-мат. наук,
Киевский нацыональный университет имени Тараса Шевченко

ПОВЕРХНОСТНЫЕ МОДЫ В ТОНКИХ ПЛЕНКАХ ПЕРМАЛЛОЯ (NiFe)

Исследованы поверхностные моды в тонких пленках пермаллоя Ni₈₀Fe₂₀ методом спин-волнового резонанса. Из четырех образцов толщиной 25, 50, 75 и 100 нм два (50нм и 75 нм) имеют по одной поверхностной моде. Используя модель неоднородности поверхности с антисимметричными граничными условиями, определили постоянную поверхностной анизотропии K_s и вариацию намагниченности $\partial_n M_s$ вблизи поверхности пленки. Также были определены критические углы θ_H^{cr} между между внешним магнитным полем и нормалью к поверхности пленки. При достижении критического угла поверхностная мода сливается с модой однородной прецессии.
Ключевые слова: спин-волновой резонанс, пермаллой, тонкие пленки, поверхностная мода, поверхностная анизотропия.

V. Malyshev, As. Prof., G. Melkov, Dr.Sci., Prof., O. Prokopenko, Ph.D., Asc. Prof.
Department of Nanophysics and Nanoelectronics, Faculty of Radiophysics,
Taras Shevchenko National University of Kyiv

X-BAND TUNABLE MICROWAVE FILTER BASED ON SURFACE
ELECTROMAGNETIC WAVE RESONATOR AND YTTRIUM IRON GARNET FILM

Microwave properties of X-band microwave filter based on the surface electromagnetic wave resonator and yttrium iron garnet (YIG) film are investigated theoretically and experimentally. It is shown that the filter can be easily tuned by an external bias dc magnetic field, and by analyzing the system's behavior in the magnetic field one can determine an effective anisotropy field of the YIG film. Obtained results might be important for the development of magnetically-tuned microwave devices and also for the characterization of magnetic films.
Key words: microwave filter, surface electromagnetic wave resonator, yttrium iron garnet film, magnetic field, coupled oscillations.

Introduction. The surface electromagnetic wave resonator (SEWR) [5–8, 10, 12–16] utilizes the surface electromagnetic waves (SEW), well-known in microwaves, optics and quasi-optics [1, 9]. Microwave properties of bare SEWRs and resonators on different dielectric substrates are studied thoroughly during last 15 years (for instance, see Refs. in [5, 10]). Such interest to the SEWRs is caused by the following important key-features of the resonator [5–8, 10, 12–18]:

(a) It consists of only one conducting (or superconducting) film, instead of microstrip systems, that should have at least two conducting electrodes for proper operation;

(b) In accordance to (a), the fabrication technique of the SEWR is quite easy, at least easier than for microstrip systems;

(c) Fundamental mode of the SEWR can be easily excited by TE_{10} mode of a rectangular waveguide and the efficiency of the resonator can be easily tuned by changing an angle between the SEWR's plane and a wide wall of the waveguide;

(d) Electromagnetic oscillations corresponding to the stationary SEWs are characterized by large amplitude of microwave currents, excited in the conducting film, due to the high concentration of SEWs' electromagnetic field near a surface of the film.

In accordance to (a)–(d) SEWRs could be considered as promising base elements for different waveguide-type microwave devices. It seems that one of the most important applications of the SEWRs is an active microwave device based on nonlinear nano-elements, for instance, Josephson junctions [5, 10, 12–15, 18]. Such systems can be used for the creation of microwave signal sources [5], microwave detectors [5, 10, 12, 15], voltage standards and other metrological applications [5, 18].

However, in typical experimental situation SEWR can not be used for the creation of wide-band microwave devices, because its unloaded Q-factor is quite large (~10^3 for metallic resonators), while the mechanical changing of an angle between the resonator's plane and wide wall of a waveguide is a low-efficient technique that is inconvenient in practical application. In order to realize the non-mechanical tuning of the resonator's frequency, we attach an yttrium iron garnet (YIG) film to the resonator and tune the obtained system by an appropriate change of an applied external dc magnetic field.

In this work we show that the SEWR with attached YIG film operates as a tunable by a dc magnetic field microwave filter. We develop an analytical theory of such filter and compare theoretical results with the data of microwave measurements that allow us to determine an effective anisotropy field of the YIG film. We believe that the obtained results are important for the development of magnetically-tuned waveguide-type microwave devices and also could be used for the characterization of magnetic films.

Experiment. The schematic of used experimental setup is shown in Fig. 1. It consists of a microwave source connected via a microwave transmission line to the standard 3-cm waveguide section 4, where the filter is situated, and the indicator of a scalar network analyzer, which is used to determine the reflection coefficient $|S_{11}|$ of considered filter (see Fig. 1).
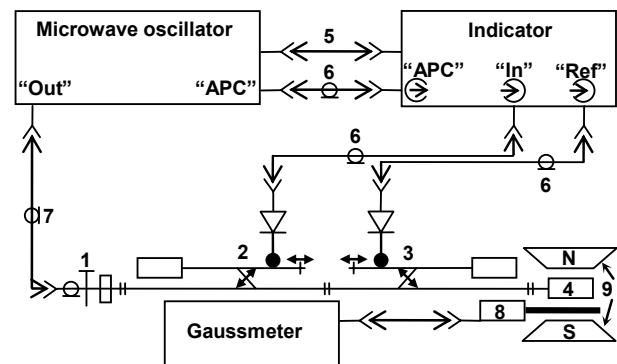
Fig. 1. Schematic of used experimental setup:
1 – waveguide-to-coaxial connector, 2 – directional coupler
of the incident wave, 3 – directional coupler of the reflected wave,
4 – the SEWR in the waveguide section, 5 – interconnecting cable,
6 – connecting coaxial cable, 7 – RF connecting cable,
8 – magnetic field sensor based on Hall effect, 9 – electromagnet

To analyze the signals reflected from the resonator we used standard technique based on measurement of the standing wave ratio of the standing wave in the waveguide section 4 using directional couplers 2, 3 (see Fig. 1) [3, 11, 19]. Waveguide section was made from the material that is transparent for an external bias dc magnetic field. The magnetic field was created by a controllable electromagnet 9 and measured by the sensor 8 based on Hall effect (see Fig. 1).

The considered filter consists of the half-wavelength aluminum SEWR (resonator's length is 10.8 mm, its width is 5 mm and its thickness is 15 mkm) on the dielectric substrate (its lateral sizes are the same as for the SEWR and its thickness is 0.5 mm) and YIG film of lateral sizes of 10.0×5.0 mm^2 and thickness 30 μm on a gallium gadolinium garnet substrate of thickness 0.5 mm. The layout of the filter is shown in Fig. 2. The distance between the aluminum resonator and the YIG film was equal to a sum of the both substrates' thicknesses.

The filter was situated inside the waveguide section as it is shown in Fig. 2. Angle between the resonator's plane and a wide wall of the waveguide, α, was chosen to be approximately 30 degree that corresponds to the optimum excitation conditions of the resonator.

External bias dc magnetic field was in-plane and directed along the length of the resonator; the magnitude of the field was controlled by an electromagnet and measured by a Hall-effect magnetic field sensor. At every value of the applied field we measured the amplitude-frequency curve of the filter in the frequency range 8.15 GHz – 12.05 GHz.

The frequency measurement error was about 50 MHz, while the field measurement error was 10 Oe.

X-band rectangular waveguide section

Al₂O₃ dielectric substrate

SEWR

YIG film
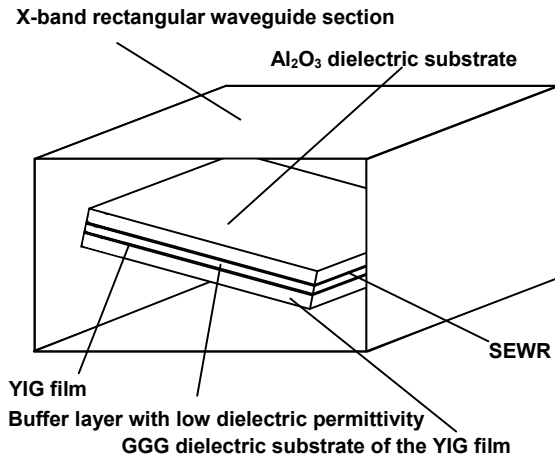**Buffer layer with low dielectric permittivity**
GGG dielectric substrate of the YIG film

Fig. 2. The layout of the considered filter in the X-band rectangular waveguide section

Theory. Taking into account the complexity of the full electromagnetic problem for considered filter in the waveguide section, we develop an approximate analytic theory based on the method of coupled oscillations [2]. Although this approach is not rigorous, it will give satisfactory results, precise enough to compare results of the theory and the experiment.

Maxwell equations for the SEWR excited by the magnetization **m** have the form [2, 4]

$$\text{rot}\,\mathbf{e} + \mathrm{i}k\mathbf{h} = -\mathrm{i}4\pi k\mathbf{m}, \quad \text{rot}\,\mathbf{h} - \mathrm{i}k\varepsilon\mathbf{e} = 0, \quad (1)$$

where $\mathrm{i} = \sqrt{-1}$, **e** and **h** are the complex amplitudes of electromagnetic fields, ε is the dielectric permittivity of the resonator's substrate, $k = \omega/c$, $\omega = 2\pi f$, f is the frequency of the fundamental mode of the SEWR, and c is the speed of light.

From the other hand, magnetization of the YIG film is excited by an electromagnetic field of the SEWR. In that case the linearized equation of motion of magnetization can be written as [4]:

$$\mathrm{i}\omega\mathbf{m} + \omega_H\left[\mathbf{m} \times \mathbf{z}_0\right] = -\gamma M_0\left[\mathbf{z}_0 \times \mathbf{h}\right], \quad (2)$$

where $\mathbf{H}_0 = \mathbf{z}_0 H_0$ is the external bias dc magnetic field, $\mathbf{z}_0$ is the unit vector directed along the external field (it is parallel to the surface of the resonator), $\mathbf{M}_0 = \mathbf{z}_0 M_0$, M_0 is the saturation magnetization of YIG film, $\omega_H = \gamma H_0$, $\gamma \approx 2\pi \cdot 28$ GHz/T is the modulus of the gyromagnetic ratio.

We present the microwave magnetic field of the fundamental mode of the resonator as

$$\mathbf{h} = \mathbf{h}_r + \text{grad}\,\phi, \quad (3)$$

where $\mathbf{h}_r$ satisfies the condition $\text{div}\,\mathbf{h}_r = 0$ and ϕ is the magnetostatic potential [4].

Eigen fields of the SEWR $\mathbf{e}_\nu$ and $\mathbf{h}_\nu$ can be determined from the equations

$$\text{rot}\,\mathbf{e}_\nu + \mathrm{i}k_\nu\mathbf{h}_\nu = 0, \quad \text{rot}\,\mathbf{h}_\nu - \mathrm{i}k_\nu\varepsilon\mathbf{e}_\nu = 0. \quad (4)$$

They also determined by the orthogonality conditions

$$\int_W \mathbf{h}_\eta^*\mathbf{h}_\eta dW = D_\nu\Delta_{\nu,\eta}, \quad \int_W \mathbf{e}_\nu^*\varepsilon\,\text{grad}\,\phi dW = 0, \quad (5)$$

where W is the volume, where the fields are not negligible, $\Delta_{\nu,\eta}$ is the Kroneker's symbol.

Eigen functions of the YIG film, $\mathbf{m}_n$ and ϕ_n, must satisfy the equations [4]

$$\mathrm{i}\omega_n\mathbf{m}_n + \omega_H\left[\mathbf{m}_n \times \mathbf{z}_0\right] + \gamma M_0\left[\mathbf{z}_0 \times \text{grad}\,\phi_n\right] = 0 \quad (6)$$

and

$$\int_V \left[\mathbf{m}_n \times \mathbf{m}_l^*\right]dV = \mathrm{i}\mathbf{z}_0 N_n\Delta_{n,l}, \quad (7)$$

where V is the film volume.

Using the equations for eigen functions (4), (6) and taking into account the orthogonality conditions (5), (7), one can obtain from (1), (2), the equations for coupled oscillations:

$$\left(\omega - \omega_\eta\right)a_\eta D_\eta + \omega\sum_n b_n\int_V \mathbf{h}_\eta^*\left(4\pi\mathbf{m}_n + \text{grad}\,\phi_n\right)dV = 0,$$

$$\left(\omega - \omega_l\right)N_l b_l + \gamma M_0\sum_\nu a_\nu\int_V \mathbf{h}_\nu\mathbf{m}_l^*dV = 0. \quad (8)$$

In the simplest case, when there are only two modes, the one is the fundamental mode of the SEWR (of the frequency ω_r) and other is the fundamental mode of the YIG film (of the frequency ω_f), we can obtain from (8) the characteristic equation

$$\left(\omega - \omega_r\right)\left(\omega - \omega_f\right)D_1 N_1 - \omega\gamma M_0 I_1 I_2 = 0. \quad (9)$$

Here $I_1 = \int_V \mathbf{h}_1^*\left(4\pi\mathbf{m}_1 + \text{grad}\,\phi_1\right)dV$, $I_2 = \int_V \mathbf{h}_1\mathbf{m}_1^*dV$. This means that the frequencies of coupled oscillations $\omega_{1,2}$ are given by the expression:

$$\omega_{1,2} = \frac{\omega_r + \omega_f + K}{2} \pm \frac{1}{2}\sqrt{\left(\omega_r - \omega_f\right)^2 + 2K\left(\omega_r + \omega_f\right) + K^2}, \quad (10)$$

where $K = \dfrac{\gamma M_0 I_1 I_2}{D_1 N_1}$ is the coupling coefficient.
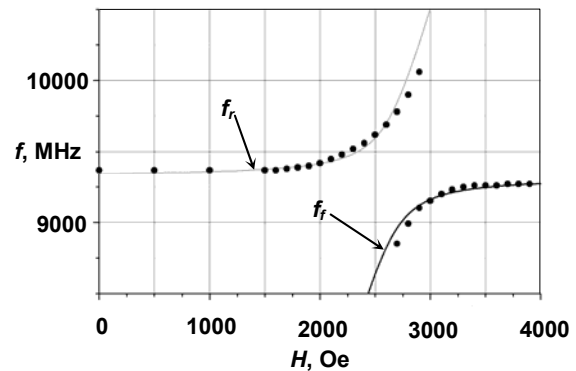
Fig. 3. Dependence of the resonance frequencies of the filter f on an external bias dc magnetic field H: lines are calculated using Eq. (10), while points are the measurement results

Results and discussion. The dependence of the response frequencies of the filter on a bias dc magnetic field is shown in Fig. 3 (lines are the theory results, while points are measurement's data). As one can see the resonance frequency of the SEWR (curve f_r in Fig. 3) practically does not depend on the magnetic field magnitude, when the field is weak enough. However, this dependence is crucial when the frequencies $f_r = \omega_r / 2\pi$ and $f_f = \omega_f(H_0) / 2\pi$ are equal and the coupling coefficient K from (10) is maximal. That condition gives a value of the resonance bias dc magnetic field (in our case this field is about 2750 Oe).

Comparing the frequencies calculated using (10) with the measurement points, we found that the optimal fit of the theoretical and experimental results can be obtained when using dc magnetic field $H_0' = H_0 + \Delta H$ in (11). Here H_0 is the real dc magnetic field applied to the YIG film and ΔH

could be the effective anisotropy field of the film. In our case ΔH was small enough, $\Delta H = -67$ Oe. However, we believe that such approach to determine ΔH can be successfully applied for the characterization of magnetic films with high anisotropy fields.

Conclusion. We have demonstrated that the SEWR and attached YIG film operates as a microwave filter, which can be tuned by applying a bias dc magnetic field to the system. Comparing theoretically predicted results and measurements data one can estimate an effective field of the film anisotropy. These results might be important for the development of magnetically-tuned waveguide-type microwave devices.

Reference
1. *Агранович В.М.* Поверхностные поляритоны // Успехи физических наук. – 1975. – Т.115. 2. *Вайнштейн Л.А.* Электромагнитные волны. – М., 1988. 3. *Гинзтон Э.Л.* Измерения на сантиметровых волнах. – М., 1972. 4. *Гуревич А.Г., Мелков Г.А.* Магнитные колебания и волны. – М., 1994. 5. *Іванюта О.М.* Лінійний ланцюжок джозефсонівських контактів у резонаторі поверхневої хвилі / дис. канд. фіз.-мат. наук / 01.04.03 – радіофізика. – К., 2003. 6. *Мелков Г.А., Єгоров Ю.В., Іванюта О.М., Малишев В.Ю.* Мікрохвильові резонатори на поверхневій хвилі // Вісник Київського університету. Серія: фізико-математичні науки. – 1998. – №3. 7. *Мелков Г.А., Єгоров Ю.В., Іванюта О.М., Малишев В.Ю.* Чвертьхвильові резонатори на поверхневій хвилі // Вісник Київського університету. Серія: фізико-математичні науки. – 1999. – №2. 8. *Мелков Г.А., Прокопенко А.В., Ракша В.Н.* Разрежение спектра собственных колебаний резонатора поверхностной волны // Известия ВУЗов "Радиоэлектроника". – Т.47, № 1. 9. Поверхностные поляритоны. Электромагнитные волны на поверхностях и границах раздела сред / Под ред. Г.А. Ремез. – М., 1985. 10. *Прокопенко О.В.* Резонатори поверхневої хвилі та надвисокочастотні пристрої на їх основі / дис. канд. фіз.-мат. наук / 01.04.03 – радіофізика. – К., 2005. 11. Техника измерений на сантиметровых волнах / пер. с англ.; под ред. Г.А. Ремез. – М., 1949. 12. *Ivanyuta O.M., Prokopenko O.V., Raksha V.M., Klushin A.M.* Microwave detection using Josephson junction arrays integrated in a resonator // Physica Status Solidi. – 2005. – Vol. 2, № 5. 13. *Ivanyuta O.M., Prokopenko O.V., Kishenko Ya.I., Raksha V.M., Klushin A.M.* The Effect of the External Magnetic Field on the Current-Voltage Characteristic of HTS Josephson Junction Arrays // Journal of Low Temperature Physics. – 2005. – Vol. 139, № 1/2. 14. *Ivanyuta O.M., Kishenko Ya.I., Prokopenko O.V., Raksha V.M.* The Josephson Junction Excitation System in a Surface Wave Resonator // Ukrainian Journal of Physics. – 2002. – Vol. 47, № 6. 15. *Klushin A.M., Ivanyuta A.N., Melkov G.A., Numssen Kai , Sigel M.* Irradiation of Multi-Junction Josephson Arrays Incorporated in SWR // PHYSICA C. – 2002. – 372–376. 16. *Melkov G.A., Egorov Y.V., Ivanyuta A.N., Malyshev V.Y., Zeng H.K., Wu K.H., Juang J.Y.* HTS Surface Wave Resonators // Journal of Superconductivity. – 2000. – Vol. 13, № 1. 17. *Melkov G.A., Egorov Yu.V.* Swihart waves and surface plasmons in a parallel-plate superconducting transmission line // Journal of Low Temperature Physics. – 2000. – Vol. 26, №2. 18. *Melkov G.A., Ivanyuta A.N., Klushin A.M., Goldobin E., Eghorov Y.V., Numssen K., Siegel. M.* .Frequency Locking of Josephson Junctions in Surface Wave Resonator.// IEEE TRANSACTIONS ON APPLIED SUPERCONCTIVITY. – 2001. – Vol. 11, №1. 19. The RF and microwave handbook / Ed. by M. Golio. Boca Raton, 2001.

В. Малишев, асп., Г. Мелков, д-р фіз.-мат. наук, проф.,
О. Прокопенко, канд. фіз.-мат. наук, доц.
Кафедра нанофізики та наноелектроніки, радіофізичний факультет
Київський національний університет імені Тараса Шевченка

ПЕРЕБУДОВУЄМИЙ НВЧ ФІЛЬТР 3-СМ ДІАПАЗОНА НА ОСНОВІ РЕЗОНАТОРА ПОВЕРХНЕВОЇ ЕЛЕКТРОМАГНІТНОЇ ХВИЛІ ТА ПЛІВКИ ЗАЛІЗО-ІТРІЄВОГО ГРАНАТУ

Теоретично та експериментально досліджено мікрохвильові властивості НВЧ фільтра 3-см діапазону на основі резонатора поверхневої електромагнітної хвилі та плівки залізо-ітрієвого гранату (ЗІГ). Показано, що такий фільтр легко перебудовується по частоті зовнішнім постійним магнітним полем, і досліджуючи поведінку системи в магнітному полі, можна визначити ефективне поле анізотропії плівки ЗІГ. Отримані результати можуть бути корисними при розробці магнітокерованих пристроїв НВЧ та при вивченні властивостей магнітних плівок.
Ключові слова: НВЧ фільтр, резонатор поверхневої електромагнітної хвилі, плівка залізо-ітрієвого гранату, магнітне поле, зв'язані коливання.

В. Малышев, асп., Г. Мелков, д-р физ.-мат. наук, проф., А. Прокопенко, канд. физ.-мат. наук, доц.
Кафедра нанофизики и наноэлектроники, радиофизический факультет
Киевский национальный университет имени Тараса Шевченка

ПЕРЕСТРАИВАЕМЫЙ СВЧ ФИЛЬТР 3-СМ ДИАПАЗОНА НА ОСНОВЕ РЕЗОНАТОРА ПОВЕРХНОСТНОЙ ЭЛЕКТРОМАГНИТНОЙ ВОЛНЫ И ПЛЁНКИ ЖЕЛЕЗО-ИТТРИЕВОГО ГРАНАТА

Теоретически и экспериментально исследованы микроволновые свойства СВЧ фильтра 3-см диапазона на основе резонатора поверхностной электромагнитной волны и пленки железо-иттриевого граната (ЖИГ). Показано, что такой фильтр легко перестраивается по частоте внешним постоянным магнитным полем, и исследуя поведение системы в магнитном поле, можно определить эффективное поле анизотропии пленки ЖИГ. Полученные результаты могут быть полезными при разработке магнитоуправляемых устройств СВЧ и при изучении свойств магнитных пленок.
Ключевые слова: СВЧ фильтр, резонатор поверхностной электромагнитной волны, пленка железо - иттриевого граната, магнитное поле, связанные колебания.

E. Martysh, D. Sc., Prof.
Taras Shevchenko National University of Kyiv,
V. Yatsenko, D. Sc., Prof.
Space Research Institute of NASU-NSAU

SPACECRAFTS AUTOMATIC DOCKING SYSTEM WITH ACTIVE INFRARED MARKERS

Servicing satellites on-orbit requires ability to rendezvous and dock by an unmanned spacecraft with no or minimum human input. Future space exploration missions will rely upon "smart" autonomous systems that require highly sophisticated vision systems. Emergence of novel computer vision algorithms and active markers will lead to a new generation of rendezvous and docking systems in the near future. Such systems will be capable of autonomously detecting a target satellite at a begining of the last rendezvous phases, estimating its bearing, range and relative orientation under any illumination, and in any satellite pose.
Keywords: satellite rendezvous and docking, marker-based vision, active markers

Introduction. The major space-faring nations are currently developing prospective manned transportation systems of the new generation. They include: advanced manned and cargo transport spacecrafts, inter-orbital transfer facilities, manned missions to the Moon and Mars, Lunar and Martian orbital complexes, landing on the surface of the planets and returning to the Earth. These facilities have diverse operating conditions, tasks specifics and dataware peculiarities at various flight stages. Traffic control and navigation system of the facilities under

development is one of the most complex airborne systems in terms of volume, tasks diversity, dataware and apparatus implementation. One of the traffic control and navigation system objectives is the navigation support task at all flight phases, which includes: convergence and docking with the orbital complex (or inter-orbital tug), convergence and docking with the Lunar or Martian craft.

For orbital operations variety performed during the orbital maintenance, spacecrafts (SC) automatic convergence and docking implementation will be necessary. During the convergence analysis it is usually considered that one of the spacecrafts is moving along the known orbit and it isn't maneuvering. This passive spacecraft is called the target (TSC). Mostly, it is the International Space Station (ISS), in case of the near-earth orbits. Maneuvering spacecraft, which mostly performs the docking part, is the active one (ASC). In general, the docking of these two spacecraft consists of the following stages: remote guidance, close guidance, final approach and docking.

Automatic guidance system uses certain previously chosen guidance method according to measurable movement parameters and produces control signals realized by the control-oriented system and active spacecraft engines. At the final approach stage TSC should be considered as a solid complex with a specific configuration and orientation, and not as a material point. In this case, granting the small movement parameters quantities, the question of special automatic measuring devices and guidance methods which take into account the TSC orientation and optimize the final approach trajectory development arises.

Docking system. "Igla" – the guidance system for the manned spacecraft "Soyuz" convergence and docking has been developed in the Soviet Union. The first prototypes of the system have been made in 1965. The first automatic convergence and docking of the "Soyuz" unmanned spacecraft took place on October 30, 1967. Guidance and convergence has been carried out in a range of 20–30 km, with the method of parallel guidance. The "Igla-1" (active one) used three sets of antennas: overview (second SC search), the gyro-stabilized (for the passive part respond auto-tracking "Igla-2") and a set of approach antennas. In 1976, the "Igla" system has been upgraded and used after that until 1985.

In 1979 the second generation of movement parameters mutual measurements system "Kurs" development has been initiated. Its main features were the presence of the reserve system build-in test control system, androgyny (distance and speed measurement on both SC), large ranges of the measured parameters, high measurement accuracy, the fly-by necessary information issuance. All of that has determined the high equipment reliability, its good adaptation to the satellite control systems of various types, including orbital stations with complex configuration. Since 1985, "Kurs" equipment delivery has begun for all SC from RSC "Energia", SSSPC named after M.V. Khrunichev. In 1986 the first "Soyuz TM-2" docking using "Kurs" equipment took place, and this equipment has been used since then [1].

On the basis of the "Kurs" equipment the work for the independent monitoring system of the ATV (European Space Agency) AC convergence with the ISS process has been carried out since 2000. The information processing using special computer of their own design is provided in this apparatus. The "Jules Verne" has been the first European automatic cargo SC, designed for the purpose,. The successful docking took place on April 3, 2008. The new generation high precision navigation system set which has been designed for managing trajectory and docking process with the ISS using optical sensors and the GPS technologies has been installed on the spacecraft [4].

The GPS system has been used so that the ship from a distance of 30 km could get closer to the ISS on the distance of 249 m, and then use the laser navigation system, which is based on the retroreflectors, located on front of the Russian module. At the same time the laser beams reflected from the retroreflectors are generated by the laser system located on the ship. Analysis of the reflection pattern has allowed to calculate the spacecraft relative position and orientation, and then "Jules Verne" has been able to approach and dock with the module. The cargo AC docking with the Russian ISS module simulation is shown in Fig. 1. The ship is equipped with two such devices. One of them is reserved.

Fig. 1. Simulation of "Jules Verne" docking with the Russian module of the ISS

The apparatus complex "Kurs-NA" development works are carried out since 2003. It is intended to replace the active part of the "Kurs" equipment on future SCs [2]. The main feature of the new equipment is almost complete analog signal processing abandonment with all the functions performed by microprocessors and the introduction of a new antenna into the equipment, which literally is antenna array with phase control. The new antenna will serve as a highly directional antenna with a gyro-stabilized platform, which is the part of the "Kurs" equipment. Recent modification consumes less power and has only one antenna (and not 5 as in the preceding). It should be noted that its orbit tests on the transport SC "Progress M-15" in July 2012 have not been entirely successful – the system has not coped with the docking program at the first attempt.

It may be mentioned that all the system modifications have been developed by the Moscow Scientific and Technical Complex "Precision instrumentation technology" (up to 2010 – SRI-TP) and have been manufactured (except for the "Kurs- NA") at the Kyiv Radio Factory.

Docking with the radar has its drawbacks. First of all, it can be inconvenient for an astronaut to maneuver on the spacecraft by viewing only the radar imagery, unlike video or images direct viewing. Radar measurements of range to the other satellites, the relative velocity and direction of convergence may not be sufficiently accurate. Moreover, as a rule, system of radar images has insufficient information on relative or angular orientation.

Alternatively, the docking operation performed by an astronaut on one of the SC can be performed by an operator on Earth. Unfortunately, the video information transmission delay to the Earth regarding distance, speed and direction, and then the command and control information transmission from the operator on Earth to the SC makes such procedure quite difficult.

Any type of control loop will have a negative impact on such delay. Of course, there are several opportunities for direct communication between the spacecraft and earth-based operators. There will be additional delays in the transmission to the satellite due to the absence of direct communication of operators on Earth with spacecraft. Naturally, these additional transmission delays will make the situation even worse.

We have already proposed the above system modernization using time-of-flight laser range finder. By reducing the duration of the laser pulse to hundreds picoseconds, the measurement accuracy of up to few centimeters can be achieved. However, this accuracy may be insufficient in the latter stages of final approach and docking. A joint analysis of the existing and future docking systems for the chosen method of obtaining the information allows general requirements formulation for individual nodes and devices in the optical system. Primarily, it concerns the optical radiation source characteristics, the optical scheme, the measurements data processing, storage and readout system.

At the intermediate docking phases mathematical movement models and pre-orientation devices based on satellite systems such as GLONASS, GPS or GALILEO can be used, which are good pre-orientation instruments required for the ASC entry into the nearest TSC region and the beginning of the docking process last phase. Certainly, the signals receiver from all three systems simultaneously is the best option for such a device.

The need for back-up systems such as an independent infrared range finder on the picosecond laser for the penultimate docking phase can be determined by the analysis of the promising developments. This device is necessary not only for measuring the relative distance in real time, but also for speeding up the mathematical processing when generating the commands for the control equipment (engine brakes and boosters). However, the laser interferometer (LI) [3], installed on the ISS can provide stable information on the relative distance with precision to the tenth of centimeter, which in its turn gives better opportunities during the docking last phase.

Interesting coherent technique, mentioned above (LI), is the so-called self-mixing or optical feedback interferometry that relies on the coherent optical echo signal backscattered by the remote target that reenters the cavity of a laser diode (LD), thus generating a useful interferometric signal. The advantages of the self-mixing approach are its low cost and compactness and the very simple self-aligning optical setup that does not require a reference path. Several distance measurement approaches have been proposed based on fringe counting in the self-mixing configuration, achieving a resolution of a few millimeters. In this paper we only present a new approach to absolute distance measurement based on the self-mixing effect, which makes use of an electronic feedback loop to achieve a resolution that is limited by the detection shot noise and not by the discretization error that is associated with the conventional fringe-counting technique. The feedback loop generates a square-wave modulation of the LD wavelength that exactly corresponds to a 2π variation in the interferometric phase; that is, the number of wavelengths that is contained in the path from the LD to the target and back again is varied by unity. Then, the target distance can be easily derived from the knowledge of the applied wavelength modulation. The performance of the prototype instrument that has been developed features a 0.2 – to 3-m measuring range, with a resolution of 0.3 mm.

However, the basis of the proposed docking system is active optical markers (AOM) to track spacecrafts motion, so their angular orientation, with the glow of the most tokens. Active systems over passive, have greater accuracy and the ability to cover more working area. Additionally, light sources (e.g. laser diodes) may be pulsed, which enables to capture a significant amount of markers which are closest to each other. That they can simultaneously use temporary and polarization separation of markers imaging for further processing.

The requirements in rendezvous and docking problems lead to control problems with imposed pointwise-in-time and terminal constraints on both state and control variables. For instance, the approaching spacecraft must maintain its position within a Line-of-Sight cone from the docking port on the target platform. In addition, terminal velocity of the spacecraft should match the velocity of the docking port to ensure soft-docking. Since the platform has convex shape, by remaining within a Line-of-Sight cone and by matching the velocity of the port, the spacecraft is guaranteed not to collide with the platform, and the spacecraft fuel consumption must be minimized during the maneuvers. The above requirements and constraints can be systematically treated using a Model Predictive Control framework and active optical markers.

The feasibility of optical movement interferometric sensor with millimeter sensitivity use is shown. The proposed method of small spacecraft movements evaluation enables its use in docking system at the adequate marker parameters. The solid-state laser treated by ionized radiation functioning analysis and its response to the space weather factors have been conducted. The forecasting systematic combination and risk minimization feasibility considering the space weather has been shown.

The possibilities of using optical image recognition methods in spacecrafts docking system analysis has been conducted. This review contains a comparison of modern classification and recognition methods. The following methods are reviewed: a) spacecraft optical imaging and markers consistent recognition based on dynamic programming; b) recognition method using a decision-making functions; c) optical image recognition using statistical methods; d) optical image recognition based on the most informative features and dynamic approach. It is shown that due to information increase, there is a recognition algorithm learning possibility.

Conclusions. The dynamic programming approach towards marker patterns has been proved to be useful in sequential video system designing, the optimal structure of which can be considered as a multistage decision making process. It is shown that the actual decision making structure with the sequential marker patterns recognition, which includes both the choice of continuing and the choice of stopping the observations sequence is obtained by recursive risk functions optimization. The resulting sequential classifier requires, on average, a smaller number of feature measurements (and therefore is less expensive when measurements cost is involved). Since the classifier observes one measurement at a time and never requests more than a predetermined number that would have to be used in an equally reliable nonsequential classifier for a single decision.

It is possible to provide docking system on the basis of AOM, which is based on automatic objects finding and recognition with the definition of their angular direction on real time scale. The proposed system also provides resistance to brightness change and geometry of the observed objects and their location. The undoubted advantages of this system include: high probability of finding and recognizing TSC (as a target), small mass characteristics and operation on real time scale. Finally, the possibility of constructing the AOM-based panoramic optoelectronic system without scanning should be mentioned.

Reference
1. *Fehse W.* Automated Rendezvous and Docking of Spacecraft // Cambridge University Press. – 2003. 2. Manned space flights // CSRIeng - Bulletin of the news and analysis – 2013, № 19. 3. *Norgia M., Giuliani G., Donati S.* Absolute Distance Measurement With Improved Accuracy Using Laser Diode Self-Mixing Interferometry in a Closed Loop // IEEE Transactions of Instr. & Measurement. – 2007, Vol. 56. 4. *Zimpfer D., Kachmar P., Tuohy S.* Autonomous rendezvous, capture and in-space assembly: Past, present, and future // 1st Space Exploration Conference: Continuing the Voyage of Discovery, Jan. – 2005.

Є. Мартиш, д-р фіз.-мат. наук, Київський національний університет імені Тараса Шевченка
В. Яценко, д-р техніч. наук, Інститут космічних досліджень НАН та НКА України

СИСТЕМИ З АКТИВНИМИ ІЧ-МАРКЕРАМИ
ДЛЯ АВТОМАТИЧНОГО СТИКУВАННЯ КОСМІЧНИХ АПАРАТІВ

Для обслуговування супутників на орбіті вимагається здатності до зближення і стикування з допомогою безпілотних космічних апаратів, з відсутністю або мінімальним втручанням людини. Майбутні експедиції з дослідження космосу будуть покладатися на "інтелектуальні" автономні устройства, для яких потрібні дуже складні системи технічного зору. Поява нових алгоритмів комп'ютерного зору і активних маркерів призведе до нового покоління систем зближення і стикування в найближчому майбутньому. Такі системи будуть здатні автономно виявляти цільовий супутник на старті останніх етапів зближення, оцінювати його пеленг, віддаль та відносну орієнтацію при будь-якому освітленні і в будь-якому його положенні.
Ключові слова: зближення і стикування, маркерний технічний зір, активні маркери.

Е. Мартиш, д-р физ.-мат. наук, Киевский национальный университет имени Тараса Шевченко
В. Яценко, д-р технич. наук, Институт космических исследований НАН и НКА Украины

СИСТЕМЫ С АКТИВНЫМИ ИК-МАРКЕРАМИ
ДЛЯ АВТОМАТИЧЕСКОЙ СТЫКОВКИ КОСМИЧЕСКИХ АППАРАТОВ

Для обслуживания спутников на орбите требуется способности к сближению и стыковке с помощью беспилотных космических аппаратов, с отсутствием или минимальным вмешательством человека. Будущие экспедиции по исследованию космоса будут полагаться на "интеллектуальные" автономные устройства, для которых требуются очень сложные системы технического зрения. Появление новых алгоритмов компьютерного зрения и активных маркеров приведет к новому поколению систем сближения и стыковки в ближайшем будущем. Такие системы будут способны автономно обнаруживать целевой спутник на старте последних этапов сближения, оценивать его пеленг, удаление и относительную ориентацию при любом освещении и в любом его положении.
Ключевые слова: сближение и стыковка, маркерное техническое зрение, активные маркеры.

S. Pud, post grad. Stud., M. Petrychuk, PhD, V. Kovalenko, Dr.Sci., Prof.
Department Electrophysics, Faculty of Radiophysics,
Taras Shevchenko National University of Kyiv

INFLUENCE OF THE ELECTROLYTE ON TRANSPORT CHARACTERISTICS
OF ION-SENSITIVE SILICON NANOWIRE FIELD EFFECT TRANSISTORS

We report on the effect of the electrolyte on transport properties of open-gated silicon nanowire (NW) field effect transistor (FET) biosensor studied using noise spectroscopy. Exposing the Si NW FET to the electrolyte solution affects the threshold voltage, because it shifts the potential of the top dielectric layer. Also electrolyte ions screen the effect of the gate dielectric traps on channel transport. NWs of different lengths were used to exclude contact effects and show consistency of the measurement.
Key Words: silicon nanowires, open-gate, noise spectroscopy, electrolyte, biosensor.

Introduction. Silicon nanowire field effect transistors (Si NW FETs) are promising structures for the development of new biosensors due to their property of directly translating |interactions with target molecules into readable signals [6], [5]. These structures are highly sensitive and selective and are capable of real-time response and label-free detection. However, there are several important challenges, such as the stability and reproducibility of the operation of such sensors in a liquid environment due to the property changes of the thin gate dielectric when exposed to an electrolyte for a long time [4]. In this contribution, noise spectroscopy was employed to characterize the performance of the Si NW FET biosensors with the electrolyte solution (working as a top gate of the NW FET structure) on top and also without it. The influence of the electrolyte on transport was studied by changes of the device transport and noise characteristics. The results show that the electrolyte solution not only influences the threshold voltage of the transistor, but also affects the charge state of the surface traps.

Experimental Details. Transport and noise properties were measured and analyzed in Si NW FETs with a width of 500nm and a variety of lengths from 2 to 16µm (Fig. 1A). The nanowires were produced on the basis of silicon-on-insulator (SOI) wafers using nanoimprint technology with subsequent wet chemical etching of the NW structures. The contacts to the NWs were highly As implanted, so the NW represented a FET with inverted n-type channel. The

NW sensors were protected from the electrolyte by a thin thermally grown SiO_2 passivation layer (10nm thickness). The measurements were performed with phosphate-buffered saline (PBS) electrolyte on top of the passivation layer of the NW FET structure and without electrolyte (in air) at different back-gate voltages, V_G.
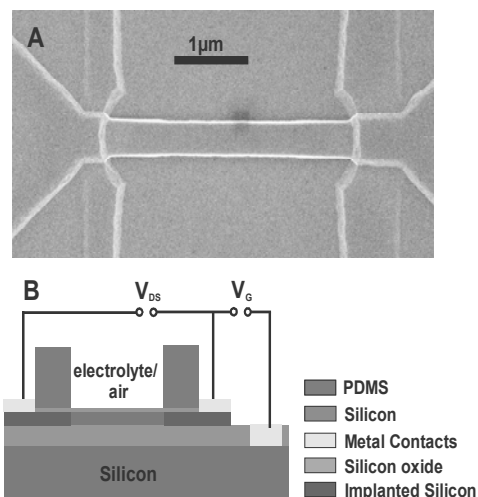

Fig. 1. (A) SEM image of a 500 nm wide silicon nanowire.
(B) Sketch of the measurementset-up

The back-gate voltage, V_G, was applied to the substrate of the silicon-on-insulator (SOI) wafer. The schematic of the experiment is shown in Fig. 1B. The potential of the drain, V_{DS}, as well as the back gate, V_G, was set against the grounded source. In all experiments shown here, V_{DS}, was set to a value of 100 mV to maintain a linear regime of operation of the NW transistor. In this regime, the differential resistance of the sample equals the normal value of resistance, which makes it much simpler to evaluate the normalized current noise spectral density (NCNSD), S_I/I^2, using the measured drain voltage noise spectral density.

It should be noted that the noise spectra and the I-V curves were measured in a constant DC mode. The drain voltage, V_{DS}, and back-gate voltage, V_G, were applied using a battery loaded with the sample and a load resistance.

Results and discussion. The transfer characteristics of the Si NW transistors were measured in DC mode in air and in electrolyte (Fig. 2).
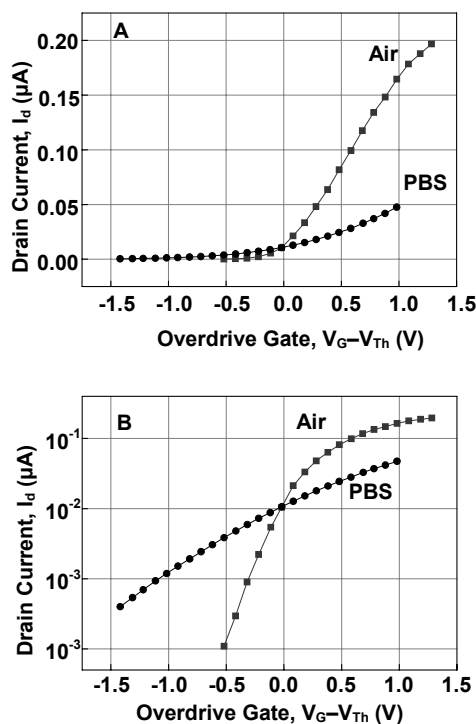

Fig. 2. Transfer curves of the 8μm Si NW FET measured in air (red curves) and in PBS (black curves) plotted on linear scale(A) and on logarithmic scale(B)

The measurement set-up was as described above. The drain current, Id, controlled by the back-gate voltage is higher in air than in the electrolyte in overthreshold mode, at $V_G>V_{Th}$ (Fig. 2A) and higher in electrolyte than in air in subthreshold mode, $V_G>V_{Th}$. It should be emphasized that each point of the transfer characteristics was measured at a stabilized drain current. After the back-gate voltage was applied, the drain current increased with time until it reached a certain saturation value. The time between applying the gate voltage and saturation of the drain current was around 20 min in the case of air and around one minute in the case of electrolyte. The leakage current through the back-gate electrode was negligibly small (below 0.1nA). Therefore we suggest that such an effect is related to charging of the traps located in the top dielectric layer through the back-gate electrode [2]. The time constant of such a process is so large because the traps are charged with extremely small currents through the back-gate dielectric. The decrease of the charging time in the electrolyte can be explained by the

effect of charge screening. In the presence of the electrolyte, the charge accumulated in the top passivation dielectric is immediately screened by the ions of the electrolyte solution. Therefore the conductivity of the channel changes much faster in the electrolyte, but the influence of the back gate on the channel through the charging of top dielectric layer decreases. The slope of the transfer curve is higher in air than in the PBS solution (Fig. 2A). And this difference can also be explained by charging the top dielectric layer through the back gate and the screening effect in the electrolyte. In the subthreshold region (Fig.2B), we can observe that the subthreshold current in the electrolyte is higher than in air.

As mentioned above, all measurements were performed at low drain voltages (100mV). In such a regime, the subthreshold current is not related to transport through surface states, but is mainly defined by diffusion [1]. The increase of the subthreshold current in PBS solution can again be explained by screening of the potential of the top dielectric layer by ions in the electrolyte. In the subthreshold mode, negative overdrive gate voltages are applied to the sample, and screening of the negative overdrive potentials by ions in the electrolyte means shifting the surface potential to zero, which, in turn, leads to an increasing drain current. The curves measured in air and in PBS solution coincide within the close vicinity of the zero overdrive gate voltage. This means that screening does not occur in this point and that the zero overdrive gate voltage is close to the flat-band point. Therefore we can conclude that introducing PBS on top of the NW transistor affects transport in the transistor through screening of the surface potential of the top dielectric layer [3].

Behavior similar to that described above is also registered in the samples with different channel lengths. The drain current with the same value of the overdrive gate voltage, $V_G–V_{Th}$, is plotted versus the channel length of the device in Fig.3.
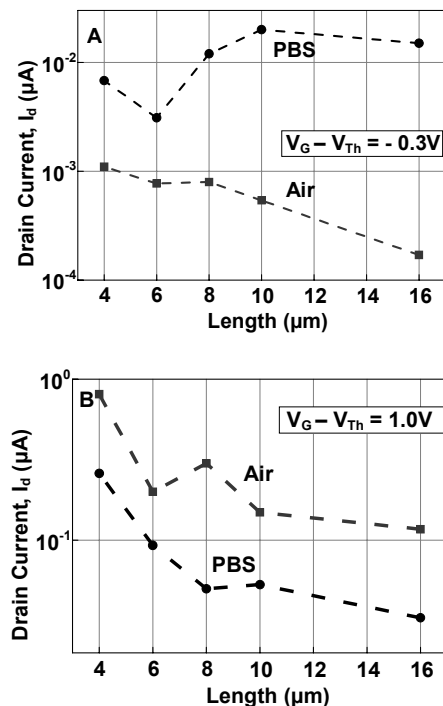

Fig. 3. Drain current through Si NW FETs measured in air (red curves) and in PBS (black curves) plotted versus chanel length at drain voltage of 100 mV in subthreshold mode (A) and in overthreshold mode(B)

The drain current is well scaled with the length of the sample (Fig. 3A in air and Fig. 3B). Contact resistance

can be estimated from the dependence of the drain current on length by linear approximation (Fig. 3A in Air). The value obtained is in the range between 8 and 12 kOhm for different measured chips, which is much lower than the device channel resistance, even when it is opened. Only Si NWs with shorter channels (4 and 6 μm) are affected by the contact resistance (Fig. 3A in Air). In the case of the PBS solution on the surface of the Si NW biosensor, the subthreshold current is higher than in air and vice versa – the overthreshold current in PBS is lower than in air. Subthreshold current in PBS (Fig. 3A) is no longer scaled with length. This may be due to the fact that the current in the subthreshold region is strongly affected by the electrolyte, which influences the surface potential of the gate dielectric.

The influence of PBS on transport in Si NW FET is also confirmed by noise measurements. Fig. 4 shows the normalized current noise spectral density (NCNSD), S_I/I^2, at subthreshold and overthreshold voltages measured in air and PBS. In the subthreshold region, NCNSD in the device decreased when PBS was introduced into the sample. This decrease can be partially explained by the changing of the subthreshold current. This current increased by a factor of 3 (Fig. 2b at an overdrive gate of -0.2V) after submerging a sample in PBS. Therefore, the NCNSD, S_I/I^2, has to decrease by approximately one order of magnitude, but from Fig. 4A we can see that the value of NCNSD is more than one order of magnitude lower in PBS compared to that as in air.
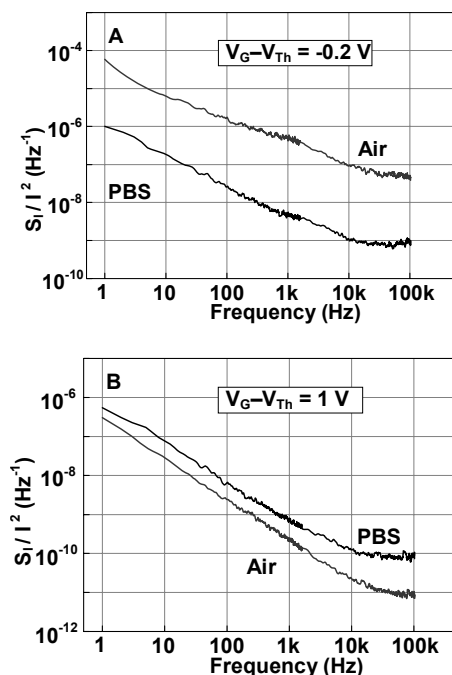

Fig. 4. Normalized current noise spectral density (NCNSD), S_I/I^2, at sub-threshold (A) and overthreshold (B) overdrive gate voltages measured in air (red curves) and PBS (black curves)

This is possible only if the exchange between the Si NW channel and the traps in the gate dielectric is affected. Thus, this decrease of NCNSD can be explained by the changing of the surface charge state in the sample's top dielectric due to PBS electrolyte adsorption and the screening effect as well as only a partial contribution of the increased subthreshold current. In the region above the threshold, submerging the sample in PBS results in a small increase in the amplitude of fluctuations in the sample. The lower value of the current at V_G-V_{Th} = 1.0 V in PBS only partially influences the normalized noise level behavior.

The difference in NCNSD cannot be explained only by the difference in current. In this case, the current in air is approximately 3.25 times higher than in PBS (Fig. 2A), which means that without any other factors NCNSD should be at least an order of magnitude lower in PBS. Our results show that exposing the nanowire samples to PBS in overthreshold mode decreases NCNSD only slightly. Therefore as in subthreshold mode, the overall excess noise in the Si NW channel is lower when we expose it to the electrolyte, in spite of the fact that the transconductance is lower in PBS than in air.

Conclusion. Transport properties of silicon nanowire field effect transistors exposed to air and to the electrolyte solution were investigated and compared utilizing noise spectroscopy. The results were obtained under quasistatic conditions in DC mode. It has been shown that the submerging of the nanowire samples in PBS affects the current in the NW channel by screening the charges, which accumulate in the top dielectric layer due to coupling between back and front gate. The investigated nanowire structures show good reproducibility in parameters. The devices of different lengths show similar behavior with the electrolyte and air on top. The produced Si NW FETS are well scaled with length and have contact resistance in the range of 10 kOhms, which is much lower than channel resistance. The noise measurements show that the electrolyte influences transport properties in the Si NW channel not only by screening surface potential, but it may also change the charge state of the traps in the top dielectric layer. As a result of such influence, the value of the excess noise is much lower in PBS than in air in the subthreshold region.

Reference
1. *Chang J., Abidi A.A., Viswanathan C.R.* Flicker noise in CMOS Transistors from Subthreshold to Strong Inversion at Various Temperatures // IEEE Trans. Electron Devices. – 1994. – N 11(41). – P. 1965–1971. 2. *Hyung-Kyu L., Fossum J.G.* Threshold Voltage of Thin-Film Silicon-on-Insulator (SOI) MOSFET's // IEEE Trans. Electron Devices. – 1983. – N ED-30(10). – P. 1244–1251. 3. *Nair P.R., Alam M.A.* Screening-limited response of nanobiosensors // Nanolett. – 2008. – N 8(5). – P. 1281–1285. 4. *Nair P.R., Alam M.A.* Design considerations of silicon nanowire biosensors // IEEE Trans. El. Dev, vol. 54, no. 12, pp. 3400–3408, 2007. 5. *Patolsky F., Zheng G., Lieber C.M.* Nanowire-based biosensors // Analytical Chemistry. – 2006. – N 78(13). – P. 4260–4269. 6. *Ramgir N.S., Yang Y., Zacharias M.* Nanowire-based sensors // Small. – 2010. – N 6(16). – P. 1705–1722.

С. Пуд , асп., М. Петричук, канд. фіз.-мат. наук,
В. Коваленко, д-р фіз.-мат. наук, проф.
кафедра електрофізики, радіофізичний факультет,
Київський національний університет імені Тараса Шевченка

ВПЛИВ ЕЛЕКТРОЛІТУ НА ЕЛЕКТРОФІЗИЧНІ ХАРАКТЕРИСТИКИ ІОННО-ЧУТЛИВИХ ПОЛЬОВИХ ТРАНЗИСТОРІВ НА БАЗІ КРЕМНІЄВИХ НАНОНИТОК

Досліджено вплив електроліту на електрофізичні властивості іонно-чутливих польових транзисторів на базі кремнієвих нанониток за допомогою шумової спектроскопії. Занурення польового транзистора на базі кремнієвих нанониток в розчин електроліту призводить до зсуву порогової напруги транзистора завдяки зміні потенціалу верхнього шару діелектрику. Також іони електроліту екранують вплив пасток верхнього шару діелектрику на транспорт в каналі транзистора. Для виключення контактних ефектів та підтвердження достовірності експерименту було проведено вимірювання транзисторів з різною довжиною каналу.

Ключові слова: кремнієві нанонитки, відкритий затвор, шумова спектроскопія, електроліт, біосенсор.

С. Пуд, асп., М. Петричук, канд. физ.-мат. наук,
В. Коваленко, д-р физ.-мат. наук, проф.
кафедра электрофизики, радиофизический факультет,
Киевский национальный университет имени Тараса Шевченко

ВЛИЯНИЕ ЭЛЕКТРОЛИТА НА ЭЛЕКТРОФИЗИЧЕСКИЕ ХАРАКТЕРИСТИКИ ИОННО-ЧУВСТВИТЕЛЬНЫХ ПОЛЕВЫХ ТРАНЗИСТОРОВ НА БАЗЕ КРЕМНИЕВЫХ НАНОНИТЕЙ

Исследовано влияние электролита на электрофизические свойства ионно-чувствительных полевых транзисторов на базе кремниевых нанонитей с помощью шумовой спектроскопии. Погружение полевого транзистора на базе кремниевых нанонитей в раствор электролита приводит к смещению порогового напряжения транзистора благодаря изменению потенциала верхнего слоя диэлектрика. Также ионы электролита экранируют влияние ловушек верхнего слоя диэлектрика на транспорт в канале транзистора. Для исключения контактных эффектов и подтверждения достоверности эксперимента были проведены измерения транзисторов с различной длиной канала.
Ключевые слова: кремниевые нанониты, открытый затвор, шумовая спектроскопия, электролит, биосенсор.

A. Skrypets, Ph.D., V. Tronko, Dr. Sci,
Avionics Department, Institute of Airnavigation, National Aviation University, Kyiv
M. Asanov, Ph.D., Energy Supply and Physics Department,
National Academy of Environmental Protection and Resort Development, Simferopol

REMOTE MEASUREMENT OF POLARIZED RADIATION PARAMETERS

In this work a method for measuring the polarized radiation parameters by determining its ellipticity angle and azimuth of polarization ellipse is describes. It is proposed to additionally mechanically modulate the polarization plane of the analyzed radiation, pre-calculating the modulation amplitude. This method allows measuring relative Stokes vector components of radiation with highly accuracy in the entire optical range.
Keywords: polarized radiation, Stokes vector components, remote measurement

Introduction. Polarization is a fundamental physical characteristic of the radiation, which is conditioned by electromagnetic nature of light. Its measurement, followed by a theoretical analysis is a powerful diagnostic tool. The polarization state of light carries information not just about the characteristics of separate particles but also about the surface of the objects. Polarization methods of analysis have been used particularly in medicine [1, 2, 5], during studying material surface [4], in aerospace remote sensing [3, 8]. Increasing the accuracy of determining the Stokes vector components of the polarized radiation is an important and urgent problem.

In [6] authors proposed a photopolarimetric method for determining the polarized radiation parameters. The basis of this method is the measurement of the ellipticity angle and the azimuth of the polarization ellipse of optical radiation by Stokes polarimeter with the modulation of the polarization plane of analyzed radiation by Faraday cell. The active element of a Faraday cell is transparent in the near-infrared range yttrium iron garnet. Additional modulation of the polarization plane of the radiation increased the accuracy of the ellipticity angle and the azimuth of the polarization ellipse measurement, and, consequently, the relative values of the Stokes vector components. However, using the yttrium iron garnet as an active element of Faraday cell limits the application of the proposed Stokes polarimeter by IR range. Additionally, the domain structure of yttrium iron garnet partially depolarizes passing light radiation that reduces the accuracy of the determination of the Stokes vector components.

In this work the Stokes polarimeter is described, in which instead of a magneto-optical Faraday cell is proposed to use a mechanical modulation of the polarization plane. This Stokes polarimeter will allow to provide studies of radiation in the entire optical range without significantly reducing the accuracy and sensitivity of measurements.

Description. Block diagram of proposed Stokes polarimeter is shown in Fig. 1. To determine the azimuth of the polarization ellipse λ and the ellipticity angle ω one needs to make two measurements.

While measuring the azimuth of the polarization ellipse λ the most transmission plane azimuths of analyzers *1* and *2* are set to $\beta - \theta$ and $\beta + \theta$ angles respectively (Fig. 1, a). The angle θ is pre-calculated so that the signal-to-noise ratio at the output of photodetector was maximal [7]. The switch *5* converts the voltage into an alternating electric signal by passing signals in turn from the two photodetectors *3* and *4*.
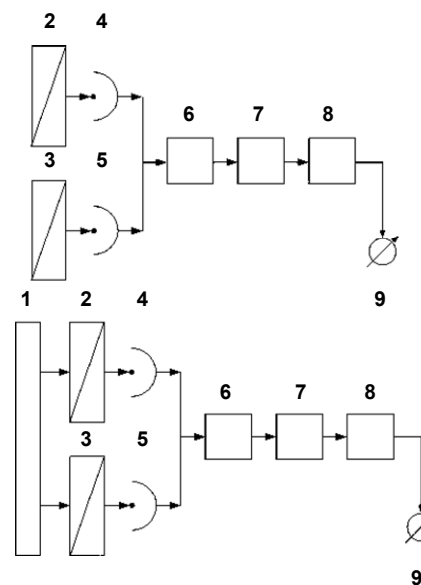

Fig. 1. Block diagram of Stokes polarimeter:
1 – λ/4 phase plate; 2, 3 – analyzers; 4, 5 – photodetectors;
6 – switch; 7 – amplifier; 8 – synchronous detector;
9 – ammeter (indicator)

Intensities of radiation at the output of the analyzers will be given by:

$$I_{OUT_2} = \frac{I}{2}(k_1 + k_2) \times \left[1 + (1 - 2Gd)\, p \cos 2\omega \cos 2(\lambda - \beta + \theta) \right];$$

$$I_{OUT_3} = \frac{I}{2}(k_1 + k_2) \times \left[1 + (1 - 2Gd)\, p \cos 2\omega \cos 2(\lambda - \beta - \theta) \right],$$

where I is the total intensity of the incident radiation; k_1, k_2 are the principle transmittances of polarizing prisms; Gd is polarization defect of prism, p is the polarization degree of the analyzed radiation.

By setting up the photopolarimeter to minimum signal at the photodetector output, measuring the most transmission plane azimuths of analyzers, one determines the parameter λ by the following equation:

$$\lambda = \frac{\pi}{2} + \beta_{min} + \Delta ,$$

where β_{min} is the most transmission plane azimuth of analyzer at which the intensity of radiation at its output is minimum; Δ is the measurement error.

To determine the ellipticity angle ω $\lambda/4$ phase plate is putted in front of the analyzers. Most speed plane azimuth of phase plate α is set in the direction of a large (or small) axis of the polarization ellipse of the light λ (Fig. 1, b). In this case, the equations for intensities of the radiation at the analyzers output will be as following:

$$I_{OUT_2} = \frac{I}{2}(k_1 + k_2) \times \left[1 + (1 - 2Gd) p \cos 2(\omega - \beta + \alpha + \theta) \right] ,$$

$$I_{OUT_3} = \frac{I}{2}(k_1 + k_2) \times \left[1 + (1 - 2Gd) p \cos 2(\omega - \beta + \alpha - \theta) \right] .$$

By setting up the photopolarimeter to minimum signal at the photodetector output, the angle of ellipticity ω is found from the following equation:

$$\omega = \frac{\pi}{2} + \beta_{min} - \alpha + \Delta .$$

The expressions for determining the Stokes vector components are following:

$$I = \frac{I_{OUT_{max}} + I_{OUT_{min}}}{k_1 + k_2} ;$$

$$M = p \cos 2\omega \cos 2\lambda = \frac{I_{OUT_{max}} - I_{OUT_{min}}}{\left(I_{OUT_{max}} + I_{OUT_{min}} \right)(1 - 2Gd)}$$

$$\times \cos 2\left(\frac{\pi}{2} + \beta_{min} + \Delta \right) ;$$

$$C = p \cos 2\omega \sin 2\lambda = \frac{I_{OUT_{max}} - I_{OUT_{min}}}{\left(I_{OUT_{max}} + I_{OUT_{min}} \right)(1 - 2Gd)}$$

$$\times \sin 2\left(\frac{\pi}{2} + \beta_{min} + \Delta \right) ;$$

$$S = p \sin 2\omega = \frac{I_{OUT_{max}} - I_{OUT_{min}}}{\left(I_{OUT_{max}} + I_{OUT_{min}} \right)(1 - 2Gd)}$$

$$\times tg 2\left(\frac{\pi}{2} + \beta_{min} - \alpha + \Delta \right) .$$

Conclusions. 1. Proposed Stokes polarimeter with a mechanical modulation will allow to provide high-precision measurement of polarized radiation parameters in the entire optical range.

2. It should be noted that the described Stokes polarimeter has two channels, which negatively affect the measurement accuracy due to the fact that it is difficult to achieve an absolute equivalence between the characteristics of two channels.

3. Furthermore, the performance of this Stokes polarimeter is low due to the mechanical type of modulation.

References
Гарасевич С.Г., Коренюк П.І., Мягченко Ю.О., та ін. Застосування оптимізованого класичного поляриметра для визначення вмісту оптично активних речовин в прозорих та темних розчинах // Вісник Київського університету, серія: фізико-математичні науки. – 1999. – № 1. – С. 311–321. 2. *Иванов А.П.* Поляризация света и ее использование в различных задачах оптики рассеивающих сред // Оптика и спектроскопия. – 2009. – Т. 107. – С. 183–195. 3. *Киселев Н.Н., Розенбуш В.К., Шаховской Н.М.* и др. Поляриметрические исследования комет в Крымской астрофизической обсерватории // Известия Крымской астрофизической обсерватории. – 2007. – Т. 103. – №. 4. – С. 216–230. 4. *Петров В.В., Крючин А.А., Савенков С.Н.* и др. Исследование поляриметрических характеристик оптических дисковых носителей // Реєстрація, зберігання і обробка даних. – 2009. – Т. 11. – №2. – С. 3–11. 5. *Рогаткин Д.А.* Об особенности в определении оптических свойств мутных биологических тканей и сред в расчетных задачах медицинской неинвазивной спектрофотометрии Медицинская техника. – 2007. – № 2. – С. 10–16. 6. *Скрипець А.В., Тронько В.Д., Асанов М.М.* Фотополяриметрический метод определения параметров поляризационного излучения // Вісник астрономічної школи. – 2011. – Т. 7. – № 2. – С. 155–160. 7. *Скрипець А.В., Тронько В.Д., Асанов М.М.* Двухлучевой фотополяриметр измерения угла поворота плоскости поляризации в мутных средах // Електроніка та системи управління. – 2010. – № 1 (23). – С. 26–30. 8. Polarimetric remote sensing of Solar System objects / [*Mishchenko M.I., Rosenbush V.K,. Kiselev N.N,* etc.]. – K.: Akademperioodyka, 2010. – 291 р.

А. Скрипець, канд. техн. наук, В. Тронько, д-р фіз.-мат. наук,
кафедра авіоніки, Інститут аеронавігації, Національний авіаційний університет, Київ
М. Асанов, канд. фіз.-мат. наук, кафедра енергопостачання та фізики,
Національна академія природоохоронного та курортного будівництва, Сімферополь

ДИСТАНЦІЙНЕ ВИМІРЮВАННЯ ПАРАМЕТРІВ ПОЛЯРИЗОВАНОГО ВИПРОМІНЮВАННЯ

У даній роботі описаний метод вимірювання параметрів поляризованого випромінювання шляхом визначення кута еліптичності та азимуту еліпса поляризації цього випромінювання. При цьому пропонується додатково механічно модулювати площину поляризації аналізованого випромінювання, попередньо розраховуючи амплітуду модуляції. Цей метод дозволить з високою точністю вимірювати відносні компоненти вектора Стокса випромінювання у всьому оптичному діапазоні.
Ключові слова: поляризоване випромінювання, компоненті вектора Стокса, дистанційне вимірювання

А. Скрипец, канд. техн. наук, В. Тронько, д-р физ.-мат. наук,
кафедра авионики, Институт аэронавигации, Национальный авиационный университет, Киев
М. Асанов, канд. физ.-мат. наук, кафедра энергоснабжения и физики,
Национальная академия природоохранного и курортного строительства, Симферополь

ДИСТАНЦИОННОЕ ИЗМЕРЕНИЕ ПАРАМЕТРОВ ПОЛЯРИЗОВАННОГО ИЗЛУЧЕНИЯ

В данной работе описан метод измерения параметров поляризованного излучения путем определения угла эллиптичности и азимута эллипса поляризации этого излучения При этом предлагается дополнительно механически модулировать плоскость поляризации рассматриваемого излучения, предварительно рассчитывая амплитуду модуляции. Этот метод позволит с высокой точностью измерять относительные компоненты вектора Стокса излучения во всем оптическом диапазоне.
Ключевые слова: поляризованное излучение, компоненты вектора Стокса, дистанционное измерение

A. Shavrin, stud., Ju. Kiashko, stud., S. Levitsky, Dr.Sci., Prof.
National Taras Shevchenko University of Kyiv, Faculty of Radiophysics

SOME PECULIAR PROPERTIES OF OSCILLATORS WITH AUTOMATIC BIAS

Differential RC-cell (grid leak) is inserted to the circuit of the feedback of oscillators for automatic bias so additional phase rotation appears that causes some shift of the generated frequency in comparison with the resonance frequency of the oscillatory circuit.
If the feedback is strong enough, the automatically bias results also to the appearance of interrupted generation, where the periodicity of the pulses becomes irregular. This is caused by internal noises causing the moment and the magnitude of the appearance of the next pulse.
Key words: phase rotation, frequency shift, interrupted generation, irregular periodicity.

Introduction. The automatic bias (so called grid leak) is often applied in order to stabilize the operation of the auto-generators (oscillators). The grid leak is an RC-cell inserted into the circuit of the transistor base [3, 4].

The oscillations that are detected (rectified) by the diode being formed in the base circuit on the p-n junction existing between the base and the emitter of the transistor. In the base circuit a current I_D arises creating a voltage drop RI_D on the resistor R which counteracts with the voltage E_B, decrease the direct voltage on the base, lowers down the working point on the common emitter–base characteristic and locks the transistor. This effect becomes so stronger so stronger are the generated oscillations.

Thus owing to the automatically bias the self-excitation of the oscillator begins in a soft regime, but the following operation occurs in a more economical steady hard regime. But the existence of a differential RC-cell in the feedback chain must in any way affect on the process of the self-excitation and on the generated frequency.

As is well known, the generated frequency is determined by self-excitation phase condition $\psi_K + \psi_\beta = 2\pi$ where ψ_K is the phase rotation in the amplifier, and ψ_β – in the feedback loop.

In the oscillator, similar to shown in Fig.1, ψ_β is determined by the corresponding switching of the inductances L and L_{FB} so as to form $\psi_\beta = \pi$. And with the oscillator where the transistor is switched in the scheme with a common emitter, the condition $\psi_K = \pi$ is satisfied if the load in the collector circuit is purely active that is exactly at the resonant frequency of the oscillating circuit.
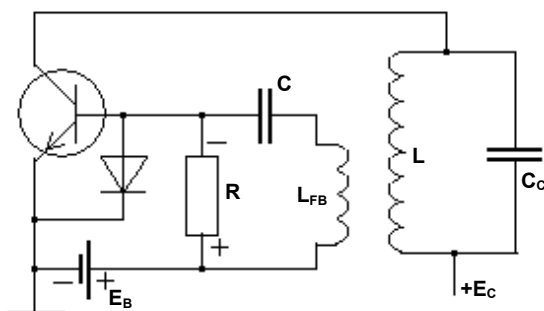

Fig. 1. Schematic diagram of the oscillator

The gridleak inserted into the input circuit of the transistor is a differential RC-cell that creates in the feedback loop a shifting of phase $\varphi(\omega) = \mathrm{arctg}(1/\omega\tau)$, where the $\tau = RC$ is the grid leak time constant, and ω - the generated frequency which is no longer exactly equal to the resonant frequency ω_0 of the oscillating circuit, and will be different from its as $\Delta\omega = \omega - \omega_0$

The phase shift delivered by the grid leak must be compensated by a phase shift in the oscillator circuit $\psi(\omega) = -\mathrm{arctg}(2Q\frac{\Delta\omega}{\omega_0})$, due to its detuning on the $\Delta\omega$. Therefore for the performance of the phase condition it may be [1, 7]

$$\mathrm{arctg}(\frac{1}{\omega_0\tau}) = \mathrm{arctg}(2Q\frac{\Delta\omega}{\omega_0}),$$

or

$$\frac{1}{\omega_0\tau} = 2Q\frac{\Delta\omega}{\omega_0},$$

hence

$$\Delta\omega = \frac{1}{2Q\tau}.$$

Further it must be verified, if it will be performed the amplitude condition of the self-excitation, because by the detuning of the oscillator circuit on $\Delta\omega$ the module of the its equivalent resistance decreases

$$| Z_{equ}(\Delta\omega) | = \frac{R_{equ}}{\sqrt{1 + (2Q\frac{\Delta\omega}{\omega_0})^2}} = \frac{R_{equ}}{\sqrt{1 + (\frac{1}{\omega_0\tau})^2}}$$

For instance, when $\omega_0 = 10^6 s^{-1}$, $Q = 30$, $C = 0.5 nF$, $R = 1 k\Omega$, the shift of the frequency is

$$\Delta\omega = \frac{1}{2Q\tau} = \frac{1}{2.30.5.10^{-10}.10^3} = 3,33.10^4 s^{-1}.$$

As for the amplitude condition,

$$| Z_{equ}(\Delta\omega) | = \frac{R_{equ}}{\sqrt{1 + (\frac{1}{\omega_0 RC})^2}} = \frac{R_{equ}}{\sqrt{1 + (\frac{1}{10^6.10^3.5.10^{-10}})^2}} \frac{R_{equ}}{\sqrt{5}},$$

and the supply for the self-excitation amplitude condition must be greater than in the absence grid leak of 2.23 times.

This in account of availability of the automatically bias in the autogenerator a negative feedback is formed and stabilizing the level of the generated oscillation.

Consequently, the surplus of the amplitude conditions of self-excitation must be greater than in the absence of the gridleak.

But due to the inertia of the oscillatory circuit, so as of the RC-cell, in the feedback circuit arises a additional phase shift, which can under certain conditions convert the negative feedback to the positive. Then in the scheme are beginning some oscillations of the level of the generated signal with a period commensurate to the inertia of the feedback circuit (selfmodulation). Herewith the capacitor C can be loaded so strong, that the transistor becomes completely closed. But even thereafter because to the large quality and inertia of the oscillatory circuit his oscillations continue to be supported and are further loading the capacitor of the grid leak. The transistor remains closed while the capacitor is discharged through the R-resistor during the time of the order of the RC-product. The generated oscillations becomes the sequence of periodical pulses. This phenomenon of interrupted generation is well known and described in the literature [2, 4].

But when modeling in Multisim software or when dealing with real oscillator layout similar to shown in Fig.1, we found that the time between pulses is not stable and may be subject to change disordered within about ten percent (Fig.2).

The spectrum of such oscillations (Fig.3) is indicating the chaotic nature of this process. From this figure we can determine the oscillation frequency of the pulses which is approximately in the vicinity of 370 kHz. This frequency corresponds just to the upper limit of the spectrum

On the Fig.2, one also can see well that the interval between pulses is that greater, than greater was the previous pulse.

To understand the reason for this is we could observing the course of the voltage on the transistor base (Fig.4). It is clearly seen that the transistor is opened and the next pulse is beginning at the same voltage about 0.7V. In the process of pulse generating the voltage on the base is reduced through the rectifying of the base-emitter diode, that charges the capacitance C in the greater extent, the larger was the previous pulse. And the longer is the process of discharge of the capacity to a level, at which the transistor is opened and can create the next pulse.

As for the size of most pulses, it is determined, perhaps, by the level of noise or interference, from which starts the self-excitation of the next pulse generated. The randomness of the noise and interferences causes the random nature of these processes, just as is the case in the absence of regular input signals in some superregenerators [2,5,6].
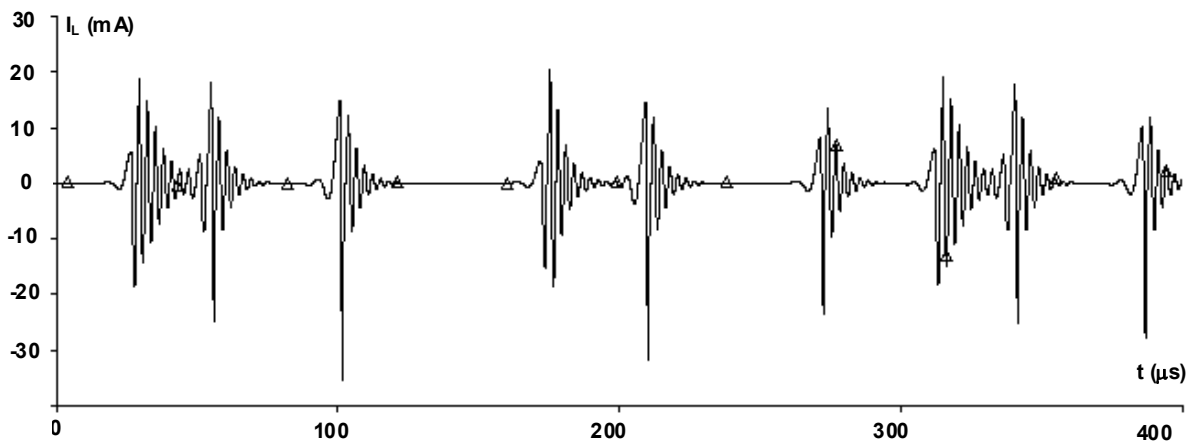

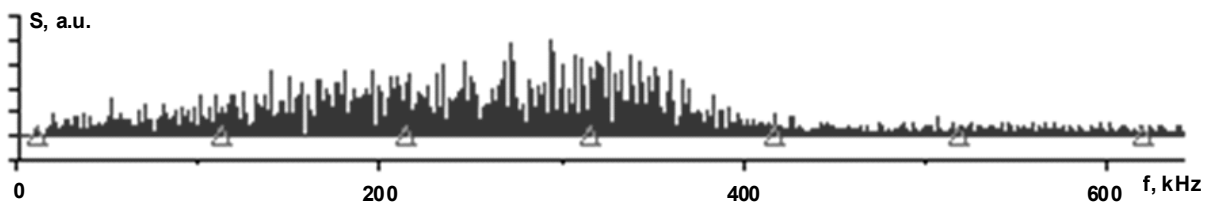Fig. 2. Waveform of the current through inductor L

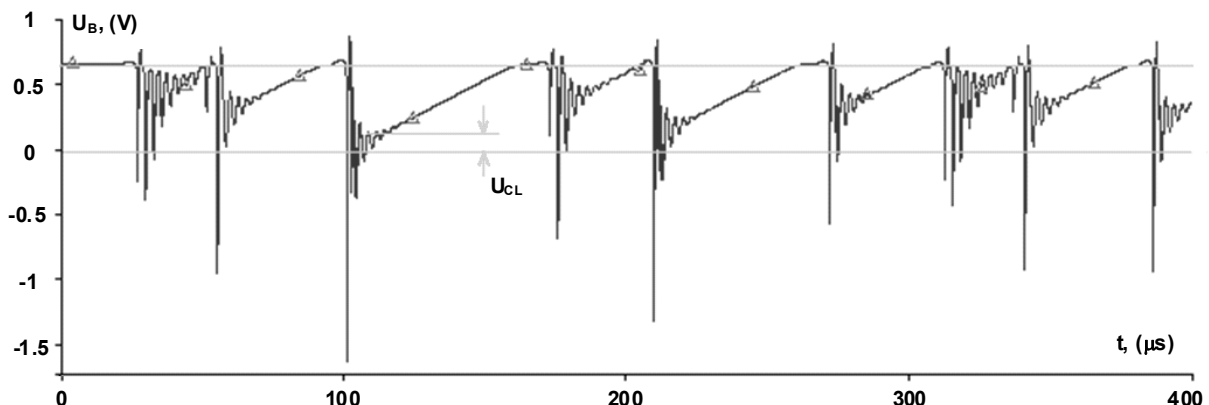Fig. 3.Spectrum of the current through inductor L

Fig. 4. Waveform of the transistor base voltage

Certain confirmation of these considerations was an experiment when we forcibly injected from an external source a slight signal in the circuit of the base with a frequency near to the frequency of oscillation of the circuit. When the amplitude of this external signal was large enough to exceed the potential of the noise and interference, the value of all the pulses and the intervals between them were identical.

In the process of pulse generating the voltage on the base is reduced through the rectifying of the base-emitter diode, that charges the capacitance C in the greater extent, the larger was the previous pulse. And the longer is the process of discharge of the capacity to a level, at which the transistor is opened and can create the next pulse.

As for the magnitude of most pulses, it is determined, perhaps, by the level of noise or interference, from which starts the self-excitation of the next pulse generated. The randomness of the noise and interferences causes the random nature of these processes, just as is the case in the absence of regular input signals in some superregenerators [5, 6].

Certain confirmation of these considerations was an experiment when we forcibly connected a slight signal from an external source to the circuit of the base with a frequency near to the frequency of oscillation of the circuit. When the amplitude of this external signal was large enough to exceed the potential of the noise and interference, the value of all the pulses and the intervals between them were identical.

Reference
1. *Bayrachenko I.V.* Radiotechnical circuits and signals / *Bayrachenko I.V.* – Kyiv: PPC "Kyiv University", 1992 (in Ukrainian). 2. *Belkin M.K.* Superregenerative radio receiving / *Belkin M.K.* – Kyiv: Technica, 1986 (in Russian). 3. *Levitsky S.M.* Fundamentals of Radio Electronics / *Levitsky S.M.* – Kyiv: PPC "Kyiv University", 2007 (in Ukrainian). 4. *Ozersky Yu.P.* Nonlinear transformations and radio signals' receiving / *Ozersky Yu.P.* – Moscow: MIPT, 2010 (in Russian). 5. *Polyakov V.* Superregenerator (part1) / *Polyakov V.* // Radio. – 2001. – No11. – P. 51–52 (in Russian). 6. *Polyakov V.* Superregenerator (part2) / *Polyakov V.* // Radio. – 2002. – No3. – P. 50–51 (in Russian). 7. *Samoylo K.A.* Radiotechnical circuits and signals / *Samoylo K.A.* – Moscow: Radio i svyaz', 1982 (in Russian).

А. Шаврін, студ., Ю. Кияшко, студ., С. Левитський, д-р фіз.-мат. наук, проф.
Київський національний університет імені Тараса Шевченка, радіофізичний факультет

ДЕЯКІ ВЛАСТИВОСТІ АВТОГЕНЕРАТОРІВ З АВТОМАТИЧНИМ ЗМІЩЕННЯМ

У автогенераторах RC-комірка автоматичного зміщення створює зсув фази коливань, що призводить до зсуву генерованої частоти.
У випадку переривистої генерації (при досить великій сталій часу RC-комірки) при відповідних параметрах RC-комірки та величині зворотного зв'язку періодичність імпульсів стає нерегулярною. Це спричиняється внутрішніми шумами які обумовлюють момент і величину виникнення чергового імпульсу генерації.
Ключові слова: обертання фази, зсув частоти, переривчаста генерація, нерегулярна періодичність.

А. Шаврин, студ., Ю. Кияшко,студ., С. Левитский, д-р физ.-мат. наук, проф.
Киевский национальний университет имени Тараса Шевченка, радиофизический факультет

НЕКОТОРЫЕ СВОЙСТВА АВТОГЕНЕРАТОРОВ С АВТОМАТИЧЕСКИМ СМЕЩЕНИЕМ

В автогенераторах RC-ячейка автоматического смещения создает сдвиг фазы колебаний, что приводит к смещению генерируемой частоты. В случае прерывистой генерации (при достаточно большой постоянной времени RC-ячейки) при соответствующих параметрах RC-ячейки и величине обратной связи периодичность импульсов становится нерегулярной. Это происходит засчет внутренних шумов, обуславливающих момент и величину возникновения очередного импульса генерации.
Ключевые слова: вращение фазы, сдвиг частоты, прерывистая генерация, нерегулярная периодичность

M. Shcherbinin, stud., I. Anisimov, Doct. Sci.,
Faculty of Radiophysics,
Taras Shevchenko National University of Kyiv

DYNAMICS OF ELECTRON BUNCH IN THE EXTERNAL MAGNETIC FIELD: COMPUTER SIMULATION

Influence of the longitudinal magnetic field on the electron bunch expansion in vacuum was studied. Analytic estimation of the spatial dependence of the bunch radius is compared with the simulation results via PIC method. Results obtained from simulation correlate satisfactory with theoretical estimations for the large magnetic field and low bunch density. Dynamics of the relativistic bunches was also studied.
Keywords: electron bunch expansion, longitudinal magnetic field, simulation via PIC method.

Introduction Problem of dynamics of electron beams and bunches is important for a wide range of branches [2], including inertial thermonuclear fusion and creation of the high frequency vacuum tubes [3], various types of spectrometry, electronic and ionic mycroscopy. In most cases top forming, focusing the bunch, and preventing of it's swelling due to the space charge are the priority tasks [2]. One of the most common ways to prevent swelling is the longitudinal magnetic field imposing to the system. Other methods use the external electric field and the spatial charge of residual plasma (for electron beams). Analytic solution of problem of the dynamics of electron bunch is rough [1]. Therefore the aim of this work is to carry out the computer simulation of the dynamics of electron bunch in a vacuum system with the longitudinal magnetic field.

Analytic estimation The simplest model of the homogeneous cylindrical electron beam of infinite length is treated. From the Gauss theorem one can obtain the electric field on its boundary:

$$E_r = -2\pi R n e = -\frac{2Ne}{R}, \quad (1)$$

where R is the current cylinder radius, n and $N = \pi R^2 n$ are spatial and linear electron densities, respectively. Note that linear density N remains constant during the beam electrons' transversal oscillations. The motion equations for the electrons at the cylinder boundary have a form:

$$m\frac{dv_r}{dt} = -eE_r - \frac{e}{c}v_\varphi B; \quad m\frac{dv_\varphi}{dt} = \frac{e}{c}v_r B; \quad m\frac{dv_z}{dt} = 0, \quad (2)$$

where $\vec{B} = \vec{e}_z B$ is the external magnetic field.

From the last equation (2) it is clear that $v_z = const \equiv v_0$.

One can obtain the following equations for the transversal velocity components from (1)–(2):

$$\frac{d^2 v_r}{dt^2} + \Omega^2 v_r = 0; \quad \frac{d^2 v_\varphi}{dt^2} + \omega_c^2 v_\varphi = -\frac{\omega_c e}{m} E_r\left(R(t)\right), \quad (3)$$

Where $\omega_c = \dfrac{eB}{mc}$, $\omega_p^2 = \dfrac{4\pi n e^2}{m}$, $\Omega^2 = \omega_c^2 + \dfrac{\omega_p^2}{2}$

(note that $v_r = dR/dt$). Initial conditions have a form:

$$R(t=0) = R_0; \quad v_r(t=0) = v_\varphi(t=0) = 0. \quad (4)$$

For the strong magnetic field one can put

$$R = R_0 + \Delta r(t) \ (|\Delta r(t)| \ll R_0),$$

$$E_r(R(t)) \approx E_r(R_0) + (dE_r/dR)\big|_{R=R_0} \Delta r .$$

Then solution of the set (3) with the initial conditions (4) have a form:

$$v_\varphi(t) = \frac{\omega_p^2}{2\omega_c^2} R_0 (1 - \cos\Omega t), \quad v_r(t) = \frac{\omega_p^2}{2\omega_c^2} R_0 \sin\Omega t . \quad (5)$$

Consequently one can obtain the following formula for the beam radius oscillations' amplitude Δr_m:

$$\frac{\Delta r_m}{R_0} = \frac{\omega_p^2}{2\omega_c^2} . \quad (6)$$

Expression (6) is valid for $\omega_p^2 \ll \omega_c^2$.

Simulation results for different bunch densities The electromagnetic 2.5D code was used valid for simulation of axially symmetric systems [4]. The simulation results are the spatial distributions of the charge density, radial component of electrical and azimuthal component of magnetic field, which are recorded every $1 \cdot 10^{-10}$ s.

The first series of simulations was carried out for bunches with various electron density (Fig. 1). From Fig. 1 a one can get the frequency and the amplitude of the bunch oscillations: in particular, for the bunch's density of $5 \cdot 10^{12}$ m^{-3} maximal difference from the initial radius is 0,85 cm, and the bunch oscillation period is 34 ns.
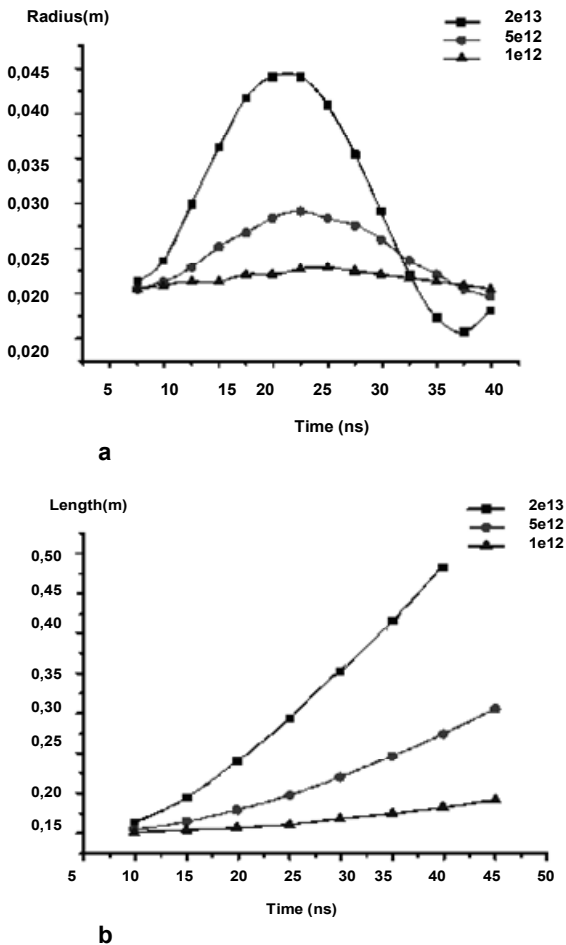

a

b

**Fig. 1: a - beam radius dependence on time;
b - time dependence of the beam length. Density n (m^{-3})
is indicated on the figure, $v_0 = 3 \cdot 10^7$ m/s, $B_0 = 1 \cdot 10^{-3}$ T**

For comparison, estimated values are 0,51 cm and 35,7 ns, respectively. The oscillation period coincides with the period of cyclotron rotation with sufficient accuracy. Calculated amplitudes are related to the first swing, eventually they decrease (see Fig. 2) because of the longitudinal spread of the beam (Fig. 1 b). The rate of the spread increases with the beam density n. From Fig. 3 one can see that difference between simulation results and formula (6) is minimal for small values of the bunch density and increases for large values.
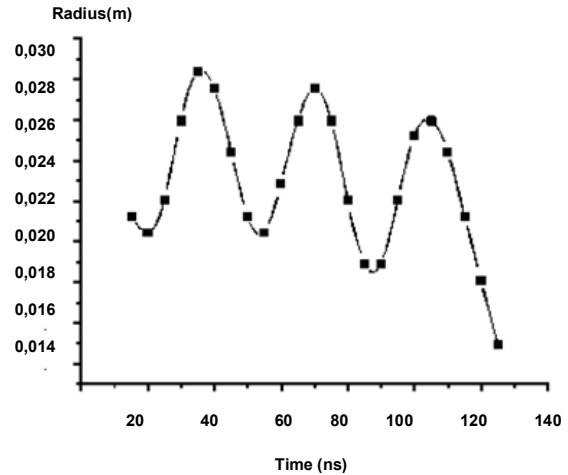

Fig. 2. Time dependence of the beam radius:
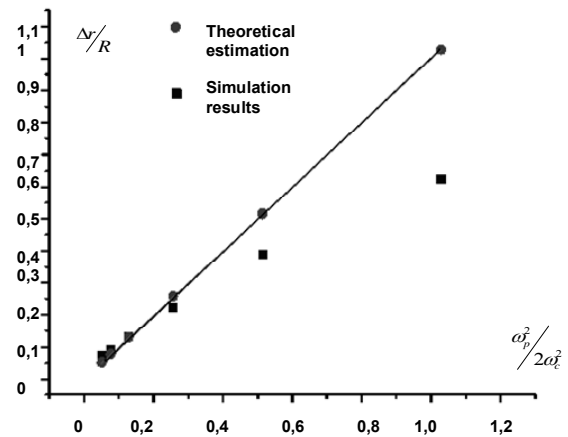$n = 5 \cdot 10^2 m^{-3}$, $v_0 = 1 \cdot 10^7$ m/s, $B = 1 \cdot 10^{-3} T$

**Fig. 3. Simulation and theoretical dependencies
of $\Delta r/R$ on $\omega_p^2/2\omega_c^2$.(beam density is varied)**

Simulation results for different values of external magnetic field Another series of simulation was carried out for bunches with equal concentration of electrons – $5 \cdot 10^{12}$ m^{-3} and different values of longitudinal magnetic field (Fig. 4).

From the graph one can see that increase of the field reduces the amplitude fluctuation and increases the frequency of radius fluctuations.

It is considered that swelling of the bunch is stopped if the expression $\Delta r/R \ll 1$ is correct. That means that the inequality $\omega_B \ll \omega_{ce}$ must be satisfied where $\omega_B = \sqrt{4\pi n e^2/m}$ is Langmuir frequency for the bunch density.

Obviously, the field $B_0 = 0,25 \cdot 10^{-3}$ T is not suitable to focus the bunch, but for $B_0 = 4 \cdot 10^{-3}$ T the bunch radius fluctuations are small and in a certain approximation the bunch is focused.
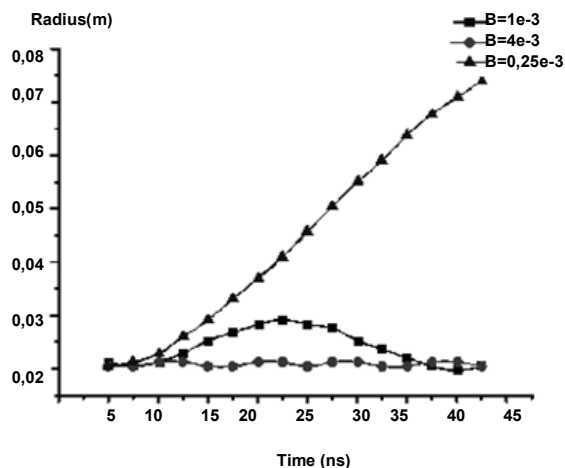
Fig. 4. Time dependence of the bunch radius for different values of external magnetic field (indicated on the figure in T)

$$v_0 = 3 \cdot 10^7\, m/s\,,\ n = 5 \cdot 10^2\, m^{-3}$$

From Fig. 5 one can see that difference between theoretical estimation and simulation results decreases with the growth of magnetic field.
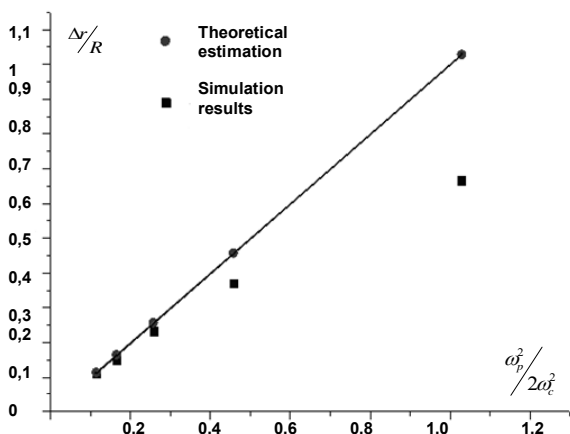

Fig. 5. Simulation and theoretical dependencies of $\Delta r/R$ on $\omega_p^2/2\omega_c^2$.(magnetic field is varied)

Simulation results for relativistic bunch Another series of simulation was intended to study the relativistic bunch, with speed, commensurable with the speed of light,

without an external magnetic field. Law of motion for particles with such velocities differs from Newton's law, pulses increase in account of relativistic factor. This can move to deceleration of the bunch expansion. Simulation was carried out for the system with length of 13,5m, without external field, bunch density was $5 \cdot 10^{12} m^{-3}$, velocity – $2,7 \cdot 10^8$ m/s (v/c=0,9) therefore

$$\gamma \equiv \frac{1}{\sqrt{1-\left(v/c\right)^2}} \approx 2,3$$

Fig.4 shows a half section of the bunch density distribution at the beginning and at the end of the passage through the system. One can see that during 19 ns the bunch radius expanded only on 1,34 sm. For non-relativistic bunch this value would be 1,5 sm. So for v/c=0,9 influence of relativistic effect is not substantial.

At the forefront the bunch radius is increased and its density is decreased relatively to the bunch bulk. Front and back edges of the bunch are slightly blurred.

Fig. 6. Half section of the bunch density distribution at time of 0,6 ns(1) and 19 ns (2). v=2,7·10⁸ m/s (v/c=0,9), L=13,5m, n=5·10¹²m⁻³

Conclusion The results obtained from simulation, correlate satisfactory with theoretical estimations: variation of the bunch is proportional to it's density, the pulse frequency is equal to the cyclotron frequency for the given magnetic field with the sufficient accuracy. Eventually oscilation of the bunch radius decreases because of the longitudinal spread. For low values of magnetic field bunch can not be focused in given system. Increase of the forefront radius of the relativistic bunch can be caused by the following effect: motion of the beam particles forms the azimuthal magnetic field, which focuses the beam. The spreading of the bunch forefront can be caused by the lower magnetic field in this area.

Reference
1. Electronic beam technology. / Gaysing U., Panzer S. // Energy, 1980 (in German). 2. Electron Physics. / Levitsky S.M. // Kyiv, 2005 (in Ukrainian).3. Vacuum and solid-state electronics UHF./ Levitsky S.M., Koshevaya S.V. // Kyiv, High school, 1986 (in Russian). 4. 2.5D relativistic electromagnetic PIC code for simulation of beam interaction with plasma in axial-symmetric geometry. / Tolochkevych Yu.M., Litoshenko T.Eu., Anisimov I.O. // Problems of Atomic Science and Technology. Series: Plasma Electronics and New Acceleration Methods. – 2010. – №4. – P. 47–50.

М. Щербінін, студ., І. Анісімов, д-р фіз.-мат. наук, кафедра фізичної електроніки, радіофізичний факультет, Київський національний університет імені Тараса Шевченка

ДИНАМІКА ЕЛЕКТРОННОГО ЗГУСТКУ В ЗОВНІШНЬОМУ МАГНІТНОМУ ПОЛІ. КОМП'ЮТЕРНЕ МОДЕЛЮВАННЯ

Досліджено вплив поздовжнього магнітного поля на розбухання електронного згустку у вакуумі. Аналітична оцінка просторової залежності радіуса згустку порівнюється з результатами моделювання методом макрочастинок у комірках. При великих магнітних полях та малих густинах згустків результати аналітичного розрахунку та моделювання добре узгоджуються між собою. Досліджено також динаміку релятивістських згустків.
Ключові слова: розбухання електронного згустку, поздовжнє магнітне поле, моделювання методом макрочастинок у комірках.

М. Щербинин, студ., І. Анисимов, д-р физ.-мат. наук, кафедра физической электроники, Радиофизический факультет, Киевский национальный университет имени Тараса Шевченко

ДИНАМИКА ЭЛЕКТРОННОГО СГУСТКА ВО ВНЕШНЕМ МАГНИТНОМ ПОЛЕ. КОМПЬЮТЕРНОЕ МОДЕЛИРОВАНИЕ.

Было исследовано влияние продольного магнитного поля на разбухание электронного сгустка в вакууме. Аналитическая оценка пространственной зависимости радиуса сгустка сравнивается с результатами моделирования методом макрочастиц в ячейках. При больших магнитных полях и малых плотностях сгустков результаты аналитического расчёта и моделирования хорошо соотносятся между собой. Была исследована также динамика релятивистских сгустков.
Ключевые слова: розбухание электронного сгустка, продольное магнитное поле, моделирование методом макрочастиц в ячейках.

В І С Н И К

КИЇВСЬКОГО НАЦІОНАЛЬНОГО УНІВЕРСИТЕТУ ІМЕНІ ТАРАСА ШЕВЧЕНКА

РАДІОФІЗИКА ТА ЕЛЕКТРОНІКА

Випуск (2)20

Друкується за авторською редакцією

Оригінал-макет виготовлено Видавничо-поліграфічним центром "Київський університет"